공학박사학위논문

준비정상상태 해석을 통한 항공기 결빙의 비정상 특성에 관한 수치적 연구

Numerical Investigation of unsteady characteristics in inflight icing via quasi-unsteady approach

2023 년 2 월

서울대학교 대학원

항공우주공학과

민 승 인

준비정상상태 해석을 통한 항공기 결빙의 비정상 특성에 관한 수치적 연구

Numerical Investigation of unsteady characteristics in inflight icing via quasi-unsteady approach

지도교수 이 관 중

이 논문을 공학박사 학위논문으로 제출함

2022 년 11 월

서울대학교 대학원

항공우주공학과

민 승 인

민승인의 공학박사 학위논문을 인준함

2022 년 12 월

위 원 장 : 김 규 홍

부위원장 : 이 관 중

위 원 : 김 태 성

위 원 : 손 찬 규

위 원 : 명 노 신

Abstract

Numerical Investigation of unsteady characteristics in inflight icing via quasi-unsteady approach

Seungin Min
Department of Aerospace Engineering
The Graduate School
Seoul National University

Accurate prediction of ice shape for inflight icing is crucial in preventing operational incidents during flight. As inflight icing is a phenomenon that involves a wide range of variables, the issue in developing simulation tools was numerical efficiency in its early stage. The quasi-steady approach was introduced to resolve inflight icing simulations involving parameters with various sizes, which provided a general inflight icing analysis method using a steady solution for each parameter and a multi-shot method. While this method effectively accounted for aerodynamic change due to ice accretion with low computation resources, it neglected the unsteady characteristic that should be addressed for accuracy. Modeling aerodynamic unsteadiness in moving objects like rotorcraft was one issue, and microscopic surface roughness growth in ice accretion was another. Prior studies

have continuously addressed these issues, and if resolved, inflight icing code accuracy and versatility can be increased.

The present study relieved issues related to unsteadiness that may appear during inflight icing via quasi-unsteady assumption. The quasi-unsteady approach simultaneously solves the air, droplet field, and surface water film, thus taking into timely account variation during the icing process. Based on a quasi-unsteady assumption, the inflight icing simulation has been applied to oscillating airfoil cases. The dynamic mesh technique was used for oscillating motion. This study also adopted a novel model to simulate the roughness distribution and its effect on the transition to improve shape prediction. The roughness distribution is analytically determined based on the maximum water bead height and residual water film. As the thermodynamic module was related to the roughness module, a quasi-unsteady manner was adopted to deliver the roughness effect on the boundary layer. The roughness amplification parameter and transition turbulence model simulated the roughness interaction with the boundary layer.

Thus, the quasi-unsteady approach exhibited good agreement for ice shapes compared to the previous numerical research. This study analyzed the unsteady effect owing to body motion on collection efficiency and convective heat transfer using the quasi-unsteady approach. Furthermore, as in the quasi-steady case, this approach demonstrated that the roughness and laminar-turbulent transition model for the oscillating airfoil could improve the prediction of the ice shape. The convective heat transfer coefficient on the iced surface and ice shape was predicted and compared with the fully turbulent model and experiment result. The results obtained from this approach using the improved model exhibited good agreement with

previously reported experimental results indicating the consideration of unsteadiness is essential for prediction accuracy.

Key words: Aviation safety, Inflight icing, Oscillating airfoil, Surface roughness, Quasi-unsteady approach, laminar-turbulent transition, Turbulent model, Convective heat transfer coefficient

Student Number: 2018-34705

Table of Contents

Abstract I

Table of Contents IV

Nomenclature VIII

List of Figures X

Chapter 1 Introduction 1

1.1 Inflight icing and simulation 1

1.2 Issues in inflight icing simulation 4

1.2.1 Unsteady effect owing to body motion 5

1.2.2 Surface roughness growth 8

1.2.3 Laminar-turbulence transition due to surface roughness 11

1.3 Motivation and scope of the dissertation 12

Chapter 2 Backgrounds for inflight icing and simulation 16

2.1 Icing scenario 16

2.1.1 Icing clouds 19

2.1.2 Icing envelope 20

2.1.3 Parameters for inflight icing 23

2.1.4 Classification of ice shapes 26

2.2 Numerical simulation for inflight icing 30

2.2.1 Aerodynamic module 32

2.2.2 Droplet impingement module 34

2.2.3 Thermodynamic module 35

2.2.4 Ice growth module 37

2.3 ICEPAC 38
Chapter 3 Quasi-unsteady ice accretion solver 42
3.1 Alternative approaches 43
3.1.1 Analytical methods 43
3.1.2 Loose coupling methods – averaged airflow with icing analysis 45
3.1.3 Loose coupling methods – Applying RANS solver 47
3.1.4 Quasi-steady approach for moving body 49
3.2 Quasi-unsteady ice accretion solver 53
3.2.1 Concept of quasi-unsteady ice accretion solver 53
3.2.2 Implementation of quasi-unsteady ice accretion solver to ICEPAC .56
3.2.3 Quasi-steady ice accretion solver for an oscillating airfoil 63
Chapter 4 Physics based roughness modeling 65
4.1 Physics in roughness development 67
4.2 Alternative approaches 70
4.2.1 Multizone model 70
4.2.2 Empirical roughness distribution model 71
4.2.3 Physics based roughness distribution model 72
4.3 Local surface roughness modeling 74
4.3.1 Maximum bead height 74
4.3.2 Water film behavior 76
4.3.3 Implementation of roughness model in ICEPAC 78
Chapter 5 Roughness induced transition model 80
5.1 Alternative approaches 81
5.1.1 1st generation icing code with inviscid flow solver 81

5.1.2 2nd generation icing code with RANS equation....82
5.2 Roughness induced transition modeling....84
5.2.1 Roughness amplification parameter, ***Ar***....84
5.2.2 Modifying turbulence model....86
5.2.3 Applying model to in-flight icing code....90
Chapter 6 Verification and validation....92
6.1 Quasi-unsteady approach....92
6.1.1 Oscillating NACA 0015 airfoil with a smooth surface....93
6.1.2 Oscillating S809 airfoil with leading-edge roughness....95
6.1.3 Collection efficiency of the oscillating airfoil....99
6.2 Laminar-turbulent transition....102
6.2.1 Flat plate case....102
6.2.2 Airfoil with roughness of leading edge....105
6.3 Roughness distribution model....107
6.3.1 Roughness height comparison....107
Chapter 7 Application: Icing on fixed airfoil....112
7.1 Roughness distribution and laminar-turbulent transition....112
7.2 Effect on roughness and transition model on ice shape....116
Chapter 8 Application: Icing on oscillating airfoil....129
8.1 Effect of oscillating frequency on icing solvers....131
8.1.1 Convective heat transfer....132
8.1.2 Collection efficiency....136
8.1.3 Water film thickness....138
8.2 Effect of roughness on oscillating airfoil icing....140

8.3 Ice shape comparison.....145
Chapter 9 Conclusion and Future Works.....149
References.....155
국문 초록.....171

Nomenclature

Symbols

A_r	=	roughness amplification parameter
C_D	=	drag coefficient of droplet
LWC	=	liquid water content, g/m^3
MVD	=	median volumetric droplet diameter, μm
Re	=	Reynolds number
$\widetilde{Re}_{\theta_t}$	=	Reynolds number for thickness of local transition onset momentum
T_{sur}	=	surface temperature, ℃
$\overline{U}$	=	velocity vector, m/s
$c_{p,w}$	=	specific heat of water
$\dot{e}$	=	energy flow rate, W/m^{2}s
g	=	gravitational acceleration, 9.81 m/s^2
h_{cv}	=	heat convection coefficient, W/m^2·K
h_f	=	height of water film, m
k	=	turbulent kinetic energy, J/kg
k_{eff}	=	effective thermal conductivity, W/m·℃
$\dot{m}$	=	mass flow rate, kg/m^{2}s
p	=	pressure, Pa
ρ	=	density, g/m^3
μ	=	viscosity, Pa·s
σ_w	=	surface tension, N/m
τ_w	=	aerodynamic shear stress of wall on water film, Pa
θ_c	=	average contact angle, rad
γ	=	intermittency
ω	=	specific turbulence dissipation rate, 1/s

Subscripts

a	=	air properties
d	=	droplet properties
∞	=	freestream
w	=	water properties
f	=	water film properties
imp	=	impinging water properties
ice	=	accumulated ice properties
eva	=	evaporating water properties
$conv$	=	convective heat transfer properties

List of Figures

Fig. 1. Cloud Classification [46] 18

Fig. 2 Continuous Maximum (Stratiform Clouds) Atmospheric Icing Conditions [48] 21

Fig. 3 Intermittent Maximum (Cumuliform Clouds) Atmospheric Icing Conditions [48] 21

Fig. 4 Natural Probabilities for LWC Averages at Altitudes up to 2500 ft above ground level (AGL) [48] 23

Fig. 5 Feature of Rime Ice [49] 27

Fig. 6 Feature of Glaze Ice [49] 28

Fig. 7. Feature of Mixed Ice [49] 29

Fig. 8. Structure of general inflight icing code 31

Fig. 9. Overall procedure of ICEPAC 39

Fig. 10. Analysis of performance degradation due to icing on the rotorblade [60,62] 44

Fig. 11. Procedure for rotorcraft icing performance analysis proposed by Britton [63] 45

Fig. 12. Procedure for ice shape prediction via loose coupling CFD method [67]..... 48

Fig. 13. Comparison of the ice shape for oscilltiating airfoil at different frequency [21] 50

Fig. 14. Characterization of the oscillating motion into discretized angle of attack [22] 52

Fig. 15 Procedure for predicting ice on oscillating airfoil via quasi-unsteady approach [23] 55

Fig. 16. Quasi-unsteady approach for the icing analysis of an oscillating airfoil..... 59

Fig. 17. Hybrid grid for oscillating airfoil simulation..... 62

Fig. 18. Quasi-steady approach for the icing analysis of an oscillating airfoil 64

Fig. 19. Simplified roughness growth process according to bead formation 69

Fig. 20. Schematic view of the spherical bead geometry [85]..... 75

Fig. 21. Implementation of physics based roughness model on ICEPAC 79

Fig. 22. Implementation of the roughness-induced transition model in ICEPAC..... 87

Fig. 23. Comparison between the aerodynamic coefficients of an oscillating airfoil and a smooth surface [94]..... 94

Fig. 24. Comparison between the aerodynamic coefficients of an oscillating airfoil with leading-edge roughness [95,96]..... 96

Fig. 25. Verification of the droplet impingement module for the quasi-steady and quasi-unsteady solver [23]..... 100

Fig. 26. Zero-gradient flat plate case (Rex = 1,300,000) [43]..... 102

Fig. 27. Coefficients of skin friction for zero-gradient flat plate 104

Fig. 28. Integrated intermittency for partially roughened NACA0012 [85] 106

Fig. 29. Comparison of heights of surface roughness [40]..... 108

Fig. 30. Comparison of heat transfer coefficients [40].....114

Fig. 31. Ice shape compared with the NASA IRT cases [98] 120

Fig. 32. Shape analysis for cases of mixed ice..... 125

Fig. 33. hcv for case 1 (V_∞ = 102.8 m/s, T_∞ = -11.11 ℃, LWC = 0.55 g/m^3, MVD = 20 μm) 127

Fig. 34. Convective heat transfer coefficient for different oscillating frequencies and steady state assumption 133

Fig. 35. γ (intermittency) distribution for different oscillating frequencies and steady state assumption..... 134

Fig. 36. Collection efficiency for different oscillating frequencies and steady state assumption..... 137

Fig. 37. Water film thickness for different oscillating frequencies and steady state assumption..... 139

Fig. 38. Ice shapes for different roughness heights 142

Fig. 39. Ratio for the empirical roughness height according to the reduced frequency 143

Fig. 40. Comparison between the ice shapes on oscillating airfoils 147

List of Tables

Table 1. Time and cost requirement for inflight icing tests 2

Table 2. Characteristics of clouds [1] 17

Table 3. Generation of inflight icing code 33

Table 4. Verification and validation case for quasi-unsteady approach 93

Table 5. Summary of roughness-related characteristics 105

Table 6. Validation cases for surface roughness [40] 107

Table 7. Rough-smooth zone transition location and ice/impinging limit 109

Table 8. Transition onset and transitional region length 113

Table 9. Validation cases for shapes of ice [98] 116

Table 10. Parameters for the experiments of Boeing-NASA consortium [21] 129

Table 11. Distance of transition onset from leading edge at upper surface 135

Table 12. Distance of impinging limit from leading edge at upper surface 136

Chapter 1

Introduction

1.1 Inflight icing and simulation

The water vapor moved to a high altitude with the updraft changes into small water droplets due to the adiabatic expansion of the air. These droplets remain supercooled liquid below the freezing point when the atmosphere remains unstable with insufficient nuclei. The supercooled water droplets grow up to 50 μm at tropospheric altitude and form clouds [1]. As the aircraft passes through the clouds containing these droplets, the equilibrium of the impinged supercooled water droplets is disrupted, and ice accretion occurs. Depending on the component of the aircraft exposed to ice, inflight icing has various adverse effects. The accreted ice of the aerodynamic surface changes its shape, causing a decrease in lift and an increase in pressure drag. Surface contamination indicates performance degradation due to an increase in friction drag. Ice on the fuselage also increases friction drag and ice formation on the radome, sensor, and windshield. It lowers operation safety by disrupting visual sight and the air data required to control the system [2, 3].

To minimize the risks to operational safety caused by inflight icing, regulatory authorities such as the Federal Aviation Administration (FAA) in the US and the European Aviation Safety Agency (EASA) require strict certification procedures under icing conditions [4, 5]. The certification procedures request data on aircraft performance evaluated under various natural icing conditions. Thus, encountering a

cloud that satisfies the test conditions is the primary demand for the natural icing test, which requires considerable time and cost. If the experiment cannot be carried out under various conditions, the icing certification process may last for several years, increasing the risk of the process. As an alternative approach, the performance would be measured by attaching the artificial ice shape obtained through the wind tunnel test to the aircraft. Compared to the natural icing test, the wind tunnel test has an advantage in controlling required atmospheric parameters, regardless of the weather. However, in the wind tunnel, experiments are performed on sub-scale or component-level models due to the size limitation of the test section, while there is not enough scaling law to describe the icing on objects with different sizes. At the same time, there is not enough scaling law to describe the icing on objects of different sizes. Also, the icing wind tunnel test cost is low compared to the natural test, but it is still expensive to apply to all required cases.

Table 1. Time and cost requirement for inflight icing tests

Certification methods	Number of data points	Time requirements	Cost
Natural flight test	10 – 50	2 – 3 months	Over 1million
Icing tunnel test	100 – 150	2 – 3 weeks	Approx. $500 thousand
Numerical simulation	Over 1000	1 day	One day salary

The development of computational tools in the 1980s provided another option in the certification process: numerical simulation. With personal computational resources, reliable numerical simulation is highly desirable for quantifying and evaluating the potential influences of various environmental factors in advance. Table 1 compares the number of data points, the required time, and the cost for each certification method. Based on the theoretical studies of Messinger [6] and Langmuir & Blodgett [7] reached significant progress, the 1st generation of inflight icing code with a two-dimensional inviscid aerodynamic solver and lagrangian droplet solver was developed. The corresponding contributors to early numerical ice prediction research were "LEWICE" [8], the Defence Research Agency (DRA), the Office National d'Etudes et de Recherches Aérospatiales (ONERA) [9], and "CANICE" [10]. As these codes used relatively low-fidelity solvers for aerodynamics, they did not extensively present the three-dimensional characteristics of an aircraft. The 2nd generation icing codes, such as FENSAP-ICE [11] and ICEPAC [12], were developed after the 2000s are based on the three-dimensional Reynolds-averaged Navier-Stokes (RANS) equation.

By applying RANS to the inflight icing code, the numerical simulation has expanded from verifying two-dimensional icing experiments in laboratory units to analyzing arbitrary three-dimensional bodies with more complex shapes. Recently, numerical simulation tools were used as complementary means of compliance during the icing certification campaign. The simulation results were used to set up a test matrix or manufacture the artificial ice shape attached to aircraft components for

flight tests without icing conditions [13]. FENSAP-ICE was used to fabricate artificial ice shapes for icing certification testing on external attachments of Fairchild RC26B [14]. Likewise, as part of its anti-icing device design for CRJ700, Bombardier has used predicted icing parameters of CANICE [15]. Several programs were used to create a virtual icing environment in flight simulators [16]. Many advances in CFD modeling techniques have been developed over the last 20 years to make inflight icing codes more reliable, and efforts are being made to apply them to practical applications.

1.2 Issues in inflight icing simulation

Icing analysis is inherently a multidisciplinary problem due to the velocity range of aerodynamics, droplet field, and surface water film involved. Since the water droplet is derived from aerodynamic drag, its velocity region is similar to that of the airfield. Still, a water film has a relatively low velocity because of the influence of wall shear stress and film thickness in the boundary layer. Additionally, as the density of the water droplet is very low, impinging must continue for several minutes to accumulate ice significantly. As ice accretion occurs over several tens of minutes, interacting closely with airflow and droplet flow, it is necessary to consider shape changes due to ice accretion and following perturbation in the airflow and droplet field for accurate ice accretion simulation. However, computing a fully unsteady solver that updates the ice shape at every step according to ice growth during an icing period requires impractical computational resources [8]. The inflight icing code for

fixed-wing cases adopts a quasi-steady approach that performs a steady analysis rather than an unsteady analysis on a fixed shape [8]. This analysis updates the ice shape generated for a few seconds and proceeds with the calculation process again. Although numerical simulation is considered an efficient way to predict the icing phenomenon, considering unsteady characteristics is limited by this method. When considering moving bodies such as oscillating airfoils simultaneously, icing simulation is challenging due to an inability to adjust the discrepancy between unsteady motion and physical time [18]. Furthermore, under the steady-state assumption, it is difficult to account for the change in roughness height with time, which is an essential factor in thermal convection. The following sections highlight the previous research's limitation for inflight icing simulation.

1.2.1 Unsteady effect owing to body motion

Ice accretion on moving objects is a challenging multidisciplinary issue owing to the aerodynamic unsteadiness associated with body motion and ice growth. Because the unsteadiness resulting from body motion affects the icing parameters, such as collection efficiency and convective heat transfer coefficient, the tight coupling of aerodynamic and icing solvers can yield an accurate prediction of the ice shape [17]. However, the duration of ice growth is much longer than the time required to derive a periodic aerodynamic solution using body motion. During an ice period, computing a fully unsteady solver that updates ice shape throughout the step would be impractical because body motion alters the shape of the ice at each stage [17].

Furthermore, discrepancies in the physical timescale of icing on moving objects have been a major issue for icing on rotorcrafts. More specifically, studies that have considered the local flow effect using the quasi-steady approach are limited to accurately predicting the ice shape on a rotor blade [19,20]. The quasi-steady approach mainly used in fixed-wing cases was focused on the flow change due to ice accretion and was unsuitable for considering unsteady local flow.

Simplified motion is required to analyze the effect of the unsteadiness of objects in motion on predicting ice shapes. Because oscillating airfoils have the advantage of controlling dynamic conditions, numerical studies have focused on the icing on a two-dimensional (2D) oscillating airfoil, such as the experiment performed by Reinhart et al. [21]. As similar ice shapes appeared, Narducci assumed that the ice shape was less relevant with oscillating frequency [22]. Thus, the first proposed method extended the quasi-steady approach by substituting the high-frequency motion with very slow motion with two cycles for whole icing times [22]. The author subsequently divided each cycle into four steps with different angles of attack and arrived at a series of static solutions with updated ice shapes at each location [22]. In some cases, the ice shape was reasonably predicted; however, improving the accuracy of predicting the location of the ice horn and ice volume distribution remained challenging [22]. While the quasi-steady approach to updating the geometry at a given angle and time interval is mathematically more efficient than the unsteady approach, which generates the mesh every time step, some issues arise when extending the methodology to various cases. Firstly, the angle of attack for the

initial calculation started at the minimum angle. In addition, the number of data changes between the airflow and icing solver needs to be limited [22], whereas an increase in data change ensures higher accuracy for fixed-wing cases [8].

To relieve the arbitrariness of the quasi-steady approach with a slow-motion assumption and improve the accuracy of shape prediction, Fouladi suggested a quasi-unsteady approach for periodic motion that can preserve unsteady characteristics [23]. In the quasi-unsteady icing code, the conventional multi-shot method is applied to account for the change in ice shape, which is similar to the quasi-steady approach; however, the unsteady dynamic multiphase solver is used for each shot. A periodic airflow and droplet solutions derived from the unsteady solver determine the ice mass of a small time step within a period. The ice thickness is computed for a single period by summing the ice mass up and repeating the process for each shot. Morreli proposed an approach similar to a multiphase solver that used the Lagrangian method for droplets [24]. Both studies presented practical strategies for predicting ice accretion on a 2D oscillating airfoil; however, these studies briefly mentioned the effects of oscillation on icing parameters in terms of collection efficiency.

The unsteady effect on the collection efficiency and resulting ice shapes presented the advantages of the quasi-unsteady approach over the quasi-steady approach; however, experimental and numerical ice shapes indicated the necessity for correlation between unsteady effect and oscillating frequency. For example, the reduced frequency defines the degree of unsteadiness and theoretically decides whether to consider the unsteady effect in the flow simulation. Efficiency in

predicting ice shape would be improved with the parameter that can present the influence of unsteady effect on the icing phenomenon. Thus, as a preliminary study before applying the quasi-unsteady approach to various cases, a parametric analysis of the effect of oscillating frequency on the governing equation of icing code is required. Considering roughness and laminar-turbulence transitions in a quasi-unsteady approach is another issue concerning convective heat transfer. The roughness and turbulence models, designed under the steady-state assumption, would show physical inconsistency for the oscillating cases. The present study extended the numerical model based on the quasi-steady approach and implemented the quasi-unsteady icing solver to evaluate the unsteady effect on icing parameters.

1.2.2 Surface roughness growth

Inflight icing code describes ice accretion using the surface energy balance, which can be used to determine the rate of ice accretion by removing the latent heat released by solidification. While various components of energy, such as droplet kinetic energy and evaporation energy, are involved in the process, convective heat transfer has a dominant influence [8]. Convective heat transfer on an icy surface is highly dependent on surface roughness and its effects on the boundary layer and surrounding flow field. Thus, modeling the convective heat transfer coefficient on an iced surface can help improve the accuracy of numerical solutions for inflight icing.

Experimental observations of Olsen & Walker showed that impinging droplets and residual water film roughness determine the surface roughness of static airfoils [25]. They observed the surface flow of the water film with close-up movies and photos of the airfoil surface at the early stage of ice accretion. A bead or rivulet of roughness is formed in the glaze zone with residing water, while the feather of roughness is developed in the rime zone where only ice accretion occurs [25]. Hansman et al. conducted a series of experiments focusing on the physics of unfrozen water physics during glaze ice accretion. They suggested qualitative results of the ice shape for cylinders with different liquids to imply that the surface roughness is affected by the adhesion force [26]. Shin illustrated the necessity of a close investigation of the underlying physics of frozen surfaces to take into account the roughness that appears in aircraft icing [27].

The currently widely used surface roughness model was from NASA LEWICE, providing a single value according to the ambient condition [8]. Because of the absence of a quantitative correlation between the roughness elements, an empirical correlation based on the experiments concerning the velocity, temperature, and liquid water content (LWC) was adopted, which provided the linear relation for each parameter [28]. Though the correlation yields the equivalent roughness height according to the test conditions, the approach is associated with several problems. While providing the single roughness value, the model would not resolve the unsteady physics relevant to the local surface roughness growth.

To model the roughness growth during inflight icing, Fortin et al. proposed the roughness distribution model based on water bead height [29]. They divided the surface into (1) a film, (2) a rivulet, and (3) bead states depending on the behavior of water on the surface. The model was applied to first-generation aircraft icing code to predict enhancements in convective heat transfer through the Stanton analogy [30]. Ozcer [31] extended the concept to second-generation icing code and considered the effects of roughness on the increase in surface area. Based on past research, this study proposes a local roughness distribution model based on an analytical solution derived from the shallow water icing model (SWIM) [32].

Since roughness height is based on residual water films on the surface, analysis results for the surface water film are needed. With the 1st generation code, convective heat transfer is considered through an independent model so that the ice accretion solver simultaneously considers the roughness growth. Nevertheless, since the roughness effect occurs in the turbulent model in the 2nd generation code, the quasi-steady solver, which solves the airflow, droplet field, and ice accretion modules in order, would not transfer the turbulent effect on airflow and droplet field solver. Previously, only the increase in surface area due to roughness was considered [31]. They modified the thermodynamic calculation by multiplying the increase in surface area by the convective heat transfer coefficient. The application does not consider the roughness effect on boundary layer formation as theoretical knowledge.

1.2.3 Laminar-turbulence transition due to surface roughness

Considering the roughness impact on the icing process is crucial, along with modeling roughness growth. Roughness has two main effects on inflight icing: shifting the transition location upstream and increasing local convective heat transfer. Many icing codes assumed a uniform roughness, enhancing convective heat transfer, but did not consider roughness distribution and according laminar-turbulent transition. Boundary layer transition is crucial in inflight icing since it affects the strength of heat convection by varying the laminar or turbulent regimes of the boundary layer.

Initial approaches employed the Integral Boundary Layer (IBL) method [33] to divide the laminar and turbulent regimes based on the Reynolds number. According to the user manual of LEWICE [8, 34], this can lead to the overprediction of convective heat transfer, which contributes to the failure to predict some glazed shapes of ice. With the development of second-generation inflight icing codes based on the Reynolds-averaged Nävier–Stokes (RANS) equation, the turbulence model was used by assuming roughness on the leading edge drives the fully turbulent flow. However, the RANS-based inflight icing solver, CANICE2D-NS [35] and FENSAP-ICE [11] underestimate the lower horn during glazed ice prediction. As one option to improve the accuracy of 2nd generation inflight icing code, Habashi noted the necessity of physical modeling of the laminar–transition in turbulence to improve the accuracy of inflight icing simulations [36].

Second-generation inflight icing codes, of which FENSAP-ICE [11] is representative, can predict the convective heat transfer coefficient using a fully turbulent model, such as the Spalart–Allmaras model [37] or the k-w SST model [38]. They assumed that the premature transition in turbulence over a short distance near the leading edge would have a negligible impact on ice accretion. In contrast, according to experimental research [39-41], roughness-induced transition affects the shape of ice at a low Reynolds number when most ice accumulates on airplanes. Only some studies have attempted to predict the ice shape by considering roughness-induced transitions using second-generation icing codes. Thus, while some icing codes applied the Spalart-Allmaras turbulent model, the transition onset predicted through educated guess was expressed through coefficients in the trip term. The effect of roughness growth of icing was challenging to consider when determining the transition onset a priori.

1.3 Motivation and scope of the dissertation

The main objective of this work is to extend an existing quasi-steady state code to address the abovementioned unsteady issues in icing simulation. Then the study developed new numerical models for ice simulation codes. Chapter 3 applied the quasi-unsteady approach to ICEPAC, briefly introduced in Chapter 2, to analyze the unsteady effect of body motion and the interaction between the ice accretion process and body motion. Chapter 4 presents a physics-based model for roughness growth, and Chapter 5 discusses roughness triggering transition in the boundary layer and

enhanced heat convection. The study attempted to overcome the limitations of previous icing research.

1) The present study analyzed the effect of unsteadiness on icing parameters, including collection efficiency, convective heat transfer, and water film thickness. The study also modified a roughness model to account for body motion. Then, the study applied a 2D quasi-unsteady approach to published experimental results for icing on oscillating airfoils to demonstrate sufficient accuracy under various conditions [23]. The quasi-unsteady approach proposed by Fouladi was applied by extending the quasi-steady icing code, ICEPAC [12]. Based on the segregated airflow solver, the droplet impingement and ice accretion solvers were integrated to calculate the ice accretion at every time step. The comparative results obtained from a parametric study on 2D oscillating airfoils determined the impact of body motion on the icing phenomenon. Subsequently, the numerical models used in the icing code were discussed and modified to account for body motion. The modified quasi-unsteady icing code was validated by comparing the predicted ice shape with the experiments performed at the NASA-Boeing consortium [21]. The comparative results are discussed both qualitatively and quantitatively.

2) This study attempted to improve physics-based roughness distribution modeling to include the roughness effect on airflow in the quasi-steady state icing solver. For the local roughness prediction, the present research referred to the model first

proposed by Fortin et al. [29], who divided the surface into (1) a film, (2) a rivulet, and (3) bead states depending on the behavior of water on the surface. Airflow, droplet field, and water film equations were solved in time for the present icing code to account for roughness distributions and boundary layer interactions. The modified roughness distribution model was validated by comparing the roughness measurement performed at the Adverse Environment Rotor Test Stand (AERTS) facility obtained by Han and Palacios [40]. Together with the roughness-induced laminar-turbulent transition model, the model was used to predict the convective heat transfer coefficient.

3) Along with modeling the roughness distribution, another critical factor is predicting the enhancement of heat convection and boundary layer transitions due to roughness. This study was inspired by numerical research on the effect of leading-edge roughness on the turbulent transition on the turbine blade of a jet engine. Dassler, Kozulovic, and Fiala [42] introduced a transport equation for the roughness amplification parameter (A_r) to consider its effect on the transition onset, and it was validated by Feindt et al. [43] through an experiment involving a flat plate. Langel et al. [44] extended the model to airfoils by modifying the parameters. In this study, this numerical method is applied to the local surface roughness of iced airfoils to analyze the impact of roughness-induced transitions on the ice shape. The shapes of ice obtained using the fully turbulent model and the proposed model are compared, and the discrepancy between the results is discussed quantitatively and qualitatively.

Preliminary validation results of these improved numerical methodologies are presented in chapter 6 compared with the available 2D cases. In Chapter 7, the available test cases of fixed airfoils were compared for the ice shape, and in Chapter 8, the comparison was performed for oscillating airfoils. The roughness distribution and laminar-turbulent transition model improved ice shape prediction in the static case. The results obtained for oscillating airfoil exhibited good agreement with previously reported experimental results, indicating the validity of the quasi-unsteady approach. Finally, the numerical issues related to the current approach were described, which may facilitate the development of more innovative computation methods with improved predictive capabilities for icing on three-dimensional (3D) moving objects.

Chapter 2

Backgrounds for inflight icing and simulation

2.1 Icing scenario

Aircraft encounters various icing conditions while passing through clouds with a supercooled droplet on an unstable day. Meteorological conditions and cloud shapes influence the characteristics of supercooled droplets, thereby affecting where and how inflight icing occurs. While cruising, supercooled droplets may be spread horizontally at stratocumulus clouds, and the aircraft would lower the operating altitude to relieve the risk due to icing. Precipitating clouds between cold air below and warmer air above expose the aircraft to rain ice, which can build up ice rapidly. Aviation safety is also compromised when ascending and descending through layers of clouds with icing conditions. During take-off, the fuselage temperature is lower than during other flight conditions, so it is easy to accrete ice on the aerodynamic surface, limiting ascending speed and prolonging exposure to icing conditions. Ice accretion during descending also deteriorates the aerodynamic performance and increases fuel consumption to reach the speed required for landing. Also, the injection of small particles would cause the malfunction of significant parts of aircraft, such as an engine. As icing is a significant threat to operational safety, developing technologies to prevent or relieve the phenomenon is imperative.

Table 2. Characteristics of clouds [1]

Cloud Type		Appearance
High	Cirrus (CI)	Thin, detached cloud with fibrous texture and white color, usually without shading.
	Cirrocumulus (CC)	A white cloud in the form of small globular masses or white flakes. Often arranged in rows, without dark bases.
	Cirrostratus (CS)	A thin, transparent white sheet with indefinite borders. Sometimes slightly fibrous.
Middle	Altocumulus (AC)	White to gray clouds composed of fairly large, flattened globules separated by patches of sky. Often arranged in lines or rows.
	Altostratus (AS)	Denser than CS, but a partially-translucent gray sheet. Usually precedes a general rain by a few hours.
Low	Stratocumulus (SC)	Soft gray clouds in the form of large globule patches. May resemble puffs of cotton. When overcast, they produce an irregular pattern of light and dark patches larger than AC.
	Stratus (ST)	Low uniform layer resembling fog but not resting on the ground. Sun and moon are not visible through the, except when the layer is very thin.
Vertical Development	Nimbostratus (NB)	Gray or dark layer with no distinct cloud element. Thick enough to obscure the sun. Produces precipitation, and may be obscured by lower ST clouds.
	Cumulus (CU)	Detached, dense, vertically-developed clouds, often characterized by flat bases. Horizontal base is usually dark.
	Cumulonimbus (CB)	White dense clouds with great vertical development, associated with heavy rainfall, thunder, hail, and tornados.

Regulatory agencies such as the FAA and EASA strictly prohibit flights in the icing cloud unless the icing conditions have been proven in response to these critical impacts of ice accumulation. Clouds are formed due to the adiabatic expansion of the atmosphere, which drops the temperature to the dew point, and condenses the water vapor into clouds and precipitation. The amount of water vapor in the atmosphere and the altitude determine the formation of clouds. Fig. 1 and Table 2 present the classification of the clouds according to the altitude proposed by Luke Howard in Askesian Society, 1802 [45].

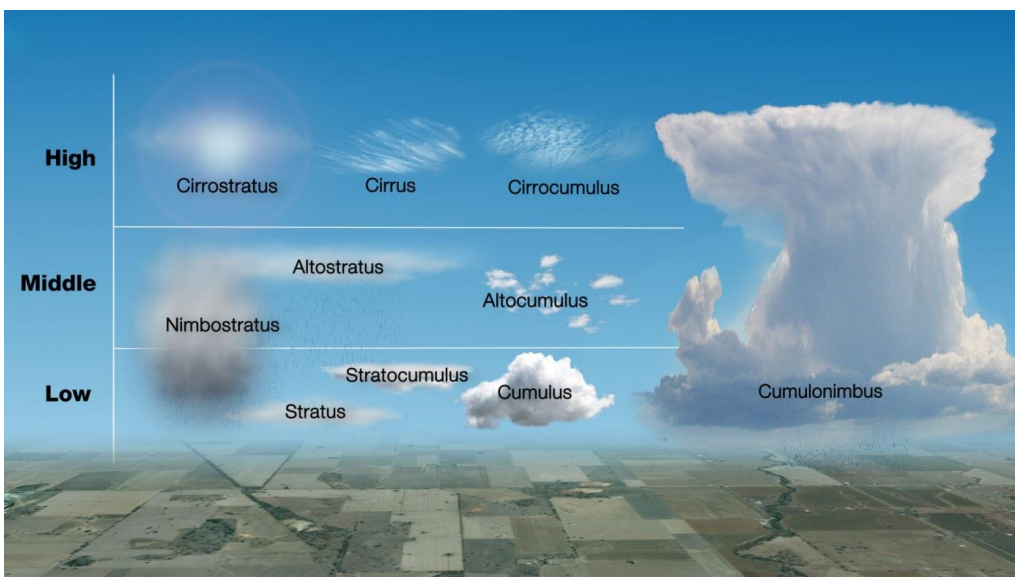

Fig. 1. Cloud Classification [46]

2.1.1 Icing clouds

Depending on the ambient temperature of the cloud, water droplets or ice crystals present in the clouds may cause aircraft icing. Droplets can remain in the liquid state, even if the temperature is below freezing point. These supercooled droplets are the main reason for aircraft icing during the flight. In contrast to supercooled droplets, ice crystals are low in sticking efficiency, so they do not adhere to the aircraft surface, preventing ice accretion. However, even ice crystals can cause icing problems inside engines, where high temperatures drive ice crystals to melt. The clouds mentioned above can be divided into two types based on the ice shape and the icing conditions; stratiform and cumuliform.

a) Stratiform clouds

The stratiform cloud presents horizontally extended layers at low levels. The severity of icing conditions in stratiform clouds is light to moderate. The liquid water content (LWC) ranges from 0.1 to 0.8 g/m^3, and the mean volume diameter (MVD) ranges from 5 to 50 μm [47]. However, due to the vast horizontal extent, aircraft flying through the stratiform clouds are exposed to icing conditions longer. The stratiform cloud typically accumulates rime ice, and the ice characteristics differ according to the altitude at which clouds are formed. Approximately six kilometers above ground level, only ice crystals are present. Ice crystals are almost incapable of sticking to the aircraft surface at this level; thus, icing is not an issue. Icing occurs at mid- and low-level stratiform clouds below 6 km, where ice crystals and supercooled

water droplets are present. At altitudes below 2 km, icing is essential due to the high LWC.

b) Cumuliform clouds

Cumuliform clouds are formed with a strong ascending current and represent the vertical height compared to stratiform clouds. The cumuliform clouds contain large volumes of supercooled water droplets but typically produce little or no precipitation. Generally, the LWC ranges from 0.1g/m^3 to 3.0 g/m^3; for a particular region, it reaches up to 3.9 g/m^3 [47]. Additionally, the vertical current may mix microdroplets, causing them to coalesce into supercooled large droplets (SLD), which are severe hazards to operational safety. Various aspects of icing events can occur as cumuliform clouds exist over a wide range of altitudes.

2.1.2 Icing envelope

In the 1940s and 1950s, the National Advisory Committee for Aeronautics (NACA) conducted experimental and theoretical studies on cloud and icing conditions encountered by aircraft during flight. To indicate the operating conditions in icing conditions, the FAA developed a regulation based on these studies and an icing envelope based on the distribution of temperature, LWC, and MVD according to the flight altitude [4]. It is divided into continuous and intermittent envelopes, with the former applied to stratiform clouds and the latter to cumuliform clouds. Fig. 2 and 3 shows the icing conditions for each envelope.

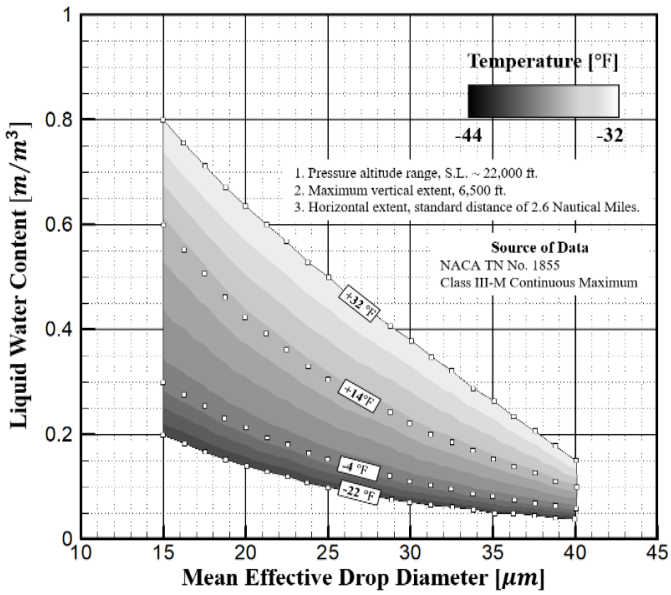

Fig. 2 Continuous Maximum (Stratiform Clouds) Atmospheric Icing Conditions [48]

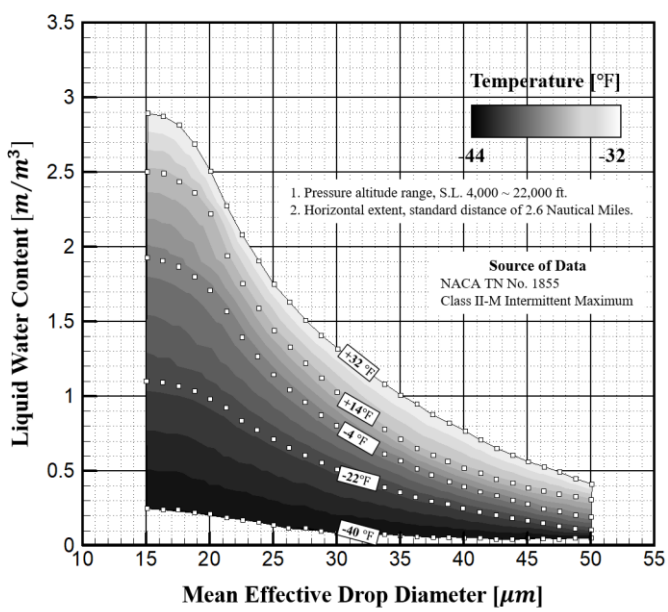

Fig. 3 Intermittent Maximum (Cumuliform Clouds) Atmospheric Icing Conditions [48]

The variables appearing in the icing envelope are related to each other variables. For the constant temperature, the LWC seems to be inversely proportional to MVD; when the MVD is constant, the LWC is proportional to the temperature. In addition, continuous and intermittent envelopes exhibit different icing conditions. With the same temperature and MVD conditions, the LWC of the intermittent envelope is greater than that of the continuous envelope, and the range of the MVD is more extensive in the intermittent envelope than in the continuous envelope. Each of these characteristics corresponds to the above-described aspects of each cloud. The information from the icing envelope would be applied in various aspects, such as the design process of the icing protection system (IPS), by providing the reference design points.

Icing envelopes represent general icing conditions, and the FAA regulation mentions some unique situations that need to be considered [48]. The first is the supercooled large droplet (SLD) condition, characterized by particles much larger than normal MVD. SLDs pose a greater threat to aviation safety than typical droplets. In addition, there is content about freezing drizzle and freezing rain, which can occur just below freezing temperatures. Also, it is essential to note that while the icing envelope summarizes only two types of cloud characteristics, the reality may include a much broader range of conditions. Natural uncertainties such as those shown in Fig. 4 are challenging to contain within the icing envelope.

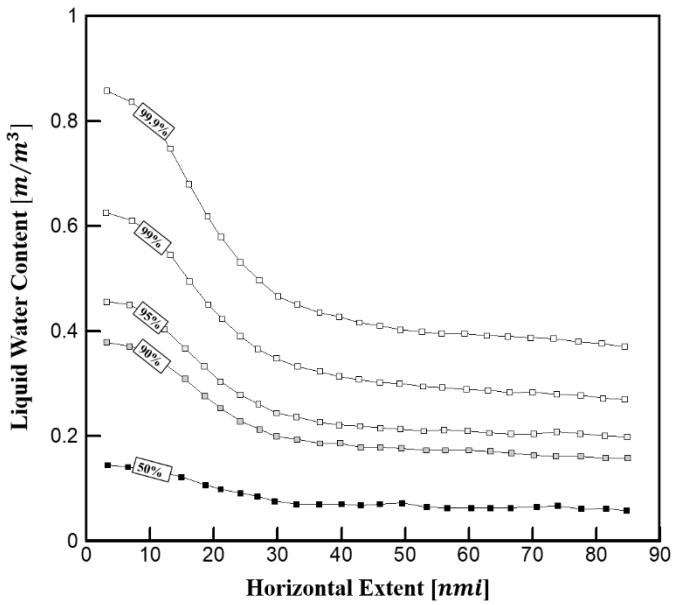

Fig. 4 Natural Probabilities for LWC Averages at Altitudes up to 2500 ft above ground level (AGL) [48]

2.1.3 Parameters for inflight icing

Inflight icing refers to the process of supercooled water droplets impinging the aircraft surface and changing phase. Since solidification is an exothermic reaction, the rate at which ice accumulates is determined by how much heat escapes into the atmosphere. A variety of meteorological parameters must be taken into consideration to understand the ice accretion process. These include mass, kinetics, and energy conservation for water droplets impinged on surfaces and changed into ice. Airspeed, LWC, and MVD are related to the properties of the droplet, while airspeed and ambient temperature are related to the energy balance between the atmosphere and

the surface. Consequently, understanding the meaning of each parameter is crucial in inflight icing simulation.

a) Liquid water contents (LWC)

The liquid water content (LWC) defines the mass of the water in the unit volume of dry air. As the portion of water mass is small, the unit of measurement for LWC is grams per cubic meter (g/m3) [8]. This parameter is essential in figuring out the potential risk for inflight icing. A high LWC would increase water mass impinging on the aircraft surface, resulting in serious ice accretion depending on temperature and airspeed. Also, LWC plays a vital role in determining the types of clouds mentioned above.

b) Median volume diameter (MVD)

The median volume diameter (MVD) represents the size of individual drops of supercooled water, unlike the LWC representation of the quantitative aspect of water in volume. The MVD represents the median values in the droplets distributed in the cloud, representing a normal distribution. The MVD indicates the droplet's size and directly relates to its inertia, indicating the amount of influence a fluctuating flow field has. In most cases, the MVD will determine the range of droplet impingement. A droplet with a small MVD is easily affected by the flow and thus slips away from the surface. However, when the MVD is large, it shows a wider impinging limit. Droplets with excessively high MVD are referred to as supercooled large droplets

(SLD). In this case, high inertia causes surface-droplet interaction such as splashes, rebound, and spreading on the surface.

c) Airspeed

Airspeed affects the inflight icing in two aspects; affecting droplet properties and thermal boundary layer characteristics. In terms of droplet properties, high airspeed would increase the impinging limit by affecting the inertia of supercooled droplets. Also, higher airspeed means an object moves through more space in a shorter period, resulting in more water mass encountering the object. Consequently, airspeed is correlated with impingement rate and quantity. In other aspects, the airspeed affects the boundary layer thickness. As the thickness of the boundary layer determines the thermal boundary characteristics, the convective heat transfer, which is also determined by the temperature gradient, is directly affected by airspeed. Increasing airspeed, convective heat is transferred more quickly, changing the ice thickness distribution. In contrast, aerodynamic heating prevents ice accretion at high airspeeds, such as transonic or supersonic speeds.

d) Temperature

The temperature is an essential factor in determining inflight icing. No freezing occurs even with a high LWC or airspeed if the temperature is above the freezing point. The low temperature of the atmosphere releases the latent heat of ice accretion from the thermal boundary layer. As the temperature lowers, the greater the

temperature difference with the surface, the greater the amount of latent heat released, which causes more ice to accrete. Although low temperatures would increase the threat of inflight icing, a temperature just below freezing temperature can cause other issues. When temperatures are close to the freezing point, a meteorological phenomenon such as freezing drizzle occurs. Droplets formed by freezing drizzle or rain are much larger than those created by supercooled water droplets, and they pose a severe threat to the aerodynamic performance by forming ice crystals or ice layers. At a temperature closer to the freezing point, it is more difficult to predict the ice shape and its effects on performance.

2.1.4 Classification of ice shapes

Inflight icing has various characteristics depending on the values of the variables mentioned above. In general, it can be categorized into three types: Rime, Glaze, and Mixed Ice [1].

a) Rime ice

When water droplets impinge on the surface, some freeze immediately, while the rest spread out as a film and freeze later. Rime ice refers to ice formed when the rate of droplet instantly freezes upon impinging is high. Low ambient temperature and LWC increase the number of droplets freezing immediately, thus offering a high possibility of rime ice formation. As a droplet freezes with a sphere shape, it creates a space between droplets due to the packing fraction, and dry air fills the space and

forms an air pocket. Increasing the number of air pockets makes the ice appear opaque or white and lowers ice density, which are essential characteristics of the rime ice. Another feature of rime ice is that the ice grows along the shape of the object. Since the droplet freezes on impact, it tends to freeze thickly where the collection efficiency is high, usually on protruding edges, so the shape of the ice is relatively predictable. Fig. 5 presents the photographic and schematic image of rime ice [49].

Fig. 5 Feature of Rime Ice [49]

b) Glaze ice

Compared to rime ice, glaze ice appears smooth and transparent when ambient temperatures are near freezing. Glaze ice appears when the ambient temperature is near the freezing point. Since glaze ice drops impinge upon the surface, spread out into a water film, and then freeze again, air pockets are rarely observed. In addition,

since it occurs at a relatively high temperature, some non-frozen water flows to the back of the impinging area. Ice horns are another characteristic of glaze ice. In glaze ice, only a portion of the impinging water mass freezes according to released latent heat through convection. The rest flows, so the ice thickness appears similar to the convection heat transfer coefficient. Thus, when the convective heat transfer coefficient is high, the ice accretion rate is also high, resulting in the formation of the ice horn. During the shape change, the water film is redistributed along the ice horn, representing various shapes, such as double ice horns or bead/feather-like roughness observed in typical accretions. It is possible to form scallop-shaped icing on a swept 3D wing. The glaze ice shape poses a severe problem because they are difficult to predict and seriously degrades the aerodynamic performance by creating a massive separation bubble.

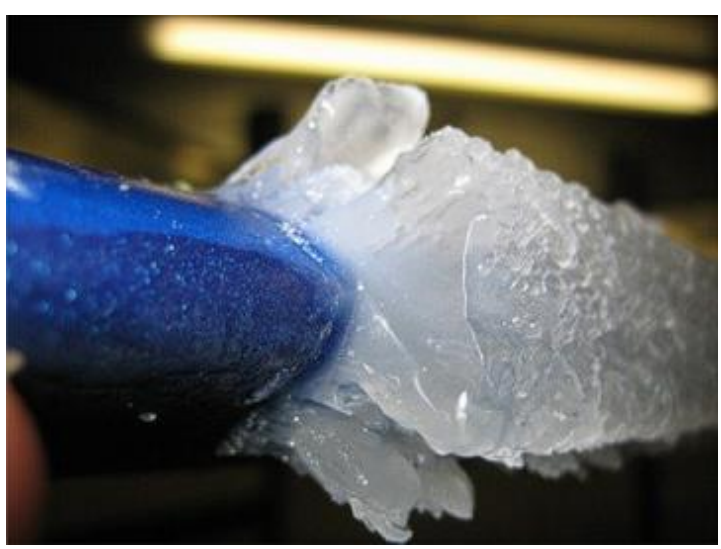

Fig. 6 Feature of Glaze Ice [49]

c) Mixed ice

Mixed ice presents characteristics of both rime and glaze ice shapes. The mixed ice is caused by varying sizes of droplets or droplets mixed with ice or snow particles. While some of the impinged droplets freeze immediately and forms an air pocket, others fill the space between the frozen droplets. A surface's heat convection characteristics determine the dominance of rime and glaze characteristics. Similar to the ice horn in the glaze ice case, ice horns can be generated when heat convection is sufficient to freeze all the water flowing from a point where convection cannot balance out the latent heat.

Fig. 7. Feature of Mixed Ice [49]

2.2 Numerical simulation for inflight icing

The primary focus of inflight icing research has been preventing severe accidents caused by ice accretion on the wing. As icing on the wing directly affects the aerodynamic performance of the aircraft, the early stage of icing research focused on the physics of icing on the airfoil and wing and techniques for icing mitigation through experimental research. In the 1970s, numerical simulation tools were developed to reduce the costs and risks of icing experiments. Since then, experimental and numerical investigations have been conducted complementary to establish more accurate icing simulation tools.

Various numerical models are used to interpret inflight icing phenomena. The governing equation for solving the flow field, the droplet model based on theoretical research of Langmuir & Blodgett [6], and analytical runback model by Messinger [7] for ice accretion are used to calculate ice thickness on the surface. Since each numerical model has a different time step characteristic, quasi-steady ice accretion solver using the multi-shots method has been proposed as a method of linking models to predict the inherently unsteady phenomena of aircraft icing.

The main physical assumption in a quasi-steady ice accretion solver is that the instantaneous airflow around the airfoil accreted ice for a short period is similar to those of a clean airfoil. Consequently, the quasi-steady ice accretion solver employed the multiple-shot method to update the ice shape only at a specified time rather than modifying it every time. Numerical analysis is performed on the final ice shape until the next update. The multi-shot method divides the exposure time under icing

conditions into several time steps, during which the ice shape is determined to sufficiently alter the airflow. NASA LEWICE manual 2.0 states that airflow varies substantially if the maximum thickness is accreted by 10% of the chord length. The computation process called step or shot involves four sequentially linked modules: (1) aerodynamics, (2) droplet trajectory, (3) thermodynamics, and (4) generating the ice shape, as shown in Fig. 8. Each module derives the steady solution of the governing equation for individual fields and transfers the solution to the following module.

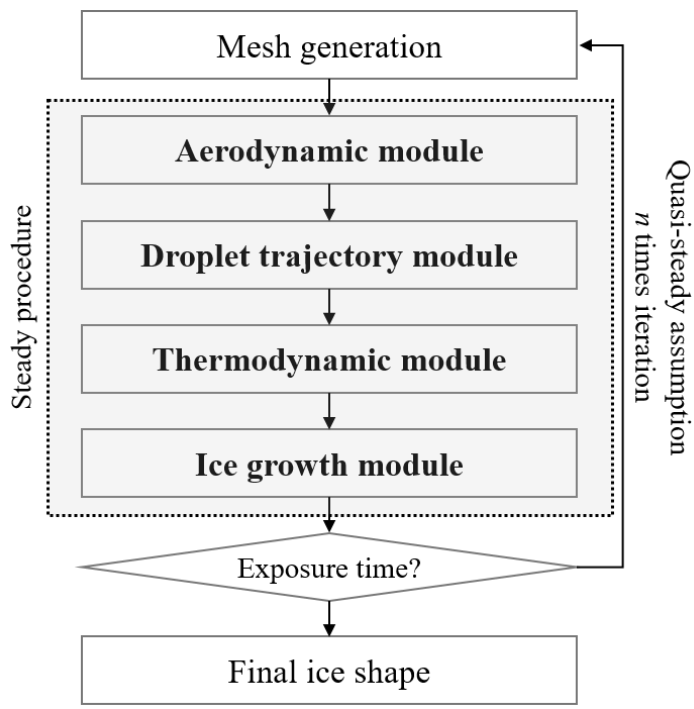

Fig. 8. Structure of general inflight icing code

Throughout this dissertation, quasi-steady or quasi-unsteady refers to a classification of numerical methods for inflight icing, different from a concept originating from aerodynamics. The quasi-steady and quasi-unsteady behavior are used in other fields, such as dynamic aeroelasticity. These terms refer to how perturbations by motion are considered in the classical thin-airfoil theory. The flow simulation is said to be quasi-steady if temporal variations at a spatial location are negligible compared to spatial variations for any quantity. Like the flow simulation approach, the ice accretion solver used the quasi-steady approach to analyze airflow, droplet field, and surface thermodynamics for a fixed ice shape and neglected the change of the ice shape in a time frame for a single shot. Similarly, for the quasi-unsteady ice accretion solver described later, periodic solutions are obtained for fixed ice accretion shapes.

2.2.1 Aerodynamic module

Icing simulation begins with the aerodynamic module. It computes the velocity field that affects the motion of supercooled droplets in the atmosphere. The wall shear stress and convective heat transfer coefficient within the boundary layer region are calculated to affect water film flow over the surface and ice accretion rates. The aerodynamic module applies a potential flow solver or a Reynolds-averaged Navier (RANS) equation solver.

Table 3. Generation of inflight icing code

	1st-generation codes (e.g., LEWICE 2.0 [8])	2nd-generation codes (e.g., FENSAP-ICE [11])
Period	1980 ~ 1990s	1990s ~ Present
Aerodynamic module	Potential flow solver	Navier–Stokes equation
Droplet trajectory module	Lagrangian approach	Eulerian approach
Thermodynamic module	2-D Messinger model	Extended Messinger model Shallow water icing model (SWIM)
Features	✓ Integral boundary layer ✓ Reynolds analogy for heat transfer	✓ Consider the water film movement on the surface

Icing codes are categorized as first-generation and second-generation according to an aerodynamic solver. The first-generation inflight icing codes, represented by NASA's LEWICE 2.0 [8], adopted a potential flow solver [51]. This approach has more advantages in terms of computational efficiency than RANS-based code but has some limitations. In the case of glaze icing conditions, where complex ice shapes and horns appear, the potential flow solver is not suitable for handling the flow with separation. The boundary layer equations or pseudo-viscous field calculations from viscous-inviscid interaction methods result in poor accuracy in numerical analysis when computing near-body characteristics.

The increase in computational power has enabled the practical use of CFD, even in personal computers. The 2md generation in-flight icing codes represented by FENSAP-ICE apply the RANS equations with mature technology [11]. The most prominent feature of these codes is that they can derive a stable solution even for complex shapes. Therefore, 3-D effects limited to the potential flow solver can be considered. These codes derive near-body flow characteristics from the turbulent model and have robust features in the flow-separation region without additional post-processing. Since the RANS-based approach can deal with unsteady challenges, this is commonly used in rotorcraft icing analysis.

2.2.2 Droplet impingement module

The droplet trajectory module was used to compute the density and motion of the supercooled droplets. The objective is to determine the collection efficiency of the surface, which is a non-dimensional parameter for the captured droplet mass. The velocity field data transferred from the aerodynamic module interact with the governing equations for the droplets. Droplet trajectory calculation methods are classified as Lagrangian and Eulerian methods. Both methodologies were used to analyze the rotorcraft icing simulations. This procedure is described in detail in Ref. [52] and [53].

The Lagrangian approach assumes that the droplets are scattered in the far-field region of the frontal area of the body. For computational efficiency, the particles whose trajectories affect the surface are considered. The particle's motion is analyzed

as a point mass particle that is acted upon by aerodynamic results but does not affect the flow. The equation of motion is derived from a force equilibrium equation defined from the lift, drag, and gravity acting on the particle's mass with the angle of attack α.

The Eulerian approach for the droplet trajectory calculations assumes a continuous flow field containing droplets. The droplets are assumed to have a volume of finite density, which could be expressed as liquid water contents (LWC), and the computation area is compatible with a finite volume method (FVM)-based CFD approach. The droplet field is computed through continuity and momentum conservation equations in matrix form based on the converged velocity field obtained from the flow analysis module. As the ratio of the bulk density of the droplets to the air is of the order of 10^{-3} in the inflight icing problem, the effect of the droplets on the flow field is negligible. Therefore, the interaction between the flow analysis solver and the Eulerian droplet trajectory solver is accounted for by the relative drag of the particles in the air.

2.2.3 Thermodynamic module

The role of the thermodynamic module was to compute the ice accretion rate on the surface. The wall shear stress, convective heat transfer coefficient, and collection efficiency computed from the previous modules are linked to generate the mass and energy input of the thermodynamic module. The majority of thermodynamic modules are based on the Messinger model developed in 1953 [7]. The concept of

the Messinger model is derived from the 1st law of thermodynamics and is used to evaluate the energy entering and leaving a control volume, and this balance relies on equating the heat loss from the object to produce the latent heat due to ice growth. The ice accretion rate was computed by coupling with the mass balance or continuity equation. A unique characteristic of the thermodynamic module is that the equations form an open system. Therefore, each thermodynamic module adopts certain assumptions to solve these equations.

LEWICE 2.0 [8] used the freezing fraction, which is the ratio of the ice and incoming mass for the thermodynamic module. The initial freezing fraction was computed by assuming the initial surface temperature as the freezing point. If the freezing fraction is within the range of 0-1, the surface state is assumed to be a mixed condition in which ice and water coexist on the surface. If the initial freezing fraction is >1, then the value was set to 1, and the mass and energy balance equations were recalculated to determine the surface temperature. The surface is covered with only ice. For an initial freezing fraction of <0, the value was set to 0, and the equations were solved by considering if no ice was present on the surface. The module iteratively calculates the freezing fraction and the assumption for the surface matches.

Messinger model has two main variations. The extended Messinger model was modified by applying a standard method of phase change or the Stefan equation [54]. The Stefan equation consists of four equations regarding the energy equation for water and ice layers, corresponding to the mass balance equation and a phase-changing equation at the ice-water interface. The shallow water icing model (SWIM)

applied in FENSAP-ICE is a variation of the Messinger model [32]. Three unknowns along with the two governing equations in the form of a PDE make the system unclosed. The surface conditions that define the surface temperature and ice mass were assumed to be rime, mixed, and only water conditions to keep the system compatible. Subsequently, based on the assumed values, the equations are solved iteratively to determine the matched conditions.

2.2.4 Ice growth module

The ice thickness was computed by multiplying the icing time with the ice accretion rate obtained from the thermodynamic module. Furthermore, the surface grid was shifted forward by the ice thickness. Due to the ice accretion, a newly formed surface was generated by interpolating the ice thickness and normal vector at each surface to the node points. On updating the ice shape, the ice thickness is corrected according to the direction of each point to maintain the volume increment owing to the ice thickness in the normal direction. Subsequently, the calculated ice thickness and normal surface vector were linearly interpolated to adjacent node points, and the newly formed surface was generated using the interpolated node values. Depending on the available computational resources, the grid generation is repeated three or four times to obtain the ice shapes when the surface is exposed to icing conditions.

2.3 ICEPAC

This study aimed to apply new numerical models to the ice contour estimation and performance analysis code (ICEPAC), an ice analysis code developed at Seoul National University based on a quasi-steady approach. ICEPAC is a second-generation inflight icing code that uses the RANS equation for aerodynamic analysis. The solver is built on the open-source CFD code OpenFOAM^{TM} [56], which provides OpenMPI-based parallel computing. As shown in Fig. 9, ICEPAC also consists of four steady-state modules: 1) the aerodynamic, 2) droplet trajectory, 3) thermodynamic, and 4) ice growth modules. Modules of the code are sequentially organized, and governing equations for each module are segregated systems solving continuity, momentum, and energy equations separately. This approach was suitable for the present research, as segregated systems do not require complex modification in governing equations for implementing numerical models. According to the Advisory Circular 20-73A [57], ice accretion in a 45-minute hold condition should be assumed to generate the critical shape of ice for overall performance analysis. To account for the transient shape of ice and aerodynamic characteristics of aircraft icing, numerical simulations using the multi-shot method. The time step for multi-shot method follows the NASA LEWICE manual 2.0, in which the change in the maximum thickness of ice reaches 10 % of the chord length [8]. After the first three modules derive the converged solution for a particular ice shape, the ice growth module determines the accreted ice thickness for a given time to obtain a new ice shape and proceeds to the next shot.

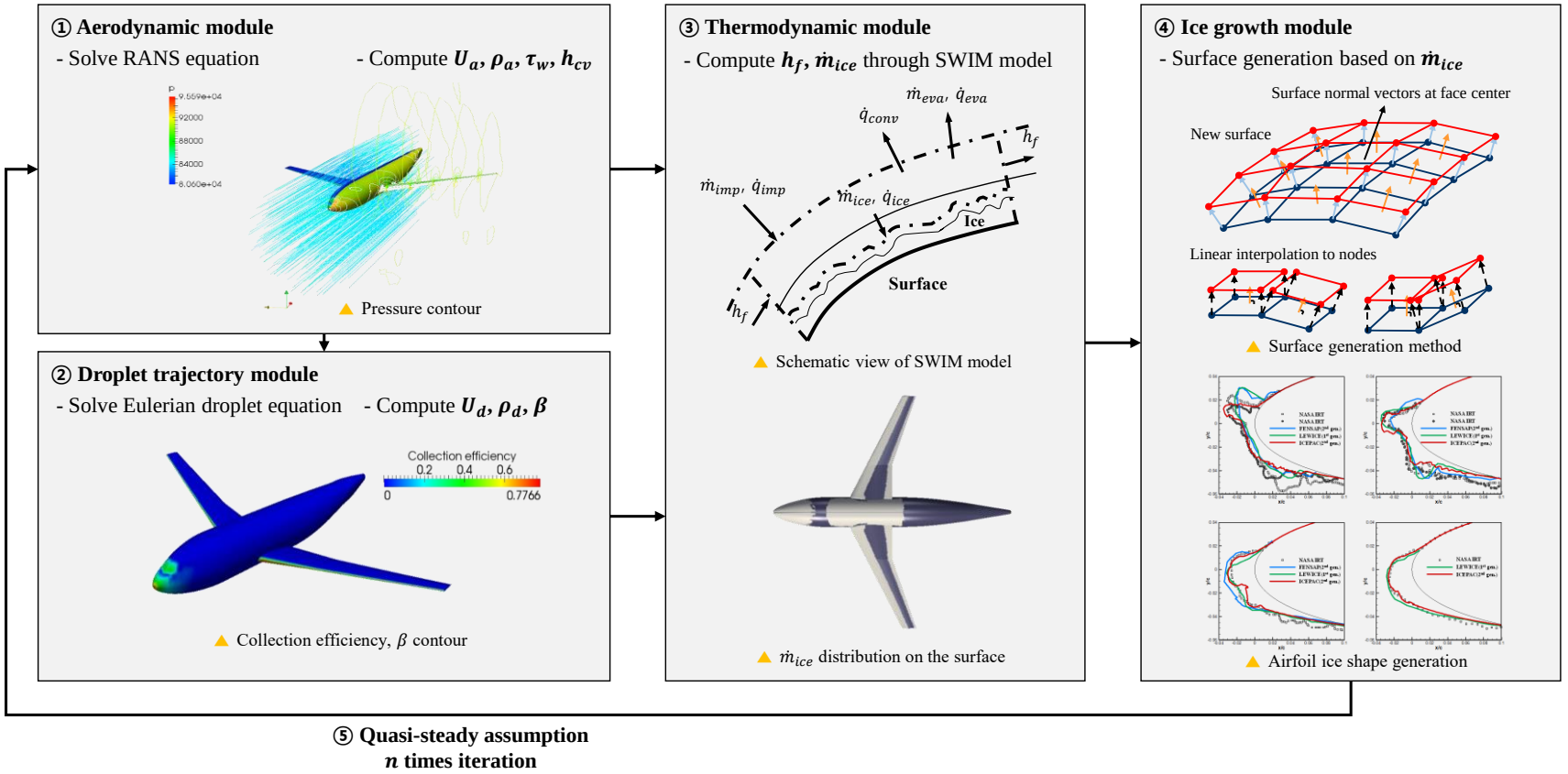

Fig. 9. Overall procedure of ICEPAC

The steady-state Reynolds-averaged Navier Stokes equation was used for the aerodynamic module, which is a steady-state solver for compressible turbulent flow based on the semi-implicit method for pressure-linked equations (SIMPLE) algorithm provided by OpenFOAM™. The physics of the boundary layer described the influence of ice roughness using the $\gamma - Re_\theta$ transition model, including the A_r transport equation [44]. The turbulence model is based on the $k - \omega\, SST$ model, and the boundary condition proposed by Knopp et al. was applied [58]. The droplet impingement module determines the collection efficiency of the surface, which is a nondimensional parameter for the captured droplet mass, with continuity and momentum equations in the form of the Eulerian equation [53]. Equations (1) and (2) represent continuity and momentum equation of the droplet impingement module. The droplet impingement modules were composed of segregated implicit solvers with the CoEuler temporal scheme, a local time-stepping technique provided by OpenFOAM, and first-order upwind schemes for droplet flux for the spatial scheme.

$$\frac{\partial \rho_d}{\partial t} + \nabla \cdot (\rho_d u_d) = 0 \tag{1}$$

$$\frac{\partial \rho_d u_d}{\partial t} + \nabla \cdot (\rho_d u_d u_d) = \frac{3}{4}\frac{\rho_d \mu_a C_D Re_d}{\rho_w MVD^2}(u_a - u_d) + \rho_d g\left(1 - \frac{\rho_a}{\rho_w}\right) \tag{2}$$

The thermodynamic module computes the ice accretion rate on the surface based on the shallow water icing model (SWIM) equation, which consists of a mass and energy balance equation [32]. Equations (3) and (4) represent the SWIM. It consists of segregated explicit equations applying a first-order upwind scheme about water film flux for a spatial scheme and a forward difference time step. We included a description of the schemes of each module before the equations.

$$\rho_w \left[\frac{\partial h_f}{\partial t} + \nabla \cdot \left(h_f u_f \right) \right] = \dot{m}_{imp} - \dot{m}_{ice} - \dot{m}_{eva} \tag{3}$$

$$\begin{aligned} \rho_w \left[\frac{\partial h_f c_{p,w} T_s}{\partial t} + \nabla \cdot \left(h_f c_{p,w} T_s u_f \right) \right] &= U_\infty LWC\ \beta \left[c_{p,w} \left(T_{d,\infty} - T_c \right) + \frac{{u_d}^2}{2} \right] \\ &+ \dot{m}_{ice} \left(L_{fus} T_c - c_{p,ice} T_s \right) - 0.5 (L_{eva} - L_{sub}) \dot{m}_{eva} - \dot{e}_{conv} \end{aligned} \tag{4}$$

The ice growth module computes the ice thickness by multiplying the icing time by the ice accretion rate obtained from the thermodynamic module. Icing time for a single shot is defined as when the maximum ice thickness does not exceed 10% of the chord length, to account for the transient shape of ice and aerodynamic characteristics [8]. On updating the ice shape, the ice thickness is corrected according to the direction of each point to maintain the volume increment owing to the ice thickness in the normal direction. After updating the ice shape, the direction of the inlet velocity is changed to consider the angle of attack variation. A detailed description of ICEPAC is presented in [12].

Chapter 3

Quasi-unsteady ice accretion solver

Due to the aerodynamic unsteadiness associated with motion and ice growth, ice accretion on moving objects is a challenging multidisciplinary issue. As the unsteadiness of body motion affects icing parameters like heat transfer coefficient and collection efficiency, an accurate prediction of the ice shape can be obtained by coupling aerodynamic and icing solvers. While icing continues for several tens of minutes, it is numerically inefficient to perform an aerodynamic analysis using the Navier-Stokes equation, which is typically completed in seconds. A further issue is that each time an icing solution with body motion is obtained, the mesh requires regeneration to update the shape change due to ice growth [17]. These issues result from the discrepancies in physical timescale between the change in aerodynamic properties brought about by moving objects and the ice-shape deformation. When simulating icing on a fixed object, the flow change due to motion is not considered; only the variation in ice shape is considered. Approximately 10% of the characteristic length of the ice is required to affect the flow substantially. Hence, the quasi-steady approach divides the entire time into small time segments for ice to grow sufficiently, and each segment obtains the ice shape through a steady solution. The mesh is updated before solving the next segment, and the process is repeated until the final shape is obtained. The quasi-steady approach would be unsuitable for considering

aerodynamic unsteadiness due to body motion, which has much shorter physical time scales than ice shape.

3.1 Alternative approaches

As the certification process for rotorcraft icing took considerable time, it became imperative to conduct an icing analysis of the moving body. Back then, in the mid-1980s, the US Navy/Sikorsky CH-53E had a limit of 29.7 natural and icing test hours per season, while the other six programs had a limit of approximately 16 hours per season [59]. Rotorcraft icing is a challenging multidisciplinary problem because the rotor motion and icing are inherently unsteady. Consequently, it is more than a decade behind its counterpart in the fixed-wing world in terms of icing simulation. Rotorcraft icing simulations require methodologies incorporating the unsteadiness of rotor motion and icing phenomena. As a result, several rotor simulation methods have been chosen to describe the flow around the rotor blade and to link with the icing solvers.

3.1.1 Analytical methods

The initial approach to icing analysis on moving objects was the computation of the performance degradation of the rotor blade calculated through empirical correlation. Through theoretical and experimental studies, Korkan, Dadone, and Shaw suggested linear correlations between icing parameters and performance degradation for 2D airfoils [60]. The icing parameters were defined based on the

sectional airspeed and angle of attack, including the total collection efficiency and accumulation parameter [61]. A momentum theory equation was applied to the computed drag coefficient to calculate the required thrust of the rotor [62]. With the given thrust coefficient, this method presented the increase in power required to overcome the drag difference caused by the iced airfoil. The empirical correlation with an analytical approach was also extended to the forward flight. Drag difference computed with varying velocity and angle of attack during the forward flight was azimuthally averaged and then linked with the performance analysis code for the rotor. Despite providing a reasonable estimate of performance degradation, the analytical model does not offer ice shape prediction and requires further development, including studies on different airfoil shapes and three-dimensional effects.

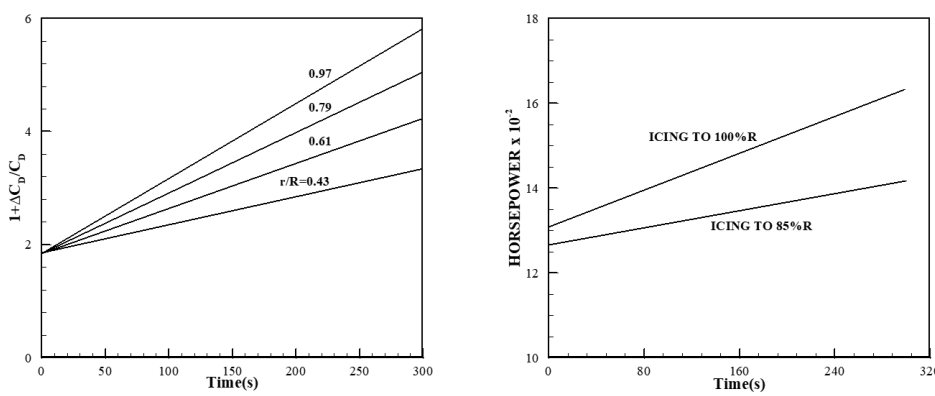

(a) Variation of drag increment with icing time **(b) Power required to maintain C_T of 0.004**

Fig. 10. Analysis of performance degradation due to icing on the rotorblade [60,62]

3.1.2 Loose coupling methods – averaged airflow with icing analysis

Predicting the shape and penalties of ice in advance would provide valuable information for icing on the full-scale rotor system and designing ice protection systems or certification procedures. Combining first-generation icing analysis codes such as LEWICE with Navier-Stokes analysis had become a viable option for calculating the ice accretion on moving objects and their performance. Due to the limitations of computing technology in the 90s, the icing code and Navier-Stokes analysis could not be applied concurrently to moving objects, especially rotor blades. Instead, as shown in Fig. 11, Britton combined a potential flow solver based on the lifting-line theory for rotor blade performance and LEWICE for ice shape and aerodynamic coefficients prediction for the airfoil [63,64].

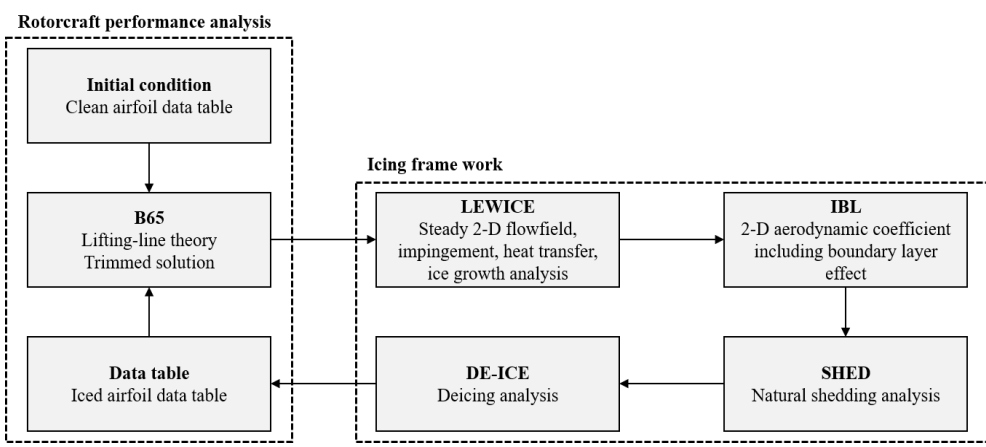

Fig. 11. Procedure for rotorcraft icing performance analysis proposed by Britton [63]

With clean airfoil data as an input, the trimmed solution for local airspeed and angle of attack was calculated using the rotorcraft performance code B65 based on the lifting-line theory. Ref. [62] showed that drag increment measured at different rotor positions with rime ice did not significantly differ from that calculated using the azimuthally averaged value. As a result, the radial trimmed flow input in B65 is azimuthally averaged and connected to LEWICE. Ice accretion is predicted primarily through LEWICE and IBL method, two components of the icing framework. The SHED and DE-ICE modules could address natural shedding and ice protection. The sectional airspeed and angle of attack are used to compute the flowfield around the airfoil, assuming a steady state based on the potential flow program developed by Hess & Smith [51]. Based on the work of Frost, Chang, Shieh, and Kimble [52], two impingement characteristics, total and local collection efficiency, are calculated. The runback model developed by Messinger then simulates the icing process and derives the ice shape [7]. Iced airfoils are resurfaced using the icing mass resulting from the runback Model. The calculation procedure is detailed in Ref. [8]. Using the IBL method [65], new aerodynamic coefficients for ice airfoil are computed for input into the rotorcraft performance code.

In contrast to Korkan's coefficient correlation-based analysis, this approach provided an approach for predicting geometric change and subsequent performance degradation. Although the inviscid incompressible potential flow solver would capture most of the rotor blade physics, it could not accurately simulate the physics around the near wall region, which is essential for the icing analysis. Furthermore,

calculating LEWICE using an azimuthally averaged value ignored local effects, such as varying convective heat transfer along the surface.

3.1.3 Loose coupling methods – Applying RANS solver

As computing capability increased, subsequent work included a Navier-Stokes solver linked with a comprehensive analysis of rotorcrafts. The application of Navier-Stokes solvers made it possible to accurately model the physical characteristics of the inviscid flow solution, improving the accuracy of the icing solver. An essential feature of the loose coupling method is to apply the Navier-Stokes solvers only for the grid system around rotor blades and reside outside the comprehensive code's trimming loop. The Trim loop of the comprehensive code is loosely coupled with the grid system, only transferring aerodynamic data to reduce the computational requirements.

Bain et al. applied the loose-coupling CFD method as an aerodynamic solver for rotor blade icing analysis [66][67]. The aerodynamic solution of rotor flow was computed with GT-Hybrid [68], a hybrid code that links the Navier-Stokes equation and rotor wake model, and DYMORE [69], the computational structural dynamics (CSD) code which derives the trimmed solution. LEWICE3D [70], extended from the LEWICE, was applied for icing analysis. While CFD codes provide an unsteady flow solution, LEWICE3D is a steady-state solver with difficulty accounting for local flow effects varying over time. Therefore, Bain et al. developed a framework to link LEWICE3D to ice accretion/aeromechanics coupling methodology (IACM),

a loose coupling rotorcraft CFD solver. A schematic of this process is shown in Fig. 12.

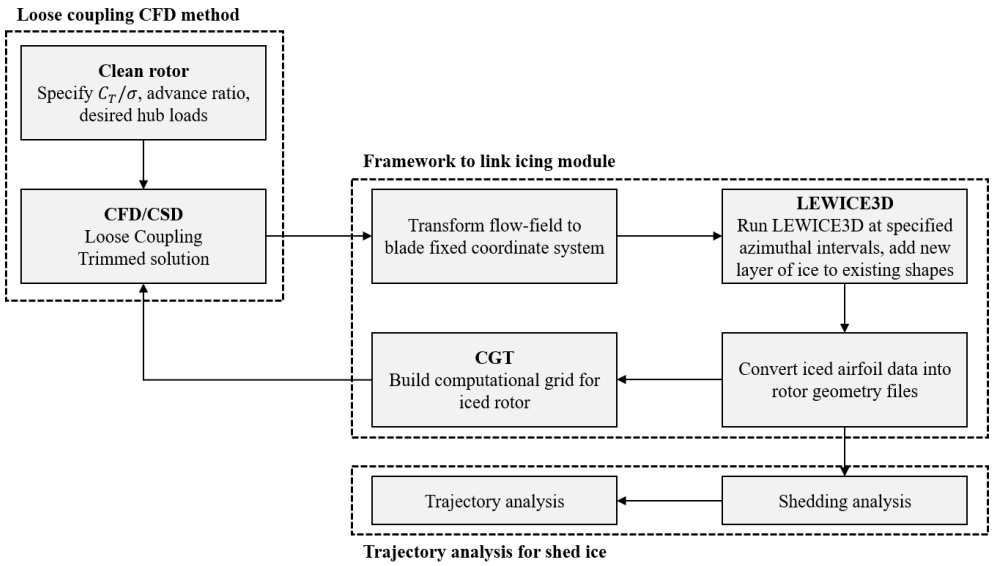

Fig. 12. Procedure for ice shape prediction via loose coupling CFD method [67]

There has been limited use of the quasi-steady approach within the IACM Framework. A user-defined time step is used to consider the slow speed of ice accretion compared to the rotor angular speed. The user-defined time step is determined according to the number of steps dividing the total icing time, and the azimuthal interval follows the time step. In each azimuthal angle, LEWICE3D predicts the ice shape assuming that ice accreted over the defined time. Although this method did not consider the local effect that changes every time, it limitedly includes the varying airspeed and angle of attack in the icing simulation according to the time

step size. A perceptible increase of 14% in torque was observed in the experimental data; while IACM with two steps increased it by 9%, it still provided a more accurate prediction than a single azimuth angle. A further investigation is necessary to account for the effect of body movement on ice accretion.

3.1.4 Quasi-steady approach for moving body

The main concern in simulating icing on the moving body was coupling a steady-state icing code with an unsteady aerodynamic solver. In their study, Bain et al. considered azimuthally changing aerodynamic conditions, but they concluded that further investigation is required for the time step when the ice shapes need to be updated. Thus, a simplified motion object was used rather than a rotating object to study the effects of body motion on ice shape prediction. Due to the advantage of controlling dynamic conditions with oscillating airfoils, experimental and numerical studies have focused on the icing on a two-dimensional oscillating airfoil [21].

Reinhert et al. conducted the icing experiment on oscillating SC2110 airfoil with varying frequency, airspeed, the initial angle of attack, and LWC. According to the study, oscillation frequency has no significant impact on the ice shape. Fig. 13(a) compares the shape of the ice under rime ice conditions with continuous ice spray and discrete ice spray at two different oscillating frequencies. Fig.13(b) presents the difference between ice shapes for a fixed and oscillating angle of attack at high speed.

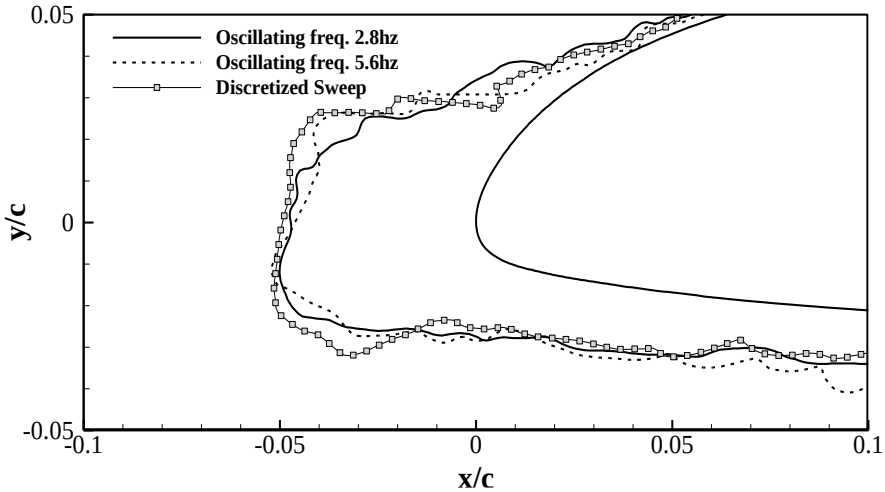

(a) Ice shape comparisons for varying oscillating airfoil and discretized sweep

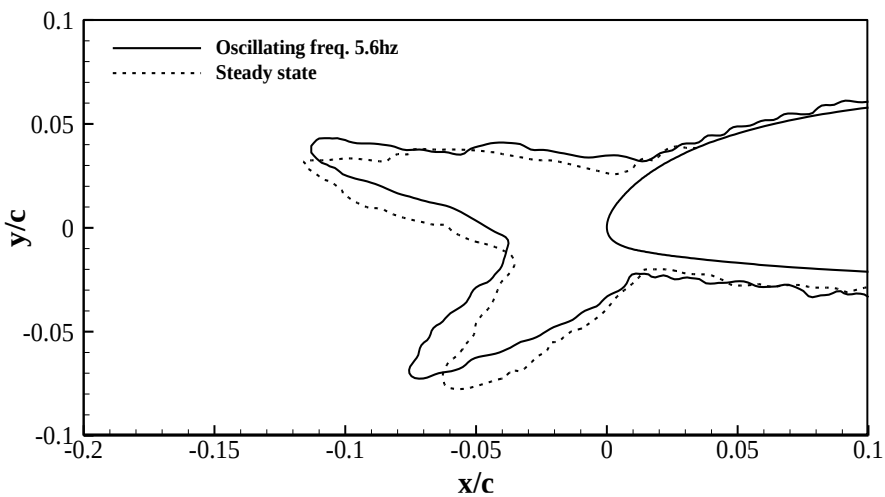

(b) Ice shape comparison for oscillating and steady airfoil at 258 knots

Fig. 13. Comparison of the ice shape for oscilltiating airfoil at different frequency [21]

According to experimental results [21], Narducci assumed that the pitching frequency of the rotor blade would change to slow motion while simulating the pitching motion of the rotor blade in the icing solver [22]. As shown in Fig. 13, this assumption was used to change the pitching motion of the rotor blade to a very slow oscillating motion. The process consists of three steps. Fig. 14(a) illustrates the pitching motion as a simplified sinusoidal function, then Fig. 14(b) shows the high-frequency changing into a slow-frequency. In Fig. 14(c), the slow sinusoidal function is discretized into a quasi-static step function. Thus, a loose coupling technique that receives aerodynamic data from CFD results can be applied. The aerodynamic solver and icing solution are linearly linked at each angle of the step function, and the surface mesh is regenerated for the next angle of attack. Numerical simulations by Narducci provided insights into coupling rotor blade unsteadiness with a quasi-steady icing solver [71,72]. Nevertheless, the quasi-steady approach was unreliable, including the ice volume distribution, especially when glaze-ice conditions were present at the lower horn.

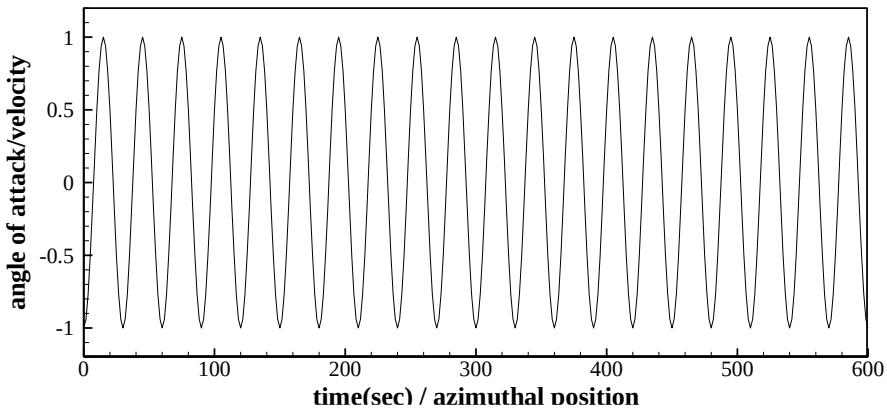

(a) Simplified pitching motion

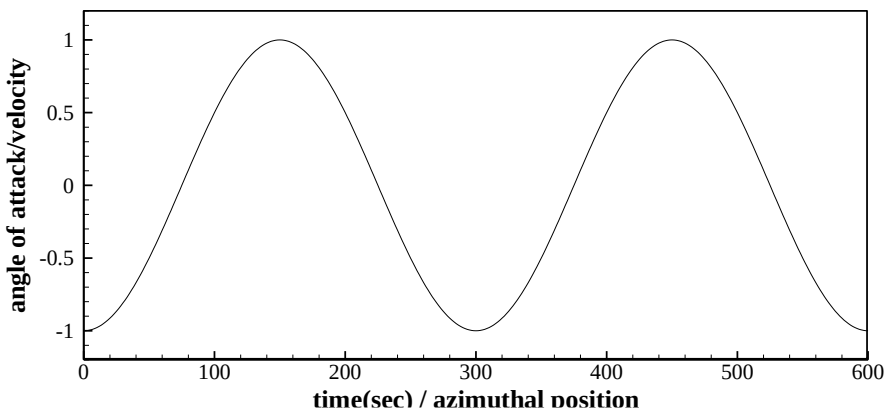

(b) Characterized slow motion

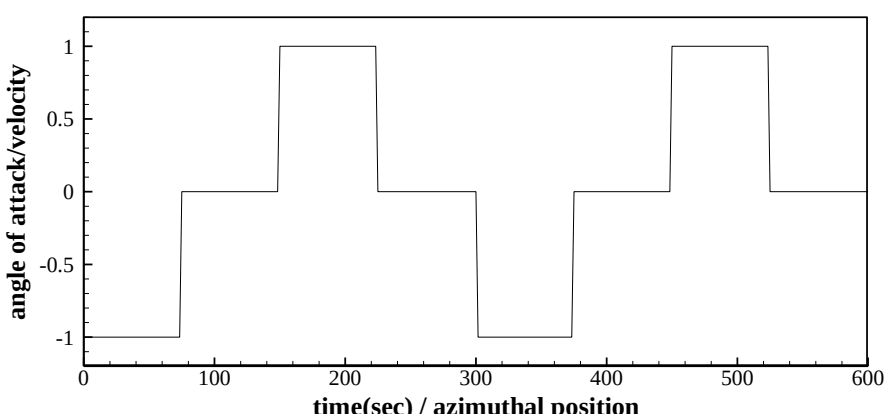

(c) Transformed step function

Fig. 14. Characterization of the oscillating motion into discretized angle of attack [22]

3.2 Quasi-unsteady ice accretion solver

3.2.1 Concept of quasi-unsteady ice accretion solver

Contrary to the quasi-steady ice accretion solver in Chapter 2, which only responds to changes in the ice shape, the quasi-unsteady ice accretion solver is designed to simultaneously handle aerodynamic perturbations caused by ice accretion and aerodynamic and simple harmonic motion. The term quasi-unsteady was used throughout this dissertation because the unsteady analysis was performed on some modules by extending quasi-steady ice accretion solvers to analyze aerodynamic perturbations. As in quasi-steady ice accretion solver, this method neglects the ice shape change for given time in single shot. Hence, the main idea of the quasi-unsteady ice accretion solver is the unsteady calculation within the time step used in the multi-shot method of the quasi-steady ice accretion solver. This additional short-time step considers the unsteadiness that changes faster than the ice accretion effect, namely body motion.

Since the ice accretion occurs very slowly, the aerodynamic perturbation caused by the ice shape in a short period is negligible, assuming that the aerodynamics are equal to those of the original shape. As with the quasi-steady ice accretion solver, the multi-shot method is also used for ice shape change. Due to the faster response time of airflow to body motion than ice accretion, multi-shot methods need assistance handling motion-airflow interactions. The quasi-unsteady ice accretion solver uses unsteady equations to account for airflow response to body motion during the single-shot calculation process. Thus, quasi-unsteady ice accretion solvers use another time

step for unsteady solutions in addition to the time step of the multi-shot quasi-steady icing code. Considering numerical efficiency, a simplified harmonic motion that can derive a periodic solution is appropriate for quasi-unsteady icing codes. In the case of arbitrary motion, the quasi-unsteady icing code can be applied. However, since there is no periodic solution to derive, all unsteady solutions must be calculated during a single time step, requiring an extensive computing resources. Since aircraft components have harmonic motions, various applications with the icing phenomenon would apply quasi-unsteady ice accretion solver by simplifying the harmonic motion into a sinusoidal motion.

The quasi-unsteady approach aims to maintain numerical efficiency while considering unsteadiness due to body motion in each module of the icing solver. Through an unsteady multiphase flow solver that incorporates body motion into the time scale, Fouladi [23] calculated quasi-unsteady ice accretion while maintaining the unsteady characteristics of the flow and droplet field. The unsteady multiphase flow solver iterates until a periodic solution is obtained, and the solution is linked to the ice accretion solver. The ice accretion solver was applied at each small time step (m steps × n cycle/shot), dividing the cycle of motion and icing time. Then, the ice grid was regenerated. Therefore, ice growth affects the flow and water droplet equations in the subsequent calculation. The concept of the quasi-unsteady ice accretion solver is illustrated in Fig. 15.

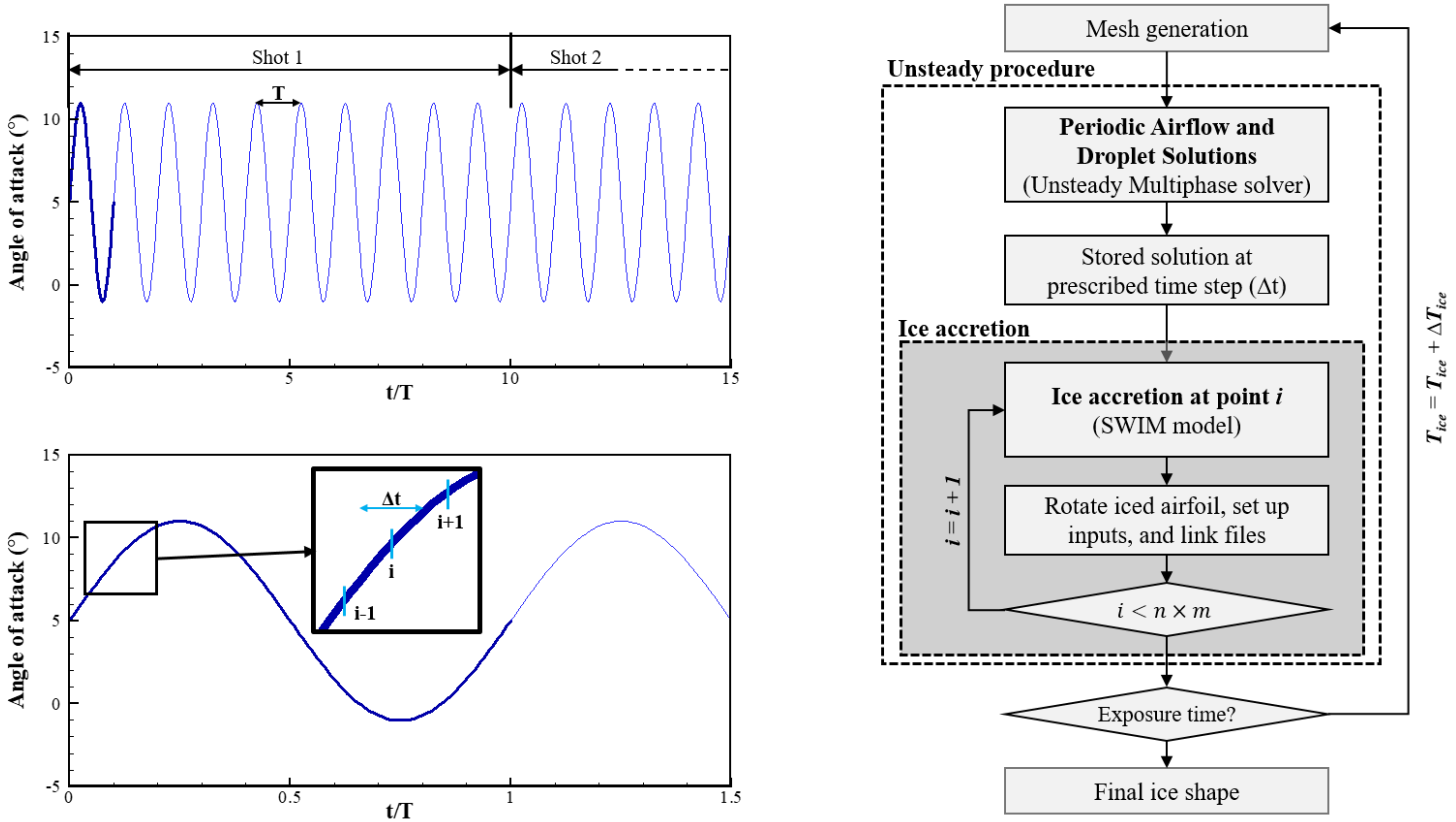

Fig. 15 Procedure for predicting ice on oscillating airfoil via quasi-unsteady approach [23]

3.2.2 Implementation of quasi-unsteady ice accretion solver to ICEPAC

This study applied a quasi-unsteady ice accretion solver to ICEPAC, as shown in Fig. 16. The modified ICEPAC comprises an unsteady loop inside the grey-shaded square and an external ice shape update loop according to the time step. Inside the unsteady loop, the aerodynamic, droplet impingement, and thermodynamic modules were linked within a small time step, which is determined through the airflow solver; therefore, the ice accretion rate was calculated at all positions of the airfoil. The ice thickness for one cycle was derived by adding these ice accretion rates per cycle. Subsequently, by multiplying the number of cycles for one shot, the ice shape was updated by the ice growth module.

The unsteady procedure lasts until a periodic solution for each module is acquired. The number of oscillating processes for periodic solutions for air and droplet fields was heuristically determined. Additionally, the height of the water film and ice accretion rate converged in 1–2 s in the ice accretion solver, depending on the speed of motion and icing condition. The oscillating frequency of the current analysis object is between 2.8 Hz and 5.6 Hz, so a periodic solution can be derived by performing unsteady analysis for 2.16 seconds, where about six cycles occur. Later in the application section, analysis time was organized separately for each case.

During the unsteady cycle, the droplet and thermodynamic equations were sequentially arranged after the unsteady aerodynamic solver loop, as shown on the right side of Fig. 16. Current unsteady cycles are configured differently than in previous research. Fouladi derived a periodic solution using a two-way coupled

multiphase solver and independently solved an unsteady thermodynamic module with the additionally stored periodic solution [23]. The method requires a lot of computing power for 3D problems such as rotorcraft and a separate memory to store periodic solutions for each time step [24]. A one-way coupling method was used in this study since the droplet size and flow rate for general inflight icing conditions had negligible effects on the airflow. Also, a periodic solution was derived for the thermodynamic module by linking with other modules in the same time step to facilitate the computation process after being extended to 3D problems.

An aerodynamic solver was developed based on the compressible transient solver using the PIMPLE algorithm provided by OpenFOAM™. The PIMPLE algorithm is a combination of the pressure implicit with the splitting of the operator and SIMPLE algorithms and provides stability to the inherently unstable solution. The PIMPLE algorithm provides two correctors; the outer corrector indicates the iteration number until time-step convergence based on the absolute tolerance of the solver, and the inner corrector defines the number of times the pressure is corrected. The flux correction column includes the boundary velocity of the grid owing to the mesh deformation caused by the velocity flux.

The droplet impingement module solves the continuity and momentum equations provided in Eq. (7) and (8) after the aerodynamic solution converges through outer correction. In this study, these equations shared the same time step as that of the aerodynamic module. Because the current solver is in the form of a segregated matrix, the solutions converge on ρ_d and u_d separate from the aerodynamic solver. The

surface velocity of the mesh was considered in the divergence term on the left-hand side of Eq. (7) and (8). This process was included in the flux-correction column, such as in the aerodynamic module. In addition, the boundary condition was corrected to include the body motion of the impinging area.

$$\frac{\partial \rho_d}{\partial t} + \nabla \cdot \left(\rho_d \left(u_d - u_{d,s} \right) \right) = 0 \tag{7}$$

$$\begin{aligned} &\frac{\partial \rho_d u_d}{\partial t} + \nabla \cdot \left(\rho_d u_d \left(u_d - u_{d,s} \right) \right) \\ &\quad = \frac{3}{4} \frac{\rho_d \mu_a C_D Re_d}{\rho_w MVD^2} (u_a - u_d) + \rho_d g \left(1 - \frac{\rho_a}{\rho_w} \right) \end{aligned} \tag{8}$$

The thermodynamic module was placed after the droplet-impingement module. Similar to the quasi-steady approach, the thermodynamic module calculates the rate of ice accretion using an unsteady 3D Eulerian thin-water-film model, which describes the conservation of continuity and energy. Additionally, the thermodynamic module employs the same time step as the aerodynamic module. Because the ice accretion occurs on the surface and has no relative motion to airfoil, the equations do not include a term that accounts for body motion. Instead, as the water film speed is linearly proportional to the wall shear stress, and the wall shear stress is calculated from the relative velocity of the flow and moving wall, the model incorporates the body motion effect. Therefore, the SWIM model represented by Eq. (3) and (4) in the quasi-steady approach was applied to the governing equations.

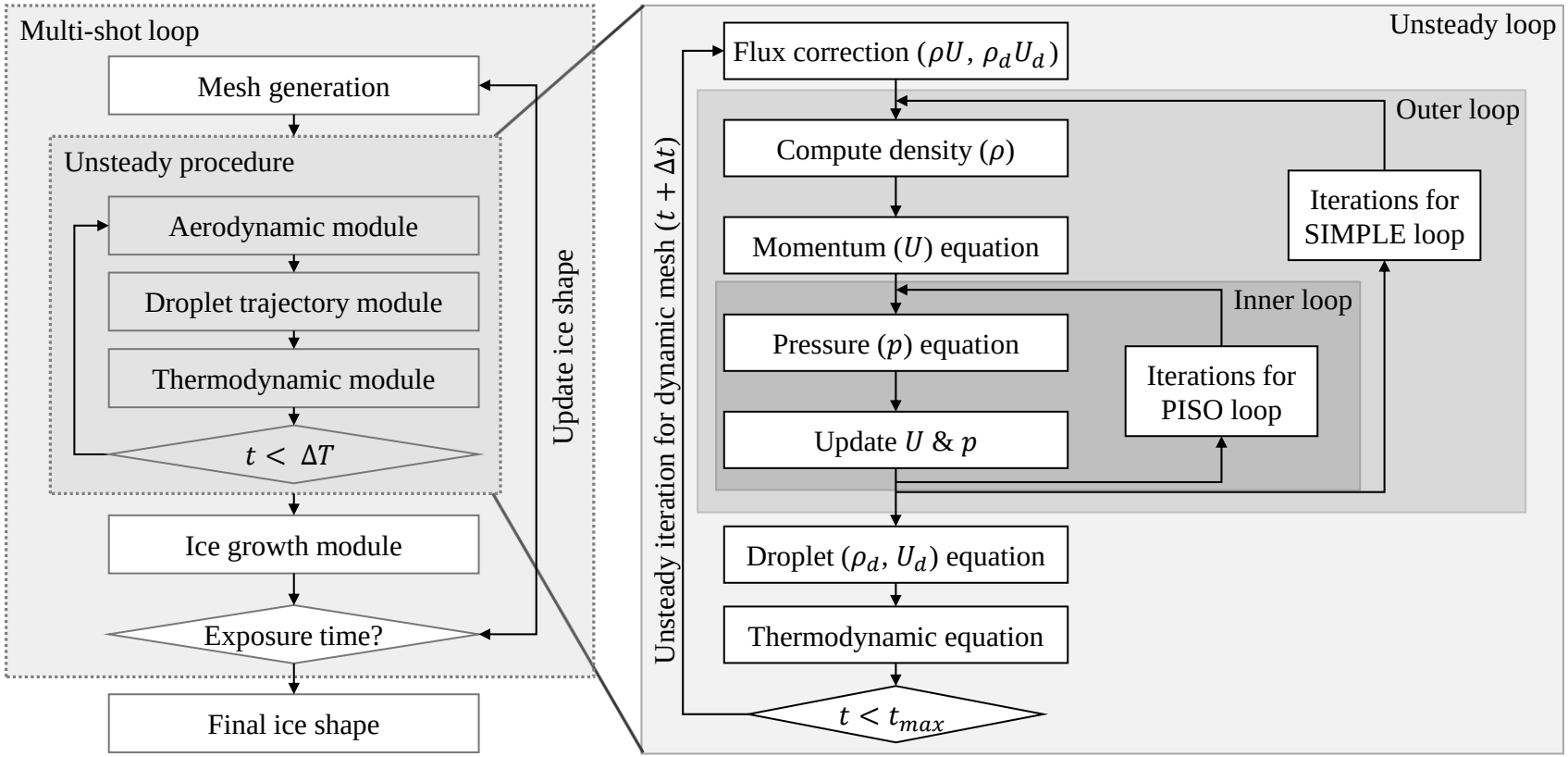

Fig. 16. Quasi-unsteady approach for the icing analysis of an oscillating airfoil

a) Time step for quasi-unsteady ice accretion solver

A crucial part of the quasi-unsteady ice accretion solver is determining the two different time steps. ΔT, the large time step shown in Fig. 16, is used in the multi-shot method. As an application of the multi-shot method, the quasi-unsteady approach updates the geometry for every ΔT when the maximum ice thickness reaches 10% of the chord length. This time step for single-shot was calculated using Eq. (9) of LEWICE 2.0 [8]. According to the icing condition used throughout the study, the time step was 50 seconds for one shot. Generally, ice shape for oscillating airfoil was acquired after 12 shots over 10 minutes.

$$\Delta t \leq \frac{(0.1) * (0.917 \times 10^5 g/m^3)c}{\beta_{max} V_\infty LWC(1 + \alpha/20)} \tag{9}$$

A Δt is another time step in the unsteady procedure, which solves the airflow, droplet trajectory, and thermodynamic module sequentially. Therefore, Δt was determined as the minimum time step among the time steps necessary to solve each module's governing equations. In this study, since the droplet field's velocity region is the same as the airflow region and the water film's velocity region is relatively slow in the thermodynamic module, the time step of the airflow solver was used. Due to the PIMPLE algorithm's numerical stability requirement, a time step satisfying the Courant-Friedrichs-Lewy (CFL) condition was adopted. Generally, the CFL number was set to 5, and iterations continued until each governing equation within each time step satisfied the tolerance. The criteria for time step convergence

is defined as the absolute tolerance of the solver, which is by default 1e-8, and for droplet field 1e-12, where the order of droplet density is 1e-5.

b) Dynamic mesh

In this study, a dynamic mesh approach was applied to capture the oscillating motion of an airfoil. OpenFOAM provides a variety of rigid-body motions with prescribed moving meshes. Because oscillating motion does not account for the large deformation in the mesh, a motion solver without topological changes was used. The dynamic mesh approach in OpenFOAM determines new positions for points with a given amplitude, angle, and frequency. The Euler angle is computed using this information and translated into quaternions. The motion is characterized by the spacing between nodes at different time steps using the calculated motion velocity, as expressed in Eq. (5).

$$x_{\text{new}} = x_{old} + u\Delta t \tag{5}$$

Since the effect of surface roughness on the boundary layer is crucial, for a near-wall grid spacing y+ below 1, the cells in the boundary layer region have a high aspect ratio. Therefore, mesh deformation may lower the stability of the solution owing to the non-orthogonality of the mesh. To maintain the robustness of the solver, the mesh used throughout the present study was divided into three different regions according to distance of the points from wall, as shown Fig. 17. The points inside

d_{inner} has the motion scale of 0 and follows the same motion as that of body. The points outside d_{outer} are fixed, where the motion scale is 0. The points between the two regions are defined using the motion scale by linearly selecting values between 1 and 0 according to the wall distance.

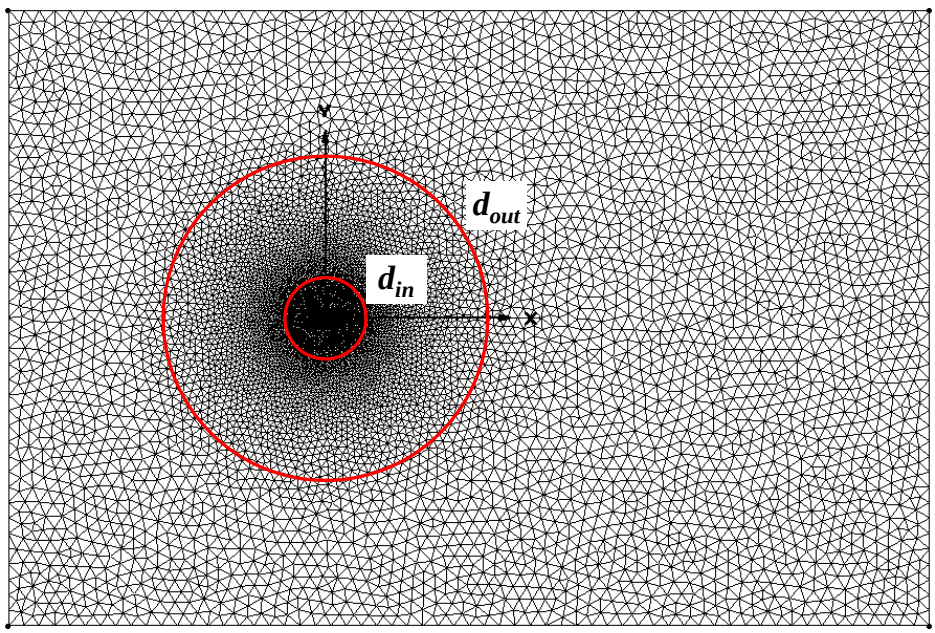

Fig. 17. Hybrid grid for oscillating airfoil simulation

The governing equation of the finite volume solver is modified to Eq. (6) over an arbitrary moving volume V bounded by a closed surface S [73]. The mesh deformation is described using the velocity of the boundary surface, u_s, computed from Eq. (5). The space conservation law was applied to define the relationship between the rate of change of the volume and velocity of the boundary surface [74].

$$\frac{\partial}{\partial \mathrm{t}}\int_V \rho\phi\partial V + \oint_S \rho n\cdot(u-u_s)\phi\partial S - \oint_S \rho\gamma_\phi n\cdot\nabla\phi\partial S = \int_V s_\phi \partial V \qquad (6)$$

3.2.3 Quasi-steady ice accretion solver for an oscillating airfoil

This study aims to examine the impact of unsteadiness on the icing parameter and the ice shape by using the quasi-unsteady ice accretion solver. Hence, the comparative results on 2D oscillating airfoils were obtained by comparing predicted icing parameters and ice shape of quasi-steady and quasi-unsteady ice accretion solvers. A quasi-steady ice accretion solver was initially applied to the oscillating airfoil for comparison with a quasi-unsteady approach proposed by Reinhart & Narducci [22] before the quasi-unsteady ice accretion solver was applied. To account for the pitching motion of the rotor blade in the icing solver, Narducci assumed that variations existed in the pitch and velocity of the rotor blade during slow motion based on experimental results [21]. As shown in Fig. 18, the pitching motion was imposed to low-frequency sinusoidal during icing, which was subsequently simplified to a step function. In Fig. 18(a), the circled number indicates the step for which the quasi-steady solver is applied in Fig. 18(b). The first step of the simplified step is to solve the modules of the quasi-steady solver. The second step is to transfer the data to the next angle of attack and update the shape based on the ice accretion rate calculated in step 1. The ice growth module computes the ice thickness by multiplying the icing time by the ice accretion rate. After updating the ice shape, the direction of the inlet velocity is changed to consider the angle of attack variation.

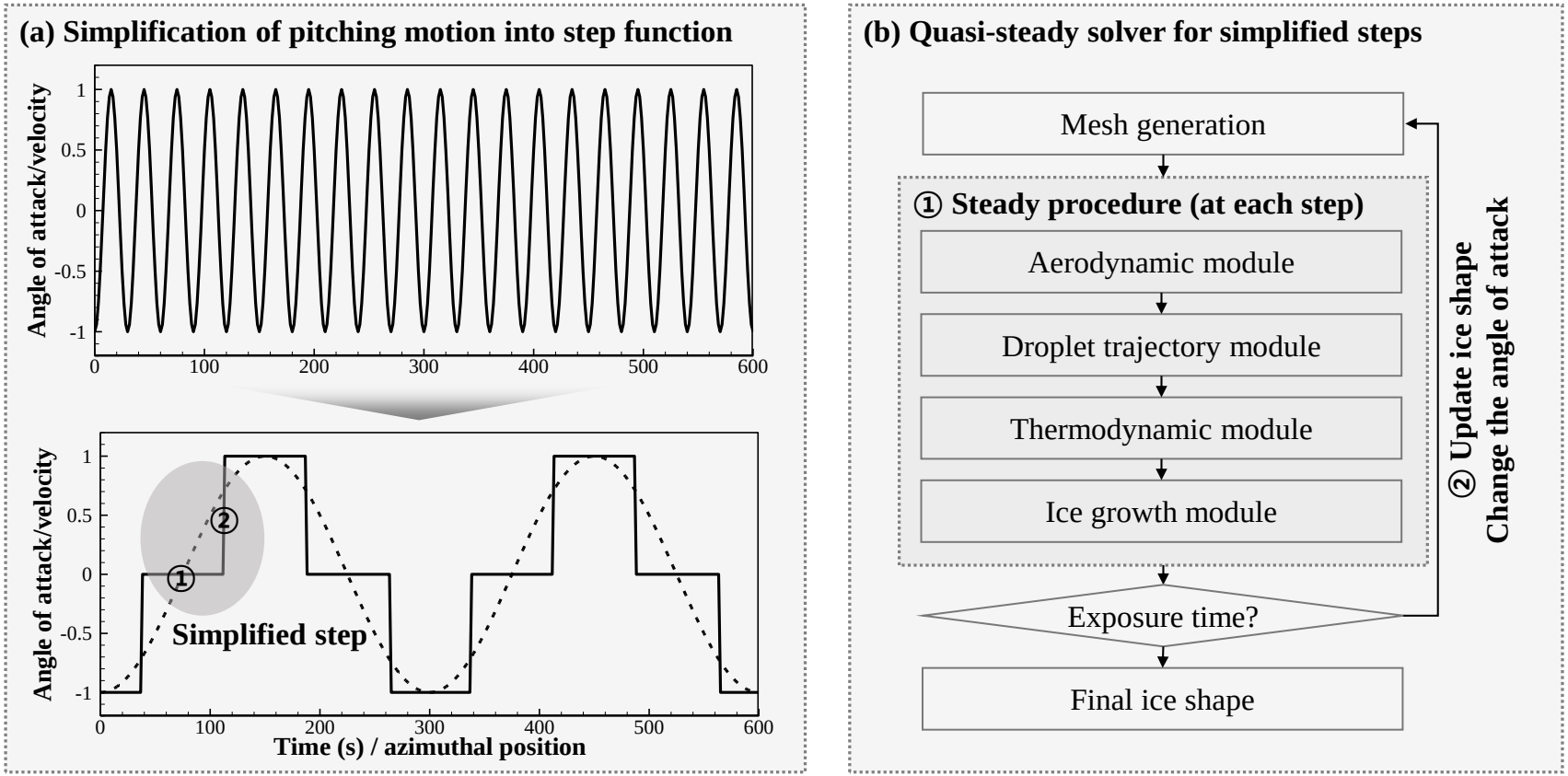

Fig. 18. Quasi-steady approach for the icing analysis of an oscillating airfoil

Chapter 4

Physics based roughness modeling

The ice growth on the airfoil induces a multi-scale shape deformation, from the apparent features such as ice horn to microscopic surface roughness. As surface roughness affects the formation of ice shape and is related to the thermal properties of the boundary layer, it has received constant attention from the inflight icing community. Since aircraft ice constantly changes shape at high speeds, it is challenging to observe microscopic roughness growth. However, experiments were conducted to observe and quantify the roughness growth process. Experimental research showed that impinging droplets and residual water film roughness determine the surface roughness of static airfoils [25-26]. Several studies have been conducted in the Icing Research Tunnel at NASA Glenn Research Center since 2014 to better understand and model the evolution of roughness during ice accretion [75-77]. With the development of laser-based technology for measuring ice thickness on an iced airfoil, the roughness distribution of the airfoil was observed using a self-organizing map (SOM) [75,78]. The results of the studies indicated the need for a roughness distribution model in an aircraft icing analysis code.

Thus, modeling for the surface roughness is a challenging issue for numerical prediction of the inflight icing. In general, the roughness element size varies from a few micrometers to a few hundred micrometers and is very small compared to the characteristic length of the objects. Accounting for the roughness shape is

impractical for computing, so inflight icing codes modeled roughness numerically and considered roughness value during icing simulations. Additionally, several assumptions regarding the unsteady characteristics are required to apply roughness to the icing code based on quasi-steady assumptions. As an initial approach, LEWICE 2.0 used the empirical correlation equation with velocity, temperature, and LWC based on 11 experimental results of Gent et al. [28]. Similarly, Shin et al. presented a correlation to consider the droplet characteristics [27]. Though the correlation yields the equivalent roughness height according to the test conditions, the approach is associated with several problems. While providing the single roughness value, the model would not resolve the physics relevant to the local surface roughness development of an iced airfoil. Also, applying it to complex shapes was not feasible based on the two-dimensional airfoil experiments [31].

Some research introduced the model with the physical insight to accurately predict ice shape and remove the arbitrariness in empirical correlations. Fortin et al. proposed the advanced surface roughness model based on 2D panel code, classifying into (1) a film, (2) a rivulet, and (3) bead states depending on the behavior of water on the surface [29]. The model was applied to first-generation aircraft icing code to predict enhancements in convective heat transfer through the Stanton analogy [30]. Ozcer extended the concept to second-generation icing code and considered roughness's effects on the surface area's increase [31].

This chapter introduces an advanced roughness model that considers local roughness affecting three-dimensional RANS-based inflight icing code. First, the

experimental evidence and concept for ice roughness are provided, and then the alternative approaches for ice roughness are briefly introduced. Based on the idea suggested by Fortin [29], this study proposes a local roughness distribution model based on an analytical solution derived from the shallow water icing model (SWIM) [32].

4.1 Physics in roughness development

In the early stages of icing, water droplets in the air attach to the aircraft surface and create surface roughness. With the number of attached water droplets increasing, some roughness flows into rivulets, and some freezes to form higher roughness. Thus, the surface roughness varies with time. The process of roughness formation has been investigated with many experimental studies [25-27]. The roughness formation can be categorized into four stages.

1) At the initial stage, impinged water droplet forms the spherical-cap-shaped bead on the surface. According to the force equilibrium between aerodynamic shear and the surface adhesion force, initially developed beads remain stationary on the surface. The newly formed bead, by continued droplet impingement, coalesced into existing droplets and grew into larger beads. As the process is reprised, beads with different sizes are formed on the surface, resulting in a complex distribution of beads.

2) The size of the bead reaches a critical size at which the aerodynamic shear force exceeds the adhesion force, and the bead starts to move. As the bead begins moving, it sweeps away other beads and agglomerates. As a result, the process is accelerated as the enlarged bead receives a greater external force.

3) As the bead moves, part of it moves slowly due to adhesion force, resulting in an elongated rivulet-like shape. The moving beads merge when the number increases, creating a water film over the surface. As water flows across the surface, rivulets and water films redistribute residing water. A change in aerodynamic force would cause the flow to stop or freeze.

4) Steps 1–3 are repeated as impinging water fills the vacant spaces where rivulets sweep. The interaction of these processes yields surface roughness, which is the product of ice and water. Droplets or runback water develop unique shapes like ice feathers and scallop icing when the roughness impinges on previously formed roughness.

Fig. 19 illustrates the steps of roughness formation by water beads. The above process can be simplified as follows to apply it to numerical simulation; (1) Calculation of bead size according to initial growth, (2) Establish the force equilibrium equation for the bead, (3) As aerodynamic shear exceeds the adhesion

force, rivulet would form. Several numerical studies presented these initial roughness formations while predicting the ice shape.

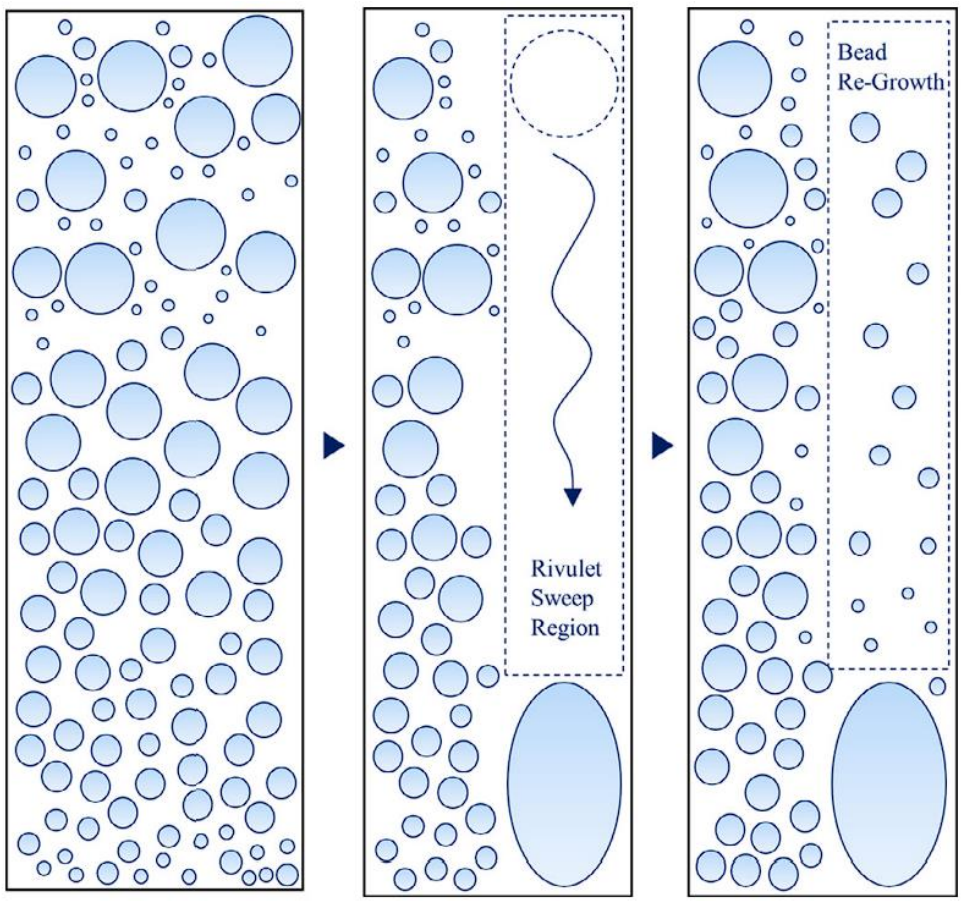

Fig. 19. Simplified roughness growth process according to bead formation

4.2 Alternative approaches

The roughness distribution of the iced surface has been considered in simulations based on theoretical and experimental research that enhances convective heat transfer and accelerates laminar-turbulent transition [79,80].

4.2.1 Multizone model

LEWICE uses different formulas for calculating convective heat transfer in smooth and rough zones as part of the IBL method that determines boundary layer characteristics. Generally, LEWICE applied the uniform roughness value from empirical correlation and formula for the rough zone, assuming the rough surface around the object. Based on the hypothesis that the smooth and rough zones correlated with the onset of the laminar-turbulent transition, Yamaguchi & Hansman applied the multizone model to the LEWICE code [80]. As an initial step, the experiment results determine laminar and turbulent zones, and smooth and rough surfaces are assumed in each zone. For subsequent calculation, the transition onset is then calculated based on the roughness Reynolds number, whose critical value is 600, assuming that the laminar zone is smooth and the turbulent zone is rough. Though the approach based on an inviscid flow solver has the advantage of computational simplicity, numerical difficulties are encountered due to limitations of the inviscid solver related to flow separation and multiple stagnation points. In addition, the physical interaction between ice accretion and the boundary layer characteristic was not considered in applying the roughness height.

4.2.2 Empirical roughness distribution model

As part of the investigation into leading-edge roughness characteristics, numerous simulation methods have been developed to apply roughness distributions to the numerical simulation of ice shapes based on experimental studies. For various 2D airfoil cases, Anderson found that the roughness height was related to the freezing fraction at stagnation [81]. The results of this study led Han & Palacios to develop a predictive correlation that can predict roughness distributions according to icing conditions [40]. According to Anderson's test data and results obtained in the Adverse Environment Rotor Test Stand (AERTS) facility, the accumulation parameter and freezing fraction are correlated to express roughness distribution. The model assumed the roughness distribution into a two-dimensional parabola. Despite the roughness distribution being included in the model, extending it to conditions outside the experimental reference range or to 3D simulations is difficult. The crude tracing technique also results in arbitrariness about the measured value.

McClain et al. eliminated arbitrariness in tracing methods for icing experiments by measuring ice thickness and roughness distribution using laser-scanning 3D ice roughness studies [75-77]. Based on the traditional scaling approaches for inflight icing, a correlation has been proposed to model transient variations in roughness characteristics. Several experimental cases demonstrated that the correlation could predict a tendency in roughness distribution, leading to McClain et al. presenting a generalized roughness correlation. However, roughness height values required refinement since they tend to overestimate or underestimate depending on the

freezing fraction in the local surface. Further work is needed to understand the interaction between the local freezing fraction, convection enhancement, and roughness formation while accounting for two- and three-dimensional local aerodynamics.

4.2.3 Physics based roughness distribution model

Various numerical studies have tried to incorporate the physics behind roughness formation into their models. At first, a roughness model based on water bead height was proposed by Fortin et al. [29]. In their study, Fortin et al. defined three types of surface states based on the remaining water mass on the surface and the impingement of the droplets. In this study, they assumed that the maximum height of a bead corresponded to the size of a bead at which aerodynamic shear, adhesion force, and gravitational force were balanced. The film state was assumed with residual water films larger than the maximum droplet height, else rivulet or film status was defined according to the impinging of the droplet.

The objective of the model was to determine the chordwise, transient roughness during ice accretion and apply it to the Stanton analogy in the IBL method to modify the convective heat transfer coefficient. The ice shapes were predicted using the 2D CIRAMIL code [82], a 1st-generation inflight icing code based on the panel method. The model suggested by Fortin et al. significantly presented a general approach that can consider physical attributes, whereas the existing roughness model provided numerical values through empirical correlation.

The numerical studies were conducted to extend the roughness model of the water bead concept to the 2nd generation inflight icing code. Croce et al. configured the beading process on the surface through the Lagrangian method and applied the maximum bead height while computing the SWIM models in the thermodynamic module [83]. The surface roughness of a plate was calculated using the Lagrangian method by tracking the motion of each droplet. Applying the Lagrangian method to all of the droplets requires considerable computational resources. Therefore, the model was not used for aircraft icing codes but has laid a heuristic approach for advanced modeling based on physical phenomena. Ozcer [31] extended the concept to second-generation icing code and considered the effects of roughness on the increase in surface area. Based on past research, this study proposes a local roughness distribution model based on a maximum bead height. This model did not link the roughness height to the RANS equation but assumed that roughness increased the surface area to maintain the quasi-steady manner of the inflight icing code. As a result, the roughness distribution based on the water bead model could be applied to the 2nd generation inflight icing code without the massive computational overhead. Considering the theoretical evidence that roughness blocks flow and increase skin friction, the above assumptions lowered the model's physical validity when accounting for roughness effects on flow and heat transfer.

4.3 Local surface roughness modeling

The proposed roughness-induced transition model requires local roughness information in the prediction of transition onset. Generally, the roughness model categorizes the state of the surface into smooth and rough zones, and computes roughness for each control surface. The concept of this model was originally proposed by Fortin et al. [29], who divided the surface state into (1) a film, (2) a rivulet, and (3) states of beads depending on the behavior of water on the surface. To apply this concept to a second-generation inflight icing code, the roughness model follows two steps: (1) calculating maximum bead height, and (2) predicting the behavior of water.

4.3.1 Maximum bead height

The maximum bead height ($h_{b,max}$) refers to the height just before a bead of water starts moving, and acts as a criterion for distinguishing among beads, rivulets, and films of water based on its volume on the control surface. The maximum bead height is computed from the equation of equilibrium of force. As shown in Fig. 20, a spherical cap shape was applied to represent the bead, and was subjected to gravity and aerodynamic shear acting as external forces, with the surface tension as the reactive force. Placing the external force on the right and surface tension on the left side yields Eq. (10). $\theta(\varphi)$ in the expression for surface tension force stands for the contact angle along the contact line. Croce et al. [33] expressed the surface tension with respect to the advancing and receding contact angles based on the polynomial

expression of $\theta(\varphi)$ developed by El Sherbini and Jacobi [84]. Therefore, Eq. (10) becomes Eq. (11). The average, advancing, and receding contact angles are based on experiments by Hansman and Turnock [26]:

$$\int_0^{\pi} \sigma_w \cos\big(\theta(\varphi)\big) \cos(\varphi)\, r_b d\varphi = \rho_b g V_b + \frac{1}{2}\tau_w A_b + \int \frac{dp}{dx_i} dV_b \qquad (10)$$

r_b = bead radius, A_b = bead surface, V_b = bead volume, θ_c = contact angle

$$\frac{24}{\pi^3}\sigma(\cos\theta_{adv} - \cos\theta_{rec}) h_b \frac{\sin\theta_c}{1-\cos\theta_c} = \rho_b g V_b + \frac{1}{2}\tau_w A_b + \int \frac{dp}{dx_i} dV_b \quad (11)$$

θ_{adv} = advancing contact angle, θ_{rec} = receding contact angle

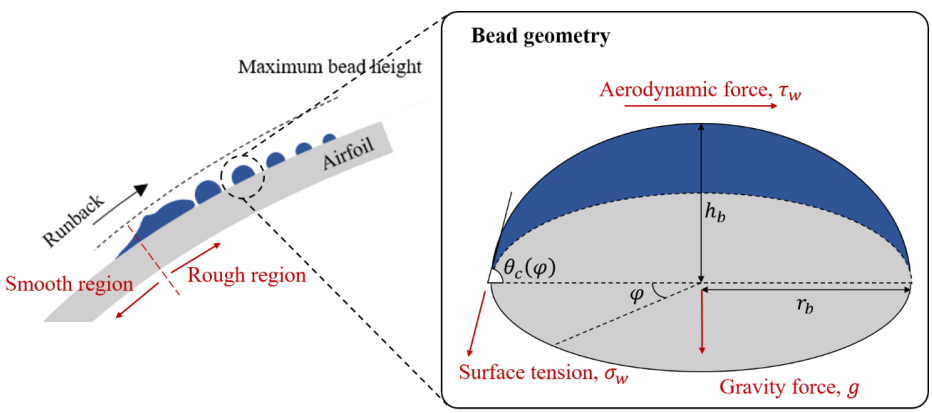

Fig. 20. Schematic view of the spherical bead geometry [85]

4.3.2 Water film behavior

Water behavior is categorized into water film, rivulet, and stationary bead. The water behavior was demonstrated by coupling with the governing equations of the thermodynamic module. Since, the present model is available for the glaze ice condition where water and ice coexist on the surface, the surface temperature is set to 0°C. At this condition, $\dot{m}_{ice}$ is computed from the energy equation of the thermodynamic module as in Eq. (4). Using the $\dot{m}_{ice}$ value, water behavior on the surface is predicted from the mass equilibrium equation of the thermodynamic module as in Eq. (3). Since the roughness growth is transient phenomena, the thermodynamic module and present roughness model is timely solved for whole ice accretion time.

At the initial stage of icing, water droplets in the air are attached to the aircraft surface in the form of stationary beads ($u_f = 0$) after impact. During this stage, bead height, h_b is expressed by following equation. f_{shape} is the factor defined from the spherical bead shape analogy. When the bead shape is converted to the same volume of water film, f_{shape} is obtained from the ratio of the bead and film height.

$$h_b = \frac{1}{f_{shape}} \frac{1}{\rho_w} \left(\dot{m}_{imp} - \dot{m}_{ice} - \dot{m}_{eva} \right) \Delta t \tag{12}$$

$$f_{shape} = \sqrt{\frac{\theta_c - \sin\theta_c \cos\theta_c}{2 \sin\theta_c}} \tag{13}$$

While h_b represents the bead height, it also indicates the water mass forming the rough zone per unit surface. According to Olsen and Walker's observation [25], insipient movement of the water occurs when the average radius of the bead reaches 65% of the threshold. Therefore, in this study, we applied the mass equilibrium equation of the thermodynamic model to analyze the water flow on the surface, after the h_b reaches the $h_{b,max}$. Water flows in the rivulet form at the initial stage, and the rivulet height, h_{riv} is defined as follows.

$$h_{riv} = \left(0.65 + \frac{1}{0.85}\frac{1}{f_{shape}}\frac{h_f}{h_{b,max}}\right)h_{b,max} \tag{13}$$

When the height of the rivulet reaches $h_{b,max}$, it is assumed that the rivulet flow is converted to film flow. The film roughness, h_{film} is calculated by the Eq. (14) which is the wave equation [86] adopted by Fortin et al. [29].

$$h_{film} = \frac{3}{4}\frac{\tau_w}{\mu_w}\sqrt{\frac{{h_f}^3}{g}} \tag{14}$$

According to the Ozcer [31], the roughness formation which assumes bead type roughness covering up to 85% of the local surface resembles the sand-grain roughness. As present roughness model follows the bead type roughness concept as in Ref. [31], the ice roughness height obtained was taken to be the equivalent sand-

grain roughness. The roughness height computed from the model is directly applied to the wall boundary condition of the turbulent model and aforementioned roughness-induced turbulence model.

4.3.3 Implementation of roughness model in ICEPAC

This study partially applied a quasi-unsteady approach to examine the effect of roughness distribution on aerodynamic modules. In Fig. 21, an aerodynamic module sequentially linked with a droplet trajectory module is shown transferring data three or four times with the thermodynamic model, including roughness modeling. The different time steps caused by the speed difference between the airflow and droplet fields and the thermodynamic water film are the reason for not tightly coupling each module simultaneously. The roughness height and ice accretion rate were calculated with the converged solution of the aerodynamic and droplet modules. Then the roughness data was then substituted into the turbulent model. Three to four data transfers were repeated to reach the ice shape for a single shot. This method considers that roughness impacts the boundary layer and enhances heat convection instead of assuming that the roughness distribution model increases the surface area as shown in previous studies with 2^{nd} generation code.

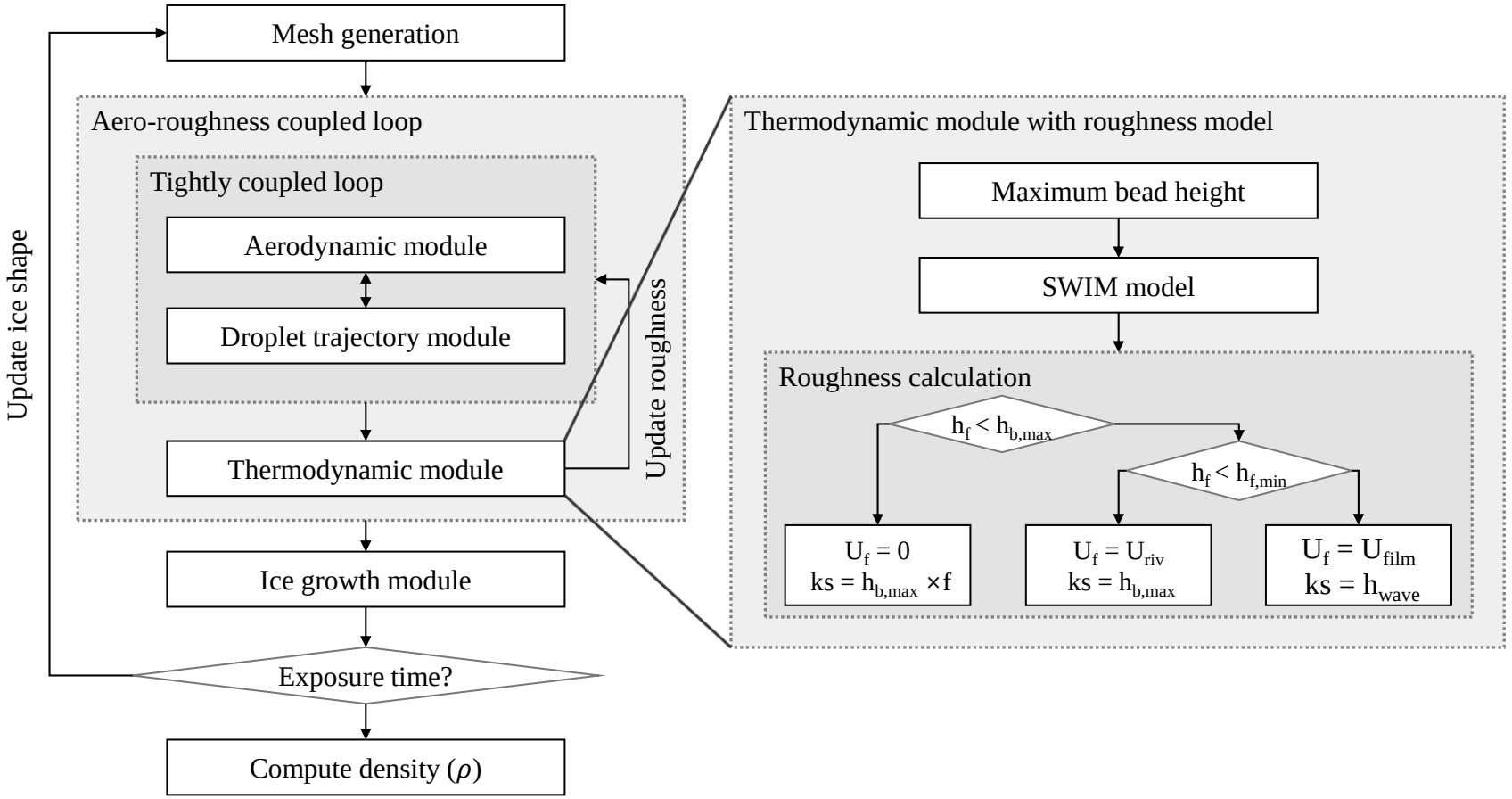

Fig. 21. Implementation of physics based roughness model on ICEPAC

Chapter 5

Roughness induced transition model

A thermodynamic module of inflight icing code simulates the balance out of latent heat caused by solidification on the surface. Various energy components are involved in the process, including droplet kinetic energy and evaporation energy, but convective heat transfer dominates. As the thermodynamic driving force generates the heat flux of the flow, the surface roughness affects the heat transfer rate when hampered by the surface roughness. As inflight icing is accompanied by roughness contamination, modeling the impact of roughness on convective heat transfer would improve the accuracy of numerical solutions.

The surface roughness is responsible for the two significant impacts on inflight icing: shifting the transition location upstream and increasing local convective heat transfer. Studies have shown that such surface roughness influences the leading edge of an airfoil. Poinsatte et al. measured the local heat convection coefficient for the smooth NACA0012 airfoil, then measured the effect of roughness element on heat convection using artificial roughness [87,88]. Bragg & Kerho [89] conducted an experimental study on the impacts of distributed roughness near the leading edge of an airfoil. They concluded that roughness triggers the premature laminar-turbulent transition.

Inflight icing codes attempted to model the roughness effect through various numerical models. Using a panel method-based aerodynamic solver and an IBL

method, LEWICE 2.0 investigated the increment of heat transfer due to surface roughness [8]. The code divided the laminar and turbulent regimes based on the Reynolds number of the boundary layer at the onset of the transition. Second-generation codes based on the RANS solver accounted for the roughness effect through the wall function of the turbulence model. The codes usually assumed a fully turbulent regime around an iced airfoil or distinguished laminar and turbulent regimes through a fixed-transition point. Most numerical simulations consider the increase in convection heat transfer with roughness but rarely the transition between laminar and turbulent regimes. As Habashi pointed out, the laminar transition required to be physically modeled to improve the accuracy of inflight icing simulations [13].

5.1 Alternative approaches

Although experimental studies have shown the need for measuring the heat transfer coefficient by using surface roughness and the resulting transition, few numerical models of roughness-induced transition have been developed.

5.1.1 1st generation icing code with inviscid flow solver

1st generation inflight icing codes used an inviscid flow solver to predict the point of transition using the IBL method [8]. Boundary layer calculation starts from the stagnation point, is assumed to have zero boundary layer thickness at that point, and is assumed to be laminar until the transition occurs. The transition onset was

determined by a correlation based on the roughness Reynolds number Re_{ks} [90]. Then, momentum thickness and heat convection coefficient for each control volume are calculated through analytical solution. The method of calibration used for the empirical correlation might not enable an accurate prediction of the shape of ice for conditions not considered for the calibration. Based on the first-generation code, a numerical model considering local roughness and roughness-induced transitions was first proposed by Yamaguchi & Hansman [80]. Based on experimental observations, smooth/rough zones were initially defined for the glazed ice. The deterministic surface roughness transition model was then applied to link the smooth/rough transitions with the laminar–transition in turbulence. Although the approach based on inviscid flow solver has the advantage of computational simplicity, numerical difficulties are encountered due to limitations of the inviscid solver related to flow separation and multiple stagnation points. Heat transfer analysis and transition position prediction through IBL method and roughness Reynolds number have difficulty predicting heat convection coefficient at the high Reynolds number. Also, the immediate growth of heat transfer due to roughness in this method is different from the actual phenomenon.

5.1.2 2nd generation icing code with RANS equation

2nd generation icing code, a coupled CFD/ice-accretion solver, delivers a roughness effect through the turbulent model. Most icing codes assume a fully turbulent environment around the object and consider roughness enhancement by

modifying the turbulent model and boundary conditions on the wall around the object. The Spalart-Allmaras model was used to model the roughness-induced transition between laminar and turbulent flows in FENSAP-ICE [11]. The transition position is predicted through the coefficients used in the trip term, which was determined through a priori or educated guess. By coupling the $k-\omega\ SST$ model to the $\gamma - Re_{\theta}$ model, it is possible to predict the free transition. Still, the model was not applied to the icing code since the methods for accounting for the roughness effect were unavailable. Due to the limitations of the existing numerical methodology, the aircraft icing simulation does not model the physical properties, such as initial surface roughness and corresponding changes in the transition acceleration and heat transfer. This is one reason for failing to simulate the critical features of aircraft icing, such as ice horns or ice formations on the ice surface under freezing conditions.

5.2 Roughness induced transition modeling

The research focused on the implementation of transition turbulence model on the inflight icing code so as to improve ice accretion shape and performance prediction accuracy.

5.2.1 Roughness amplification parameter, A_r

A roughness amplification parameter (A_r) is a non-physical value that describes the effects of surface roughness on the flowfield. This variable represents the propagation of roughness-induced perturbations into the field in order to calculate the momentum deficit at the boundary layer and modify the criteria for transition onset. The flowfield affected by roughness is defined with A_r transferred through a convective equation and connected to the $\gamma - Re_\theta$ transition model. As the equation is designed to convect turbulent kinetic energy away from the roughness, an experimentally observed lag occurs between encountering the rough section and its effect on the mean boundary layer.

The behavior of the $\gamma - Re_\theta$ model strongly depends on the boundary layer's momentum thickness. As the Re transport equation calculates a local value for critical momentum thickness Reynolds number from experimentally known value, A_r involves this process to alter transition onset decision. A simplified definition of momentum thickness of incompressible flow was used to explain the relationship between A_r and momentum thickness Reynolds number.

$$\theta = \int_0^{\infty} \frac{u(y)}{u_0}\left(1 - \frac{u(y)}{u_0}\right) dy \tag{15}$$

An Eq. (15) represents the momentum thickness of a smooth surface. Taking theta rough as the momentum thickness above roughness and subtracting the value from theta, $\Delta\theta$ can be expressed as the effect of roughness on momentum thickness. The amount of change in momentum thickness due to roughness can be calculated by applying the linear varying near-wall velocity assumption, as shown in Eq. (16).

$$\Delta\theta = \theta - \theta_{rough} = \frac{1}{2u_0} k_s^2 \left(\frac{\tau_w}{\mu}\right) - \frac{1}{3u_0^2} k_s^3 \left(\frac{\tau_w}{\mu}\right)^2 \tag{16}$$

The following equation can be derived based on the definitions of non-dimensional roughness height k^+, momentum thickness Reynolds number, and Re_θ.

$$Re_{\theta,rough} = Re_\theta + \frac{1}{3} u^+ (k^+)^3 - \frac{1}{2} (k^+)^2 \tag{17}$$

Assuming that A_r is a linear function of k^+ and that c_{r1} is a constant coefficient, Retheta can be expressed in terms of A_r.

$$Re_{\theta,rough} = Re_\theta + \frac{1}{3} u^+ \left(\frac{A_r}{c_{r1}}\right)^3 - \frac{1}{2}\left(\frac{A_r}{c_{r1}}\right)^2 \tag{18}$$

The momentum Reynolds number and momentum thickness increase with the increment of surface roughness, as illustrated by the cubic function for A_r. In the $\gamma - Re_\theta$ model, the critical momentum Reynolds number is determined by the Re_θ equation. Similar to increasing the momentum Reynolds number, the A_r variable can be applied to the $\gamma - Re_\theta$ model to reduce the critical momentum Reynolds number.

5.2.2 Modifying turbulence model

The computational attempt to account for the effects of roughness involves modifying the near-wall turbulent viscosity according to the relative roughness height. A similar approach has been used for the second-generation inflight icing code [37, 38]. However, turbulent boundary layers can be modified for the flow field of a fully turbulent regime.

In this study, to simulate the influence of roughness on the transition in turbulence, a A_r introduced by Dassler, Kozulovic, & Fiala [42] was implemented in the form of a transport equation. The turbulence model is constructed by coupling the A_r transport equation with the transitional $\gamma - Re_\theta$ model and the two-equation *k-ω SST* turbulence model. Through this, a robust computational approach is introduced to simulate the characteristics of flow as influenced by surface roughness. The modeled roughness-induced transition is integrated into the turbulence model of the aerodynamic module in ICEPAC as shown in Fig. 22.

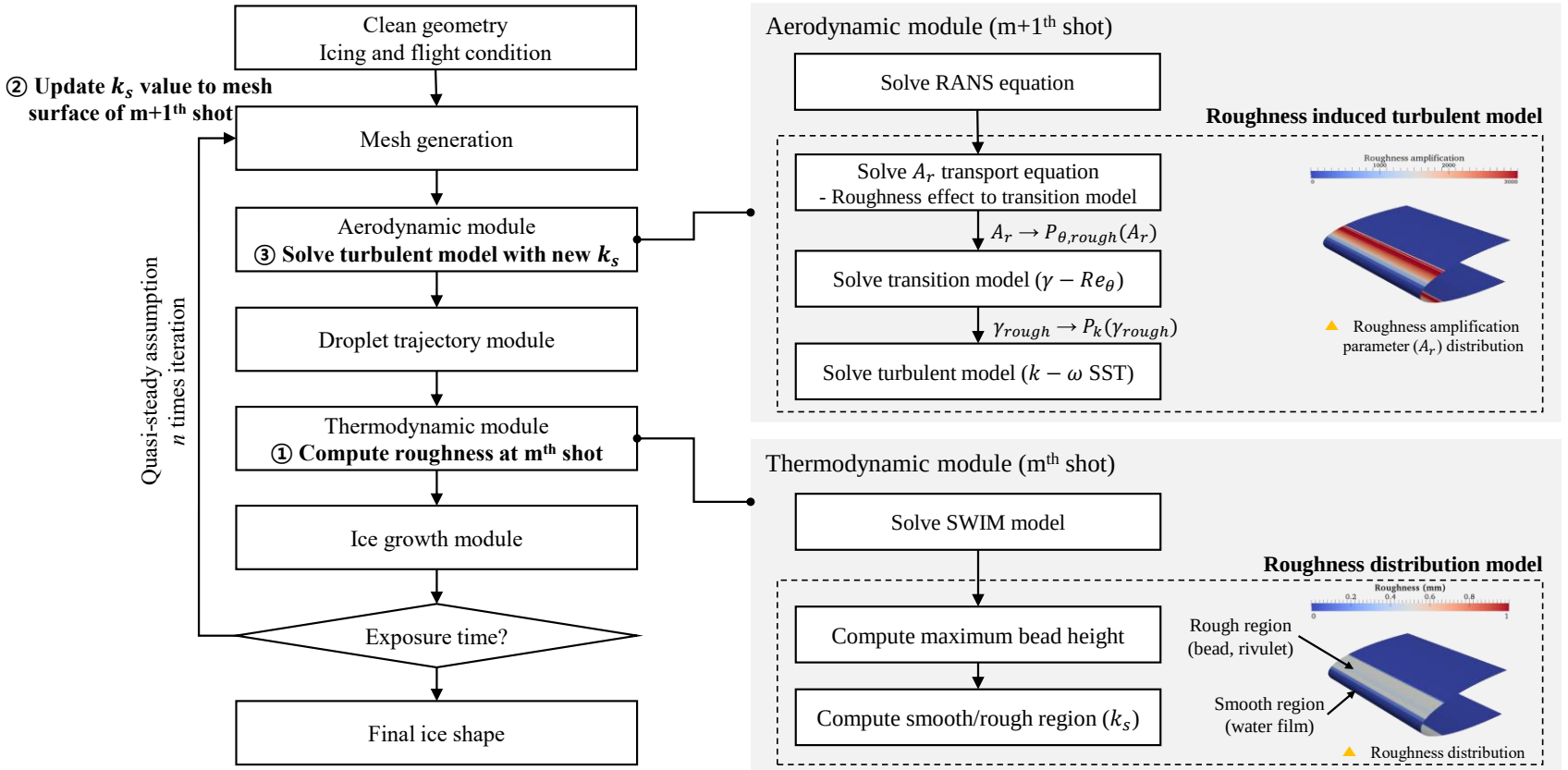

Fig. 22. Implementation of the roughness-induced transition model in ICEPAC

The variable A_r is defined using the non-dimensional height of roughness k^+ as given in Eq. (19), amplified by the constant parameter c_{Ar1}. Eq. (19) is the boundary condition of the wall for the A_r transport equation, which is given in Eq. (20). The formation of the transport equation is similar to that of the transition model without any production or dissipation term; thus, the height of roughness is the primary influential factor.

$$A_r|_{wall} = c_{A_r1}k^+ \tag{19}$$

$$\frac{\partial(\rho A_r)}{\partial t} + \frac{\partial(\rho U_j A_r)}{\partial x_j} = \frac{\partial}{\partial x_j}\left[\sigma_{A_r}(\mu + \mu_t)\frac{\partial A_r}{\partial x_j}\right] \tag{20}$$

The value of A_r is linked with the $\gamma - Re_\theta$ model through the production term, $P_{\theta_t,rough}$, of the Reynolds number ($\widetilde{Re}_{\theta_t}$) of the thickness of the transition onset momentum. F_{A_r} in Eq. (22) reduces the local critical value for the transition onset, $\widetilde{Re}_{\theta_t}$, by lowering $P_{\theta_t,rough}$, and thus accelerates the transition. F_{A_r} is expressed in the polynomial function of $\mathrm{A_r}$ as shown in Eq. (23), which was correlated in Ref. [44].

$$\frac{\partial(\rho\widetilde{Re}_{\theta_t})}{\partial t} + \frac{\partial(\rho U_j\widetilde{Re}_{\theta_t})}{\partial x_j} = P_{\theta_t,rough} + \frac{\partial}{\partial x_j}\left[\sigma_{\theta_t}(\mu + \mu_t)\frac{\partial\widetilde{Re}_{\theta_t}}{\partial x_j}\right] \tag{21}$$

$$P_{\theta_t,rough} = c_{\theta_t}\frac{\rho}{t}\left[\left(Re_{\theta_t} - \widetilde{Re}_{\theta_t}\right)\left(1 - F_{\theta_t}\right) - F_{A_r}\right] \tag{22}$$

$$F_{A_r} = \begin{cases} c_{A_r2}\,(A_r)^3 & : \quad A_r < C_{A_r} \\ c_{A_r3}\left(A_r - C_{A_r}\right) + c_{A_r2}C_{A_r} & : \quad A_r \geq C_{A_r} \end{cases} \tag{23}$$

$$c_{A_r1} = 8.0 \quad c_{A_r1} = 0.0005 \quad c_{A_r3} = 2.0 \quad C_{A_r} = \sqrt{c_{A_r3}/3c_{A_r2}}$$

The Reynolds number for vorticity is computed from $\widetilde{Re}_{\theta_t}$, and intermittency ($\gamma$) production is then triggered. The Reynolds number for vorticity affects the transition onset function, F_{onset}, and accelerates the transition. For the transitional region length, F_{length}, the original calibration by Langtry & Menter is used [91]. The model can thus represent the effects of roughness on the transition onset. The transport equation of γ and the production term, P_γ, are given as below. The detailed process of the model is provided in work by Menter et al. [91]:

$$\frac{\partial(\rho\gamma)}{\partial t} + \frac{\partial(\rho u_j\gamma)}{\partial x_j} = P_\gamma - E_\gamma + \frac{\partial}{\partial x_j}\left[\left(\mu + \frac{\mu_t}{\sigma_f}\right)\frac{\partial\gamma}{\partial x_j}\right] \tag{24}$$

$$\mathrm{P}_\gamma = F_{length}c_{a1}\rho S[\gamma F_{onset}]^{0.5}(1 - c_{e1}\gamma) \tag{25}$$

$$\frac{\partial(\rho k)}{\partial t} + \frac{\partial\left(\rho u_j k\right)}{\partial x_j} = \gamma_{eff}P_k - min\left(max\left(\gamma_{eff}, 0.1\right), 1.0\right)D_k + \frac{\partial}{\partial x_j}\left[(\mu + \sigma_k\mu_t)\frac{\partial k}{\partial x_j}\right] \tag{26}$$

The computed γ is fed into the turbulent kinetic energy equation of the $k-\omega$ SST model as a production term as shown in Eq. (26). The growth in the turbulent kinetic energy is affected by γ, which initiates the laminar–turbulent transition that is influenced by the local disturbance in surface roughness.

5.2.3 Applying model to in-flight icing code

In addition to affecting the location of the transition, surface roughness enhances the shear stress on the wall and heat transfer coefficient in the fully transitional boundary layer. The boundary condition of the $k-\omega$ SST turbulent model is modified for both the turbulent kinetic energy (k) and the rate of turbulent dissipation (ω). When the height of roughness is expressed as a dimensionless roughness Reynolds number, roughness generated near the leading edge of the airfoil was 1000. To consider this value, the boundary condition proposed by Aupoix [38] based on experimental data by Colebrook and White [32] was applied, as shown in Eq. (28) and (29):

$$\frac{\partial(\rho\gamma)}{\partial t}+\frac{\partial(\rho u_j\gamma)}{\partial x_j}=P_\gamma-E_\gamma+\frac{\partial}{\partial x_j}\left[\left(\mu+\frac{\mu_t}{\sigma_f}\right)\frac{\partial\gamma}{\partial x_j}\right] \tag{27}$$

$$k_w^+=max(0,k_0^+)$$
$$k_0^+=\frac{1}{\sqrt{\beta^*}}tanh\left[\left(\frac{ln\,k_s^+/30}{ln\,10}+1-tanh\frac{k_s^+}{125}\right)tanh\frac{k_s^+}{125}\right] \tag{28}$$

$$\omega_w^+ = \frac{300}{k_s^{+2}}\left(tanh\frac{15}{4k_s^+}\right)^{-1} + \frac{191}{k_s^+}\left(1 - exp\left(-\frac{k_s^+}{250}\right)\right) \tag{29}$$

The modified boundary condition affects the calculated turbulent viscosity and, thus, the convective heat transfer coefficient. The turbulent viscosity is calculated from the turbulence model, which affects thermal conductivity. The convective heat transfer coefficient, which is an important parameter for determining the shape of ice, is calculated from the thermal conductivity and temperature gradient. Because the rate of ice accretion is determined by heat exchange at the surface, increasing The convective heat transfer coefficient affects the accuracy of the analysis:

$$h_{cv} = -k_{eff}\frac{\partial T}{\partial n}\left(\frac{1}{T_{sur} - T_\infty}\right) \tag{30}$$

Convective heat transfer balances the latent heat of solidification in the air and appears as the source term of the energy equation of the thermodynamic module. Therefore, the surface roughness from the present model changes the heat convection coefficient through the turbulence model, which in turn influences the ice shape by the energy equation of the thermodynamic solver.

Chapter 6

Verification and validation

In this section, previously introduced models are validated by comparing them with published experimental results. As validation results are unavailable for some cases, some models were verified with published numerical results.

6.1 Quasi-unsteady approach

The quasi-unsteady icing code configured the unsteady loop with 1) the aerodynamic, 2) droplet trajectory, 3) thermodynamic modules, and implemented the oscillating motion through the dynamic motion solver. As the present study simulated the icing experiment on an oscillating airfoil with an angle of attack of 5 and 10 degrees, the aerodynamic module and droplet impingement module was validated for light stall cases with similar angles of attack to the icing case, as shown in Table 4. The first case simulated oscillating NACA0015 airfoil with a smooth surface, and the study of Dumlupinar & Murthy was referred to validate the dynamic motion solver [93,94]. The second case compared the aerodynamic coefficient of the S809 airfoil with the leading-edge roughness to verify whether the current solver accounts for the effect of leading-edge roughness that occurs during icing [95,96]. As there was no validation result for collection efficiency on an oscillating airfoil, the third case verified the droplet impingement module by comparing the numerical collection efficiency of SC2110 airfoil computed by Fouladi [23]. The validation

result for the original ICEPAC would be found in Ref. [97], which introduced the basic ICEPAC and applied it to fixed-airfoil.

Table 4. Verification and validation case for quasi-unsteady approach

Airfoil	Chord length (m)	Airspeed (m/s)	Angle of attack (°)	Frequency (Hz)
NACA0015	0.3054	100	11±4	10
S809	0.55	40	10±6	1.6
SC2110	0.381	77.167	5±6	2.8

6.1.1 Oscillating NACA 0015 airfoil with a smooth surface

The motion solver was validated using a smooth oscillating airfoil. Based on the PIMPLE solver of OpenFOAM, the dynamic mesh technique, which solves the Laplacian equation, was applied to an oscillating NACA0015 airfoil. The light stall case was selected to match a similar range of attack used in the icing analysis. The airfoil had a chord length of 0.3054 m, Reynolds number of approximately 2 million, and Mach number of 0.3. The oscillating angle was in the range of 7–15°. The oscillating frequency was 10 Hz and respectively. For the numerical simulation, a hybrid grid system was applied with 600 points along the surface with 120,000 meshes and a far-field domain that is 20 times the chord length. The simulation applied the turbulence model, and the near-wall grid spacing was computed as $y^+ = 0.35$. The $k-\omega$ shear stress transport (SST) model was used for turbulent model.

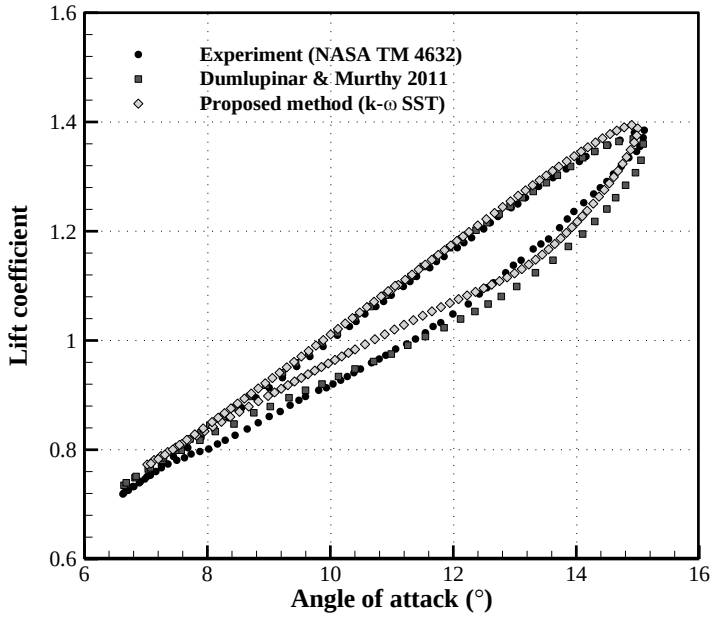

(a) Lift coefficient

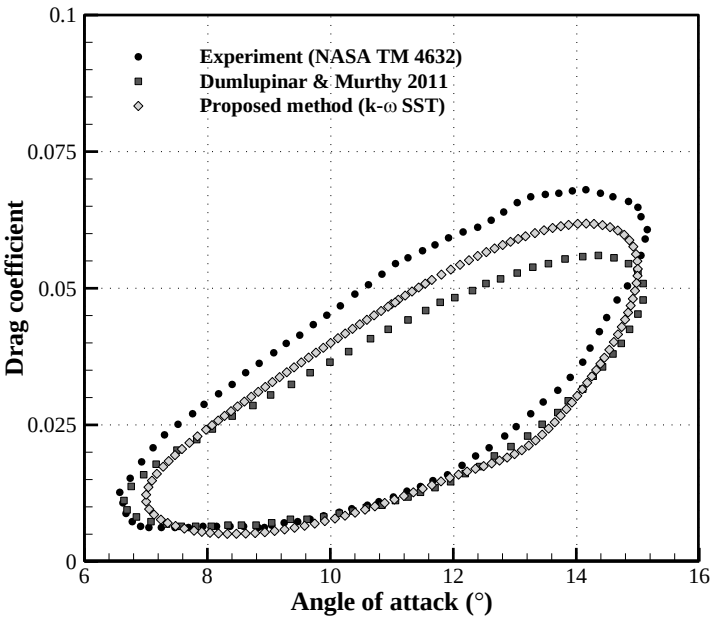

(b) Drag coefficient

Fig. 23. Comparison between the aerodynamic coefficients of an oscillating airfoil and a smooth surface [94]

Fig. 23 compares the aerodynamic performance computed using the proposed method with those obtained from the experimental [93] and numerical results reported by Dumlupinar and Murthy [94]. In the Fig. 23, the black circle is the experimental value, black square is the numerical result from Ref. [94], and gray diamond is the value calculated using the present method. The results showed that the Laplacian dynamic mesh solver and aerodynamic solver reliably derived solutions. The proposed numerical simulation accurately predicted the hysteresis loop for the lift and drag coefficients. The upstroke process increased linearly in the form of an attached flow. When the angle of attack approached the peak, the flow separated and remained separate during the downstroke, which caused the hysteresis effect.

6.1.2 Oscillating S809 airfoil with leading-edge roughness

A previous study by Min and Yee numerically demonstrated that the roughness near the leading edge in in-flight icing affects the ice shape owing to the boundary layer development and the consequent change in the convection heat transfer coefficient [85]. Therefore, the leading-edge roughness also affects the transition and flow separation in the oscillating airfoil. In this study, the roughness-induced transition model associated with the present motion solver was validated by comparing the aerodynamic performance of an oscillating airfoil with the leading-edge roughness on wind-turbine airfoils reported in previous studies.

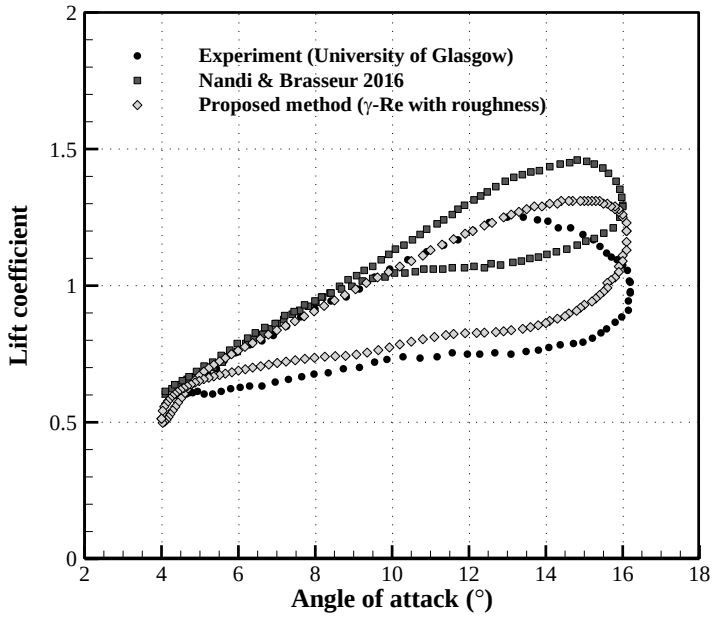

(a) Lift coefficient

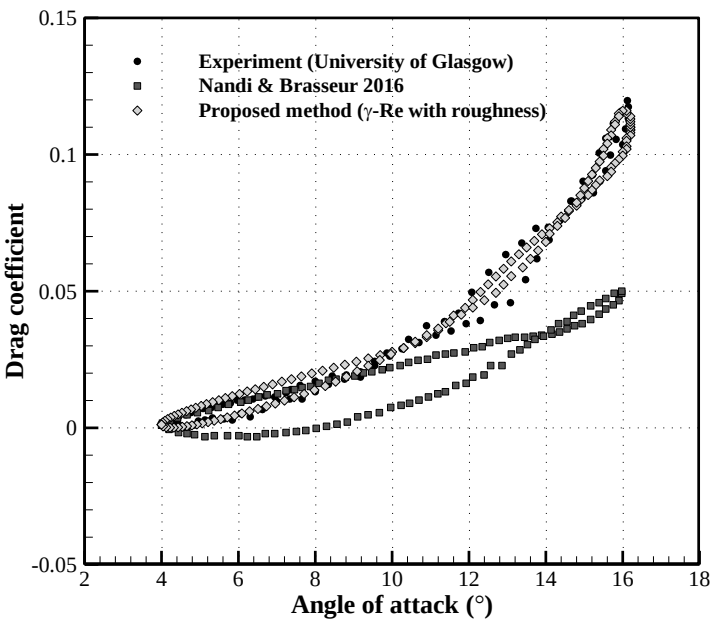

(b) Drag coefficient

Fig. 24. Comparison between the aerodynamic coefficients of an oscillating airfoil with leading-edge roughness [95,96]

Experiments performed at the University of Glasgow were used to assess the numerical techniques in this study [95,96]. The model used was a partially roughened S809 airfoil with a chord length of 0.55 m and Reynolds number of approximately 1.5 million, and Mach number of 0.15. The oscillating angle was in the range of 4–16° with reduced frequency, which was selected as the light stall case. The leading-edge roughness was modeled according to 60-grit sandpaper placed from 2.5 % on the lower surface up to 3.5 % chord on the upper surface. For the numerical simulation, a hybrid grid system was applied with 800 points along the surface with 160,000 meshes and a far-field domain of 20 times the chord length. As present case simulated the partial roughness, the minimum grid spacing was used up to the rough region to prevent numerical instability caused by rapid fluctuations k (turbulent kinetic energy) and ω (dissipation rate). Thus, the simulation used 800 surface grid points and $y^+ = 0.35$ for near-wall grid height unlike other cases. For boundary layer transition analysis, the roughness-induced transition model, which couples the Ar equation with the four-equation transition model by Langtry & Menter [91], was used to account for the roughness effect. The wall boundary conditions for k and ω in the rough zone followed the model proposed by Knopp et al. [58]. For the smooth zone, k was set to zero and ω was computed according to [96]. The turbulent intensity was set to 1.5 % for the inlet boundary condition of k.

Fig. 24 compares the aerodynamic performance computed using the proposed method with that obtained from the experimental and the numerical results reported by Nandi and Brasseur [95,96]. The black circular symbols represent the

experimental values reported by the University of Glasgow [95], and the dark and light grey squared symbols represent the numerical results reported by Nandi and Brasseur [96] and the present study, respectively. The current numerical simulation similarly predicted the hysteresis loop of the lift and drag coefficients. In the upstroke process, the stall onset on numerical lift curves is delayed compared to the experimental value which is attributed to the delay in the separation of flows during the upstroke and the faster reattachment of downstroke flows, resulting in over-prediction of lift coefficient at a higher angle of attack. Compared with the numerical results of Nandi & Brasseur [96], the current model closely approximates the experimental value. In the present study, in addition to Langtry & Menter's transition model used by Nandi & Brasseur [96], the transport equations for roughness amplification parameters were integrated to consider the effects of leading-edge roughness on transition. Accordingly, the present study predicts a high drag coefficient, as shown in Figure 24(b), since roughness accelerates flow separation. Thus, the current aerodynamic solver can reliably consider the roughness effect, which is essential for the icing phenomenon of oscillating motion.

6.1.3 Collection efficiency of the oscillating airfoil

As there were no available experimental data for collection efficiency on the oscillating airfoil, the present study verified the collection efficiency by comparing it with the numerical results obtained by Fouladi [23]. The case used was Run 36 in the experiments performed by Reinhart et al., and the icing conditions were liquid water content (LWC) = 0.55 g/m^3 and median volume diameter (MVD) = 22 μm [21]. For the numerical simulation, a 2D hybrid grid of the SC2110 airfoil with an angle of attack of $5\pm6^{\circ}$ was used with 600 points along the surface, and the near-wall grid spacing was $y^+ = 1$. For the accurate prediction of the impingement area, the grid points were clustered for 10 % of the chord length from the leading edge.

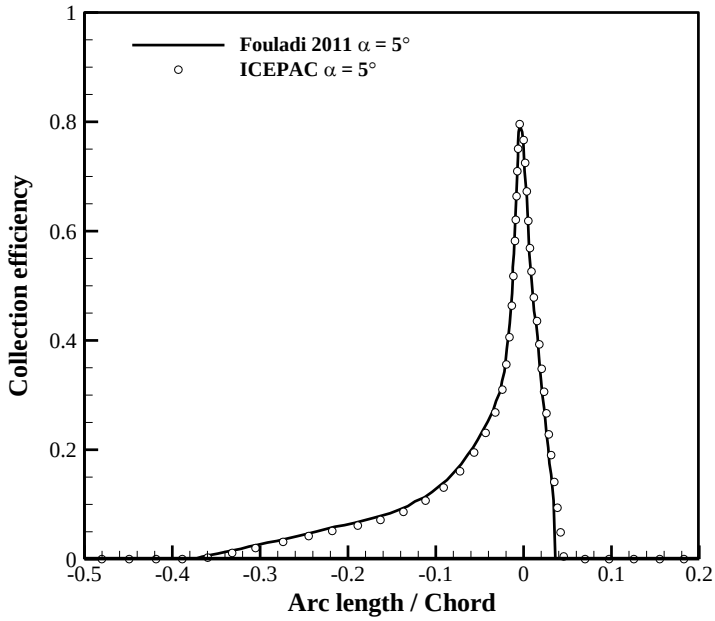

(a) Quasi-steady solver

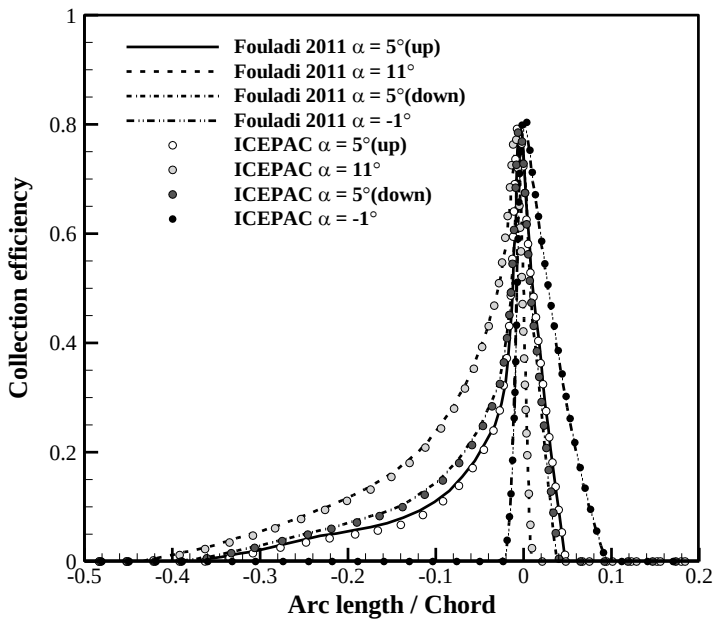

(b) Quasi-unsteady solver

Fig. 25. Verification of the droplet impingement module for the quasi-steady and quasi-unsteady solver [23]

First, to solely verify the droplet impingement module, Fig. 25(a) compares the collection efficiency of the fixed airfoil at an angle of attack of 5°. The results compared the values obtained using the original ICEPAC with those reported in Ref. [23], which confirmed that these results are consistent. Fig. 25(b) shows the collection efficiencies according to the oscillating angle of attack. The lines denote the numerical results obtained by Fouladi [23]. The solid and dotted dashed lines indicate the upstroke and downstroke at the mid-angle of attack, respectively, and the dashed line and dashed line with a double dot indicate the values at high and low angles, respectively. The circular symbols with different colors present those of the modified ICEPAC. Fouladi [23] applied a tightly coupled multiphase solver for the airflow and droplet fields. Although the present study considered the effect of airflow on the droplet field using a one-way coupling technique based on a segregated solver, the results were in a good agreement with the reference. Therefore, if the diameter and density of the super-cooled droplets that caused icing were considered, applying one-way coupling can also be an adequate method to derive an accurate collection efficiency.

6.2 Laminar-turbulent transition

6.2.1 Flat plate case

The proposed roughness-induced transition model is formulated based on an experiment involving a partially roughened flat plate conducted by Feindt et al. [43]. As shown in Fig. 26, the model has a Reynolds number of 1.3 million, and roughness is partially applied from chord 0.03 of the plate with a roughness Reynolds number ($Re_k = \frac{\rho U_\infty k_s}{\mu}$) ranging from zero to 330. For numerical analysis, the intensity of turbulence was set to 0.91% based on numerical research by Dassler et al. [42].

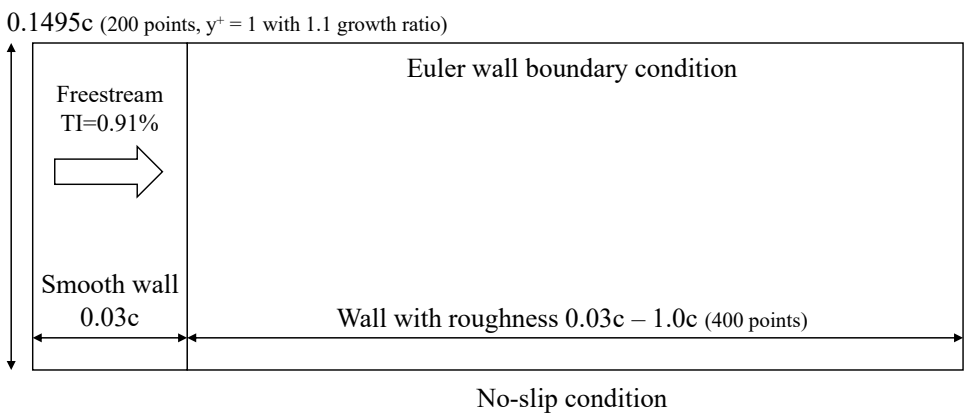

Fig. 26. Zero-gradient flat plate case (Re_x = 1,300,000) [43]

The numerical results of the skin friction coefficient (C_f) are shown in Fig. 27. Roughness was set from smooth to a roughness Reynolds number Re_k of 330 to examine the effects of the height of roughness on the transition model. Because the skin friction coefficient tends to increase after the transition in turbulence, the

location where the curve of the skin friction coefficient changes to positive is used as an indicator of the transition onset. The measured locations of the onset of the transition are indicated on the curve of C_f. At a low roughness height with a value of Re_k smaller than 50, a transition in turbulence did not occur; as roughness increased, the location of the transition onset moved upstream. Current results indicate that roughness tends to accelerate transition onset. However, there are some discrepancies in predicting the exact value for the onset of the transition. It is due to the inherent limitations of the experimental values used for validation and the present model. The experimental value poses arbitrariness since it averaged the various transition onsets measured by Feindt et al. Additionally, the current numerical model contains some partially correlated components. Despite the inherent limitation of the flat plate data, the results serve as an appropriate first check for implementing the roughness amplification model.

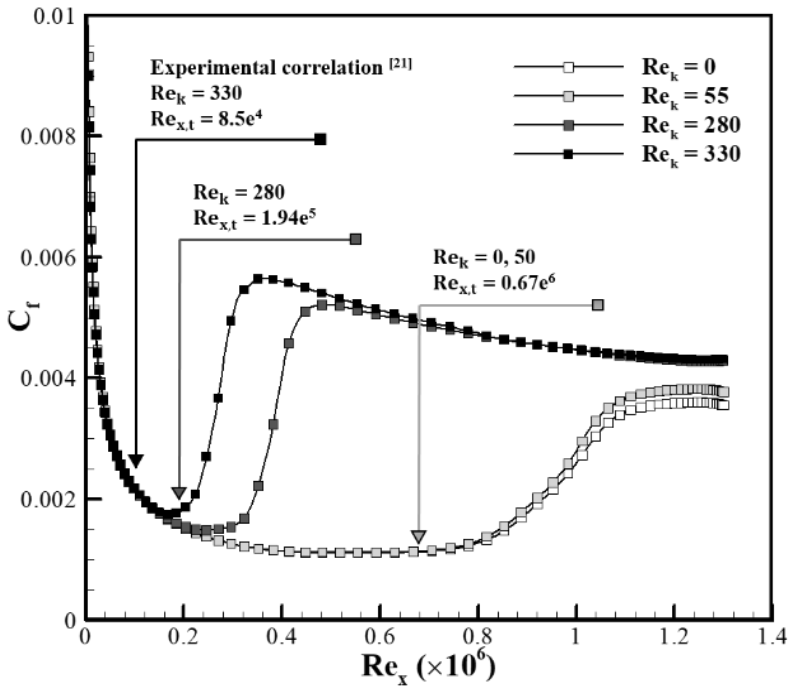

Fig. 27. Coefficients of skin friction for zero-gradient flat plate

6.2.2 Airfoil with roughness of leading edge

The experimental results obtained by Bragg & Kerho [89] were used to assess when the model was applied to an aerodynamic profile. They applied a hemispherical roughness of 0.35 mm to the leading edge of an NACA0012 airfoil with a chord length of 0.5334 m, and observed the effects of the roughness of the leading edge on the development and transition of the boundary layer. The characteristics of roughness were controlled by changing the distance between leading edge and the length of the rough region as summarized in Table 5. For the numerical simulation, an O-type grid was used with 800 points along the surface and 135 in the normal direction. The near-wall grid spacing was $y^+ = 1$.

Table 5. Summary of roughness-related characteristics

Case	k/c ($\times 10^{-6}$)	Re_k (roughness begin)	Re_k (roughness end)	x/c (rough zone)
Clean	0	0	0	0
1/2" @ 8mm	656	701	907	0.00612 – 0.0258
1/2" @ 18mm	656	988	918	0.0212 – 0.0432

Fig. 28 shows a comparison of integrated intermittency ($\hat{\gamma}$) and state of the boundary layer between the experimental and the numerical results. The mean value of γ for the thickness of the boundary layer was calculated through the surface of the airfoil. The state of the boundary layer was categorized into laminar, transitional, and turbulent regions according to the profile of $\hat{\gamma}$. The transition onset was defined

at the location where $\hat{\gamma}$ abruptly increased and reached a constant value of approximately 0.8.

The model did well to track changes in the transition onset due to the increase in the roughness of the leading edge, while relatively early transition was predicted for clean airfoils. The profiles of $\hat{\gamma}$ did not exhibit a large difference of up to x/c = 10%, where ice accretion mostly occurred, and the model was applied to the case of accretion of ice on the airfoil. Another feature of Fig. 28 is that the numerical results repeatedly underpredicted the length of the transitional region. This feature can be explained by absence of the correlation for roughness impact on transitional region, as mentioned in Section II. B. However, this disparity can be considered acceptable in the prediction of ice shape.

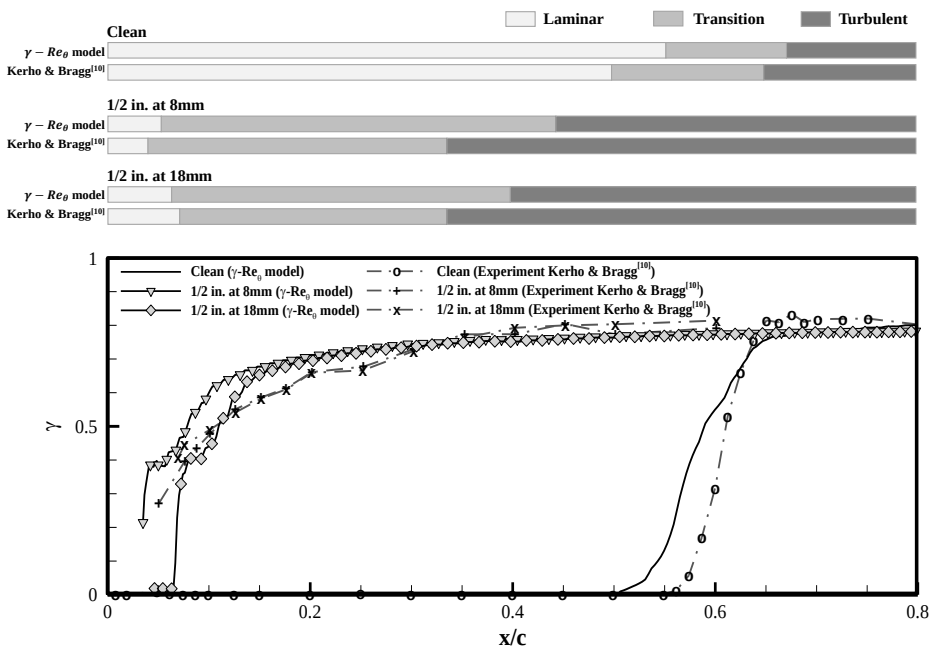

Fig. 28. Integrated intermittency for partially roughened NACA0012 [85]

6.3 Roughness distribution model

6.3.1 Roughness height comparison

The roughness height on the iced surface was obtained through the analytical model for the behavior of water beads on it. To assess the model, the numerical value of the height of roughness was compared with that obtained from experimental data at the AERTS facility [40]. For the numerical simulation, a 2D O-type grid about an NACA 0012 airfoil with an angle of attack of zero was used with 800 points along the surface and 135 in the normal direction. The near-wall grid spacing was $y^+ = 1$. Due to the characteristics of the model of water beads, the evaluation focused on glazed ice as shown in Table 3

Table 6. Validation cases for surface roughness [40]

	Case A	Case B	Case C	Case D
Airfoil	NACA 0012			
Chord (m)	0.5334			
Angle of attack (°)	0			
Airspeed (m/s)	66.7	66.7	66.7	66.7
Temperature (°C)	-3.60	-5.54	-5.86	-9.90
LWC (g/m^3)	1.7	1.7	1.0	0.6
MVD (µm)	30	30	20	30
Time (s)	94	94	94	94

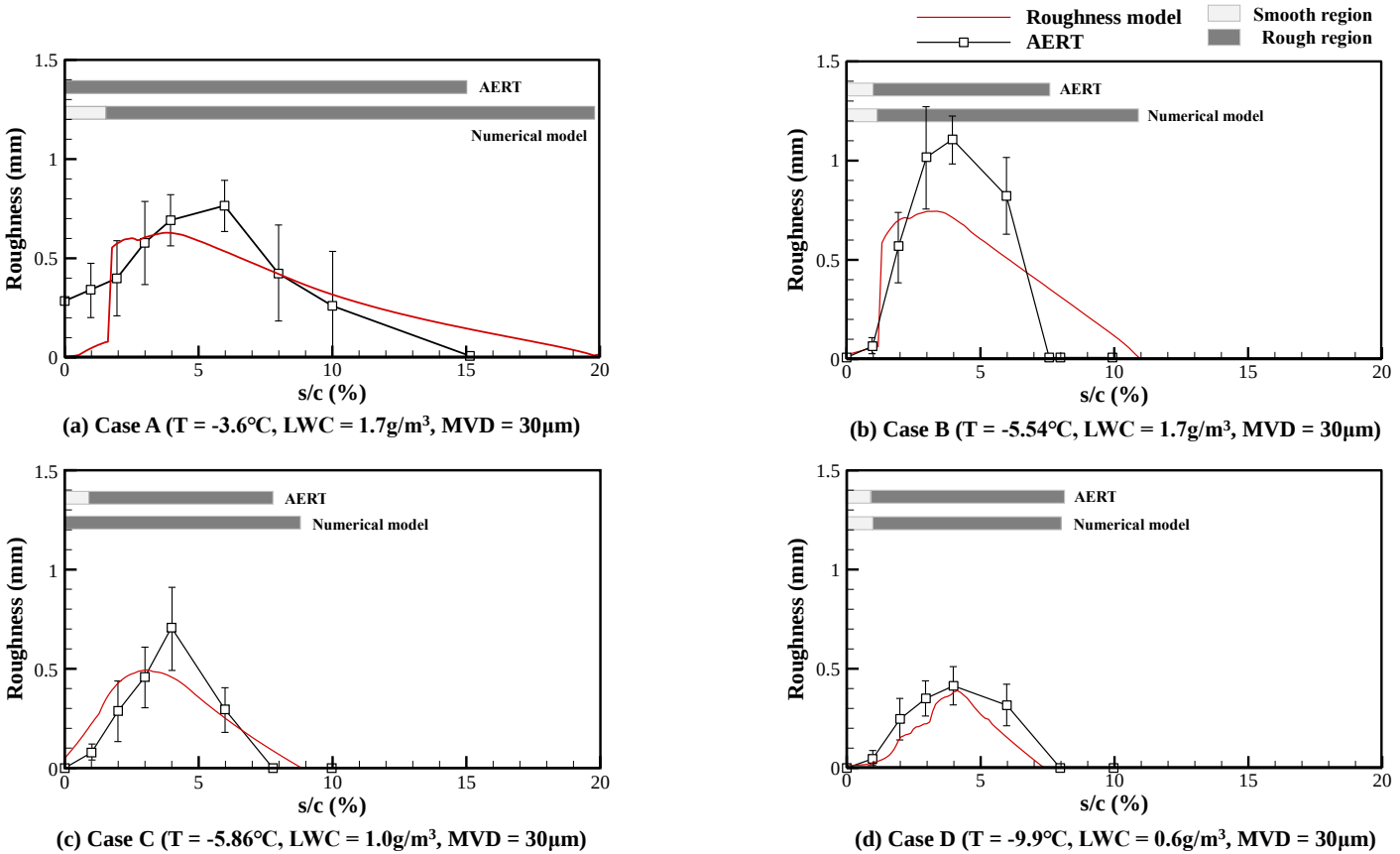

Fig. 29. Comparison of heights of surface roughness [40]

The numerical results are shown by the red solid line and the experimental measurements by the black solid line with square symbols in Fig. 29. s / c = 0% was the stagnation line. The bar graph shows the smooth and rough zones. The location for smooth to rough zone is presented in Table. 7.

Table 7. Rough-smooth zone transition location and ice/impinging limit

	Case #	Case A	Case B	Case C	Case D
AERTS Results [14]	Smooth to Rough Transition, % s/c	0	1.5	1.6	1.4
	Ice limit, % s/c	15.2	7.6	7.8	8.0
Numerical results	Smooth to Rough Transition, % s/c	1.7	1.4	0.4	1.2
	Ice limit, % s/c	19.6	10.8	8.7	7.6
	Impinging limit, % s/c	8.6	8.6	8.6	6.7

The model formed a smooth zone with a thin film of water from the stagnation point to 1%–2% of the chord owing to the high impingement rate. Outside of the smooth zone, the roughness heights abruptly increased, and a rough zone with rivulets and beads was predicted for both the areas of impingement and wetting. The numerical results were encouraging in that most predicted location of smooth-rough zone showed good agreement with the experimental data, with a slight disparity in the predicted roughness height. The error was assumed to be caused by the

assumption of the model that the semi-spherical beads covered 85% of the rough zone regardless of the density of roughness. The value of 85% is obtained from experiments without ice accretion and water flow until reaches steady state [83]. However, for the icing condition, ice starts to accrete and water film flows in short duration of time. Under this condition, the maximum surface coverage would be lower than the 85%, which would increase the predicted roughness height.

As seen in Fig. 29(a), the experimental result observed the rough zone starting from the stagnation point, while present model predicted the smooth zone near the stagnation point. Standard deviation of experimental results indicated the disturbance for the rivulet flow at the stagnation point, which would contribute the rough zone formation at that region [40]. The numerical result computed water film in this region due to the high impingement rate and no other disturbance was assumed.

Another trend found in Fig. 29 is that the numerical results predicts the longer wetted region than the experimental results. This is thought to be due to the difference between the experiment and numerical assumption. Since AERTS facility controlled the airspeed by rotating system, the water beads on the surface tended to form streaks and rivulets that moved in diagonal direction due to the centrifugal force [40]. On the other hand, in numerical simulation, the water beads are only affected by the aerodynamic force and move linearly toward the trailing edge, resulting in longer wetted regions. Fig. 29(d) displays no difference in icing limit, since the most of the ice is formed near stagnation point due to low LWC and temperature.

Nevertheless, use of such quantitative and phenomenological model enabled the numerical prediction of the local roughness distribution, and suggested that the present approach is quite promising for applying on the airfoil icing simulation.

Chapter 7

Application: Icing on fixed airfoil

7.1 Roughness distribution and laminar-turbulent transition

The primary effect of roughness on ice accretion is an increase in the rate of convective heat transfer. This section compares The convective heat transfer coefficient obtained using the proposed transition model, accompanied with the roughness model, with experimental results from the AERTS facility [40]. For the conditions given in Table 3, the Frossling number (Fr) defined in Eq. (31) is shown in Fig. 30. Fr is a non-dimensional value of the heat transfer coefficient used to eliminate the effect of the Reynolds number on different ambient conditions:

$$Fr = \frac{Nu}{\sqrt{Re}} = \frac{h_{cv}c/\kappa}{\sqrt{U_\infty c/\nu}} \tag{31}$$

h_{cv} = convective heat transfer coefficient, c = chord length,

κ = thermal conductivity, U_∞ = air speed, ν = kinematic viscosity

The red solid line and black dash-dotted line show the numerical results of the roughness-induced transition model and the fully turbulent model, respectively, with the roughness distribution obtained from Fig. 29. The $k-\omega$ SST model was used to analyze the fully turbulent model. The black solid line with square symbols indicates the experimental results of Fr from the AERTS facility [40]. The bars plotted under the Fr curves show the smooth and rough zones while the upper bars

represent the laminar–transition turbulence region. The transition onset and transitional region length are presented in Table. 8.

Table 8. Transition onset and transitional region length

	Case #	Case A	Case B	Case C	Case D
AERTS Results [14]	Transition onset, % s/c	0	1.6	1.9	1.9
	Transition length, % s/c	5.9	2.3	3.5	3.8
Numerical results	Transition onset, % s/c	1.7	1.6	1.8	1.8
	Transition length, % s/c	1.9	1.6	2.1	2.1

In Fig. 30, the numerical results for two turbulent models show different aspects of predicting The convective heat transfer coefficient. A significant difference in the numerical results occurred in terms of the transition onset in the curve of Fr. The transition onset was estimated as the point where the curve near the stagnation point changed from a negative to a positive gradient. The results of the transition model show the laminar region up to s / c = 2% from the stagnation point, and the transitioned occurred as the value of Fr increased. On the contrary, the results of the $k-\omega\, SST$ model predicted that the entire airfoil would be covered with the turbulent boundary layer, and thus the maximum value of Fr appeared at the stagnation point, which was inconsistent with the experimental results.

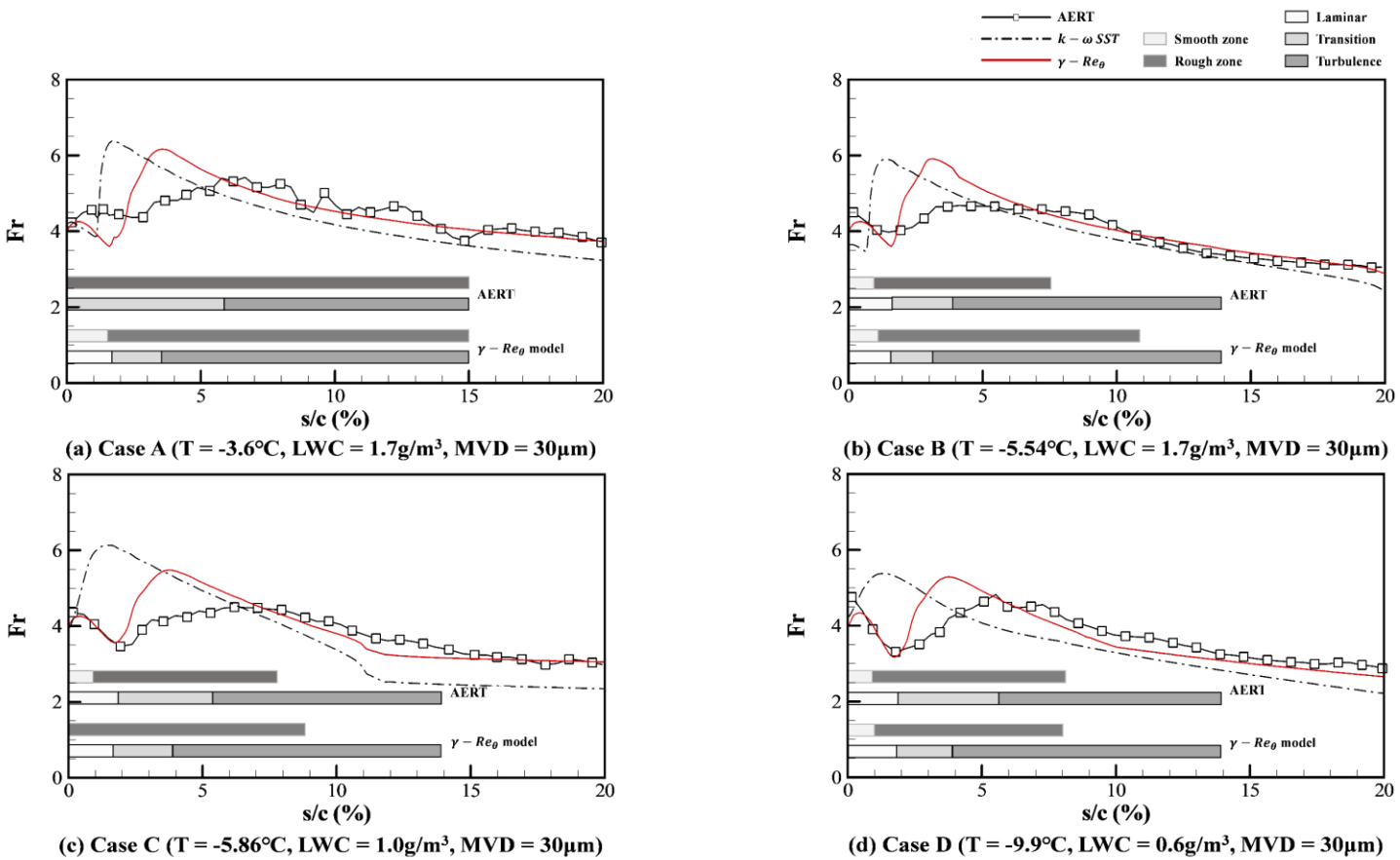

Fig. 30. Comparison of heat transfer coefficients [40]

The presence of the transition onset also affected the prediction of the heat transfer rate near the trailing edge. Applying the transition model yielded a larger value of Fr behind the airfoil. Because the transition model had predicted a higher skin friction coefficient for the turbulent boundary layer to compensate for the deficit in its momentum because the laminar region was near the leading edge, heat transfer coefficient also increased.

Fr curves predicted by the roughness-induced transition model showed similar trend with the experimental results in terms of the transition onset. Once the numerical and experimental rough zones had appeared at s/c = 1% as shown in Fig, 8, the results of both presented the transition onset near s/c = 2% with a slight deviation. This implies that the proposed transition model predicted the premature transition owing to local roughness in the iced airfoil. For case A, where the experimentally obtained rough region started from the stagnation point, unstable Fr values appeared from the beginning of the airfoil, where these differed from the numerical results showing a smooth rough zone and laminar region.

A deviation occurred in predicting the length of the transition region, similar to the results in the case of validation compared with the experiment by Bragg & Kerho [89]. This affected the magnitude and location of the maximum rate of heat transfer, which affected Fr as shown in the Fig. 30. Because the proposed model accounts for the effects of roughness only for the transition onset, it can be improved by correlating the interaction between the length of the transition region and local roughness.

7.2 Effect on roughness and transition model on ice shape

The proposed roughness-induced transition model was assessed by comparing its results with 2D shapes of ice obtained in experiments and the fully turbulent model. The local roughness model was applied to the proposed model, and the equivalent roughness model of sand grains was used for the fully turbulent model. The cases of evaluation were from the validation report for LEWICE 2.0 [98].

Table 9. Validation cases for shapes of ice [98]

	Case 1	**Case 2**	**Case 3**	**Case 4**	**Case 5**	**Case 6**
Airfoil	NACA0012					GLC305
Chord (m)	0.5334				0.9144	0.9144
AoA (°)	4				3	4.5
V_∞ (m/s)	102.8	102.8	102.8	102.8	67	90
T_∞ (°C)	-11.11	-11.11	-9.87	-22.78	-7.16	-4.86
LWC (g/m^3)	0.55	1.0	1.3	1.0	1.0	0.54
MVD (μm)	20	20	30	20	24.8	20
Time (s)	420	231	480	420	1200	1350
IRT case#	403	308	072591.002	425	C17	72503

The cases considered focused on the laminar and mixed ice conditions with upper and lower horns, as shifts in the maximum convective heat transfer due to the application of the transition model affect the predicted ice horn. Case 4 refers the rime ice case. Cases 5 and 6 show the shapes of ice at 22.5 minutes, the maximum exit time without an icing protection system stated in AC20-73A [57]. The numerical simulations were performed for a 2D O-type grid with a near-wall spacing of $y^+ = 1$. The shapes of ice were obtained by the multi-shot method, and the time step used for each shot was determined according to the equation given in the user manual of LEWICE 2.0 [98].

In Fig. 31, the solid red line indicates the results of the roughness-induced transition model while the dashed line represents those of the fully turbulent model, $k - \omega\ SST$ model, and the square symbol shows the results of the experiments. The differences in the shapes of ice obtained using the proposed model are shown by the cases of mixed ice in Figs. 31(a)–(c). The geometry of ice differed in two respects: (1) relatively low ice accretion near the stagnation point, and (2) height of the ice horn on the lower surface of the airfoil. Fig. 31(d) presents the shapes of ice in the low-temperature case, where rime ice was dominant, and no specific difference in shape was observed. Fig. 31(e) and (f) show results of the mixed and glaze ice cases exposed for long periods. Similar trends were observed as shown in Figs 30(a)–(c).

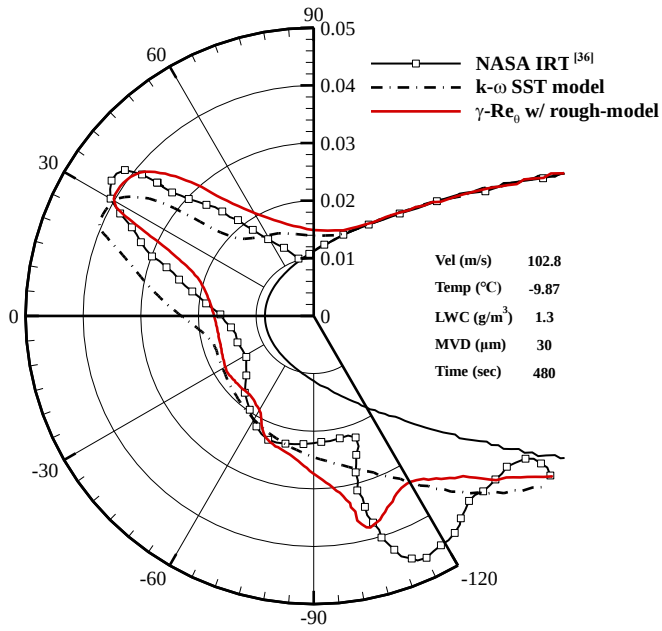

(a) Case 1

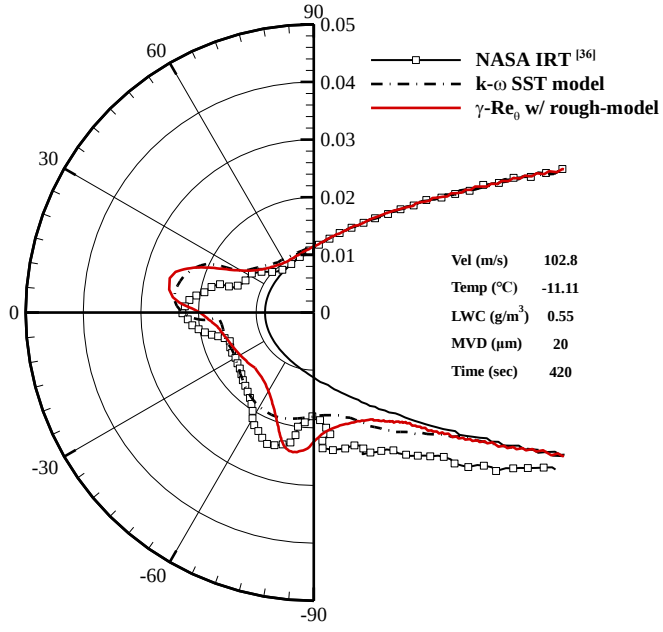

(b) Case 2

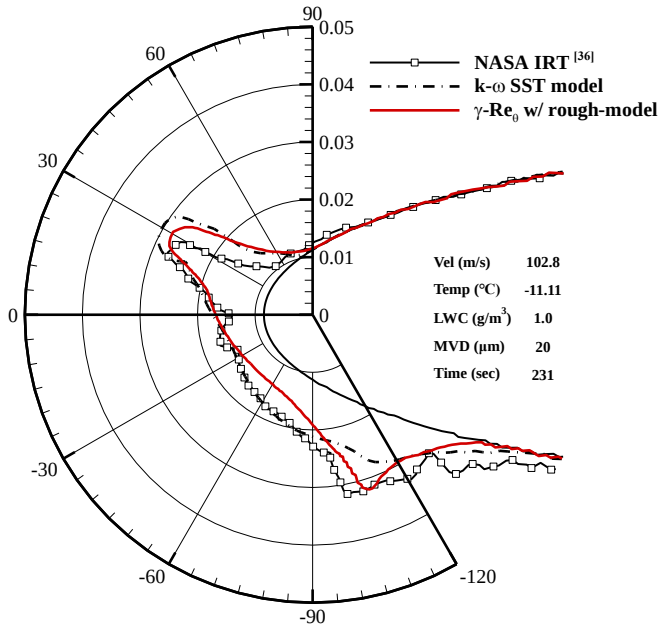

(c) Case 3

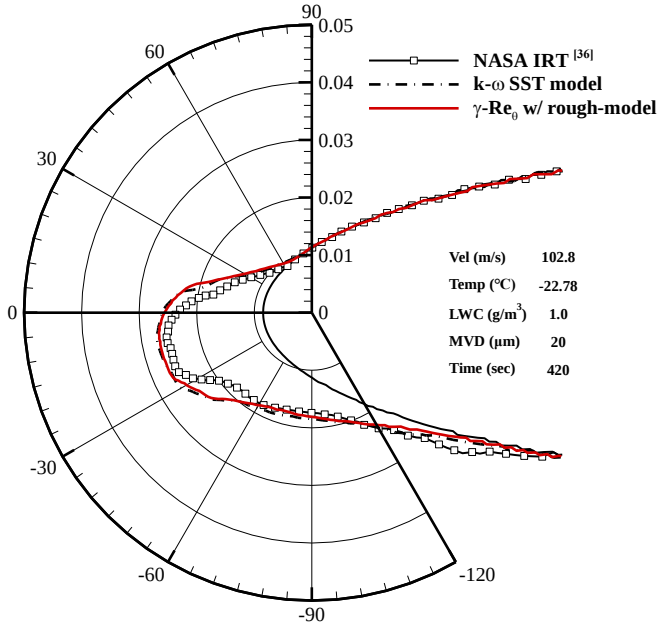

(d) Case 4

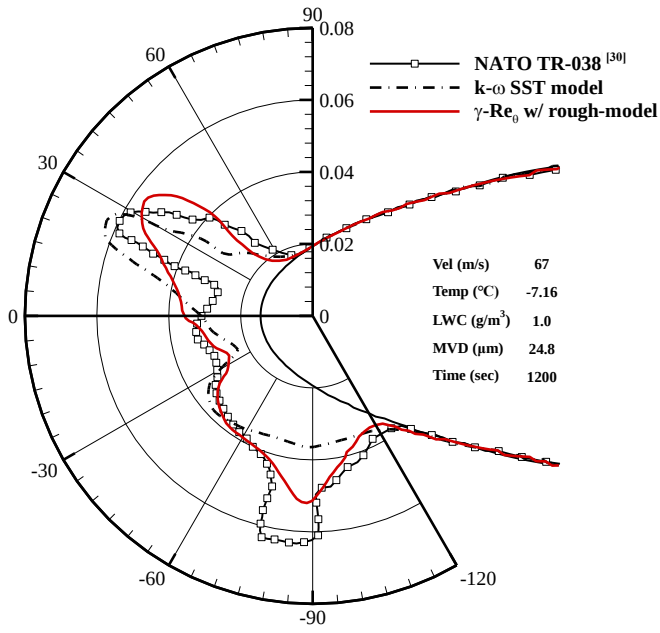

(e) Case 5

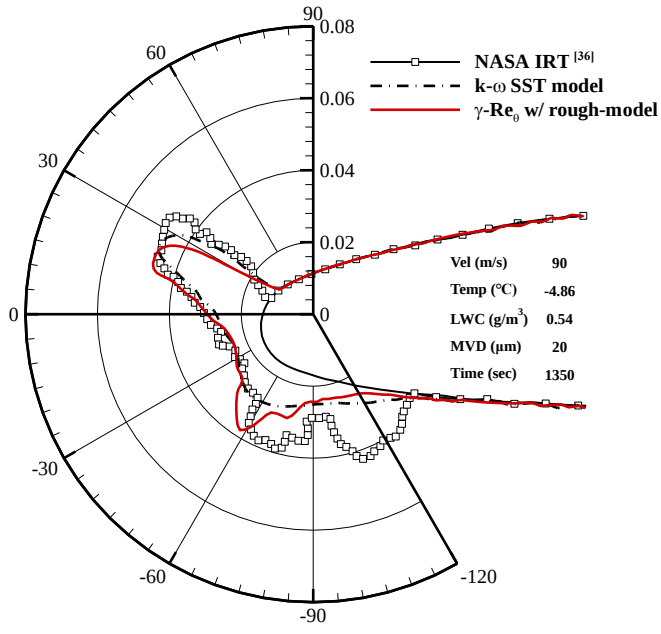

(f) Case 6

Fig. 31. Ice shape compared with the NASA IRT cases [98]

Fig. 32 shows the location and size of the ice horns on the upper and lower surfaces for the case of mixed ice in Figs. 30(a)–(c) for a quantitative comparison once roughness-induced transition was considered. The position of the ice horn was expressed as the angle between the center of the airfoil and the curvature of the leading edge, and height was represented by the perpendicular distance to the clean surface. A significant difference was observed for the ice horn of the lower surface, as shown in the left bar charts of Figs. 31(a)–(c). When roughness-induced transition was considered, thin ice was predicted near the stagnation point but an intruded ice horn instead formed on the lower surface. Compared with the results of the full turbulence model, the height of the ice horn increased by 30%–75%. Although the bar chart shows the thickest point in the full turbulence model, the ice horn is difficult to distinguish from the radial shape of ice in Figs. 31(a)–(c).

According to the turbulent models, the difference in ice shape is occurred due to different thermal convection characteristics of laminar and turbulent boundary layers. Assuming a turbulent boundary layer from the stagnation point, a fully turbulent model exhibits relatively high thermal convection characteristics. As a result, a relatively flat convective heat transfer coefficient distribution appears on the lower surface, and the ice thickness shows a slight difference. Alternatively, the transition model shows low thermal convection near the stagnation point since it considers the laminar boundary layer region but quickly increases after the transition onset. Therefore, the transition model simulates the ice horn by allowing less frozen water

film near the stagnation point with the laminar boundary layer to flow backward and freeze more near the transition onset.

The above-mentioned difference was considered to be the result of the redistribution of the convective heat transfer coefficient due to transition-related considerations. The proposed model showed the laminar region near the stagnation point that led to the low convective heat transfer. For glazed and mixed ice, rate of accretion followed the rate of convective heat transfer and, therefore, less ice accumulated in these cases compared with the results obtained with the assumption of full turbulence. Low ice accretion near the stagnation region increased the rate of flow of the film of water along the surface. With an abrupt increase in convective heat transfer after the transition onset, the mass of flowing water froze to form the ice horn.

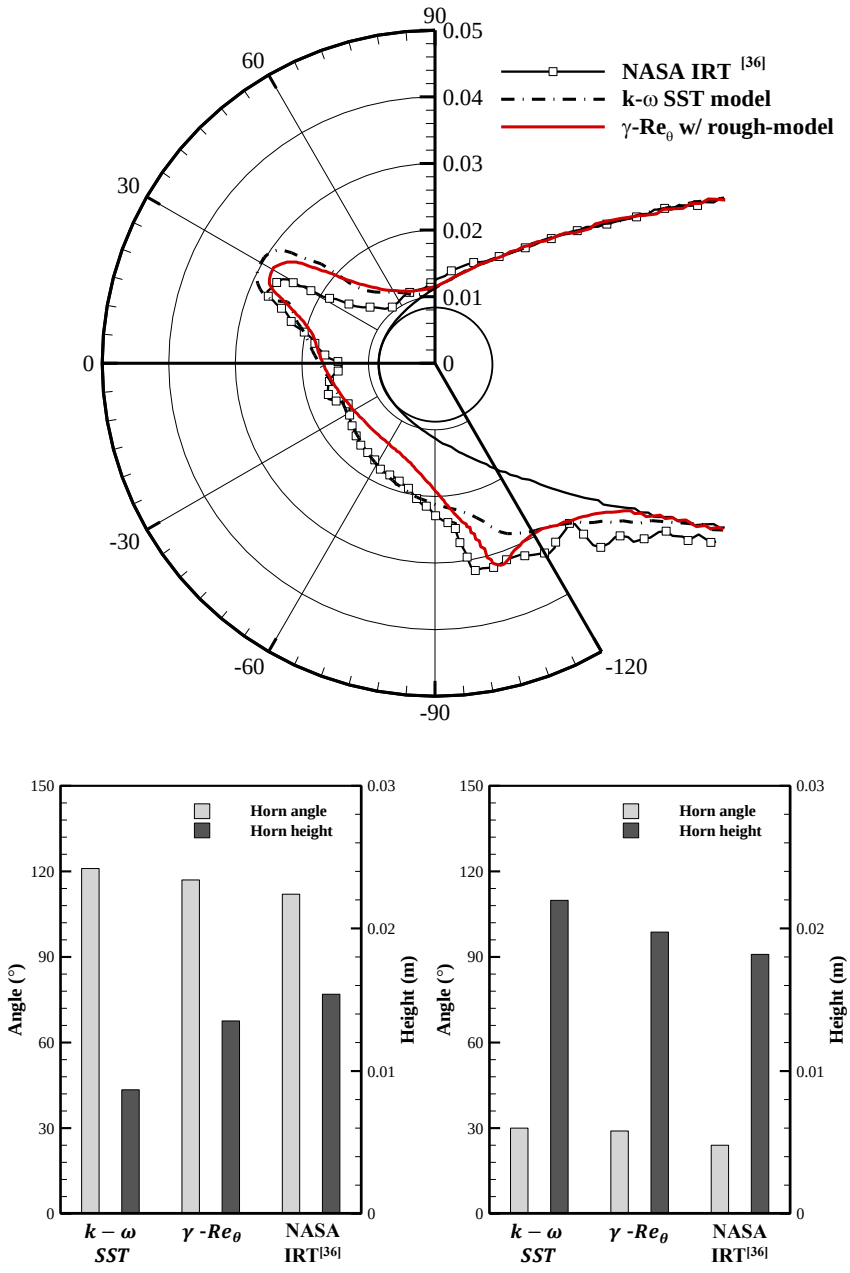

(a) Case 1 –Radial ice shape and lower(left) and upper(right) horn shape comparison

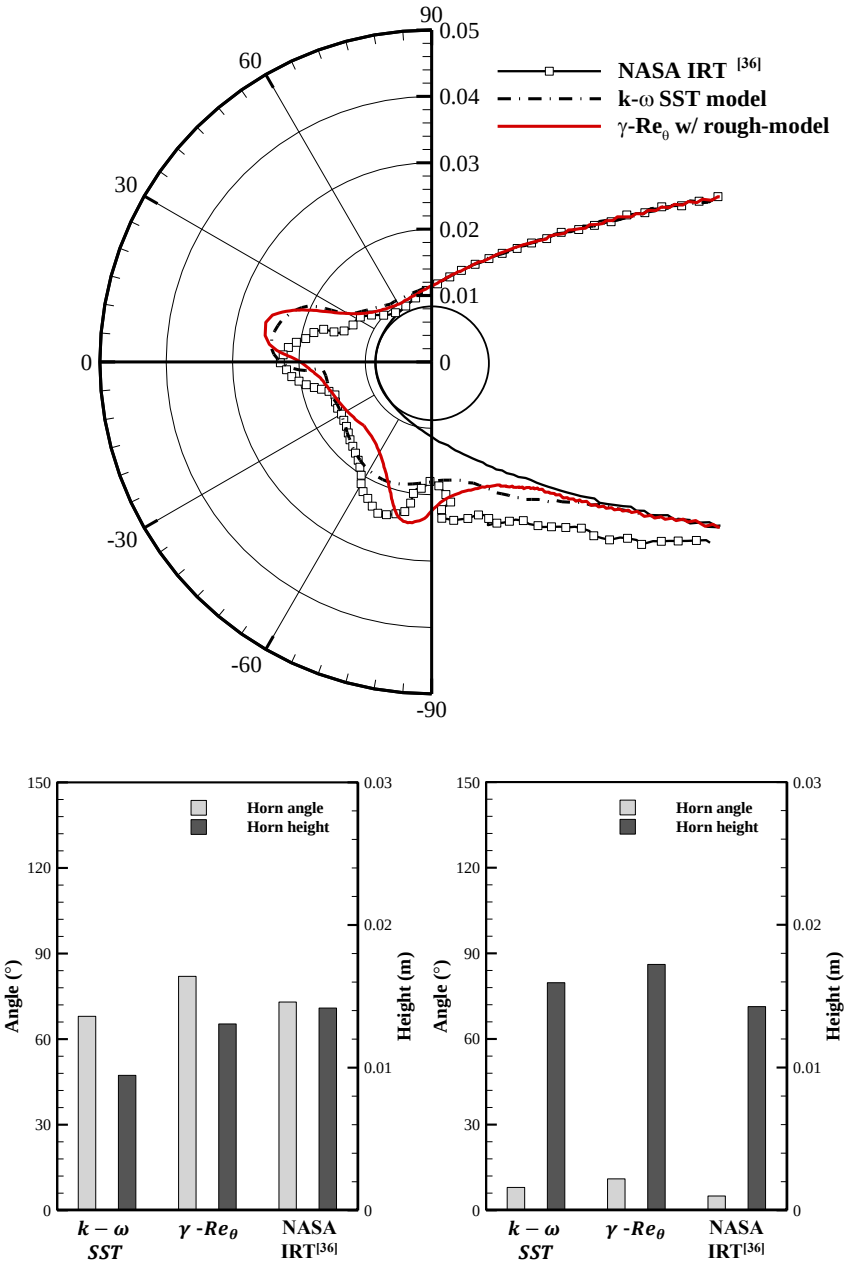

(b) Case 2 –Radial ice shape and lower(left) and upper(right) horn shape comparison

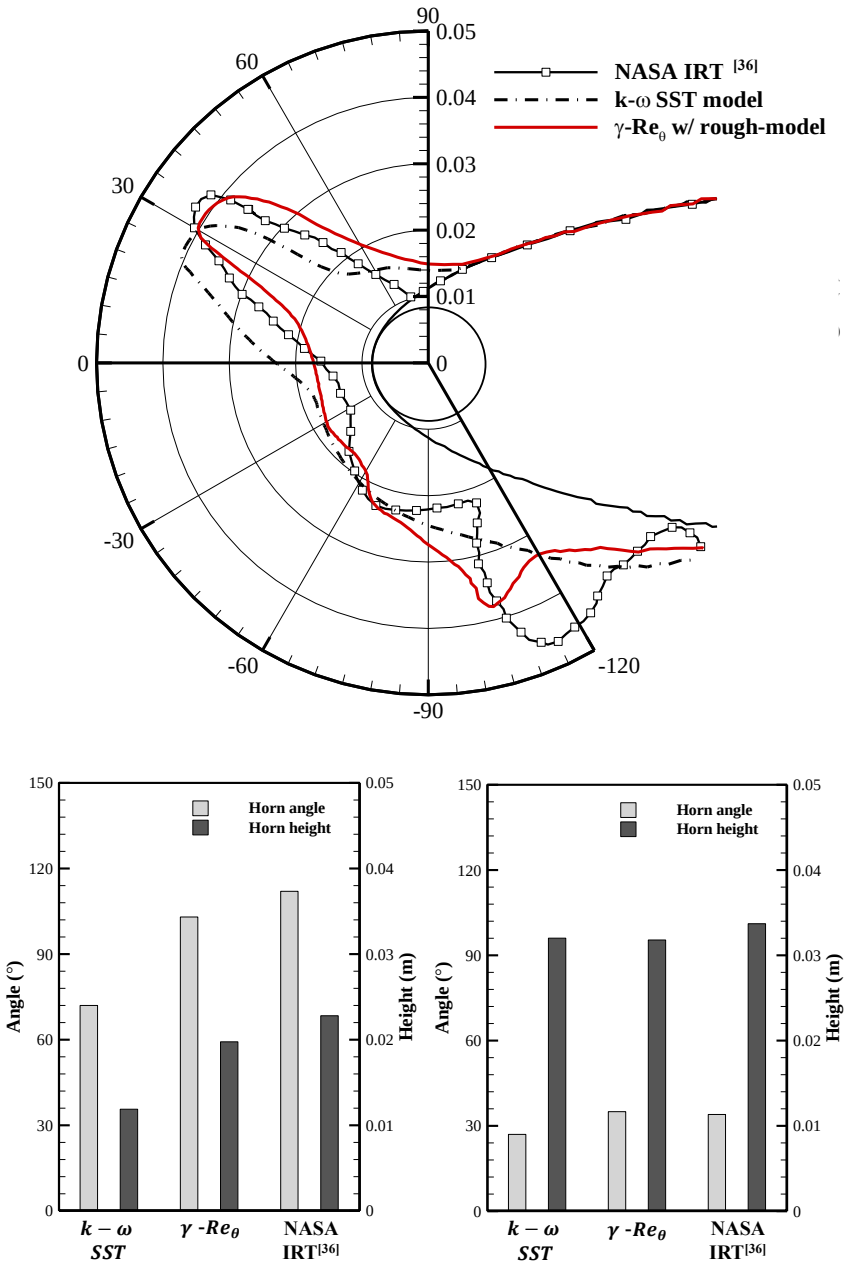

(c) Case 3 –Radial ice shape and lower(left) and upper(right) horn shape comparison

Fig. 32. Shape analysis for cases of mixed ice

The redistribution of the thickness of ice and the subsequent ice horn were mainly observed on the lower part of the suction side of the airfoil, whereas the upper side or pressure side did not exhibit a large difference, as shown in the right section of Figs. 31(a)–(c). The high-pressure gradient on the upper surface due to the angle of attack caused convective heat transfer to increase rapidly over a short length after stagnation. Therefore, in this region, the point where the convective heat transfer peaked due to the transition after the laminar region and that of the fully turbulent assumption were similar.

To show the above tendency clearly, the convective heat transfer in the case where only roughness was applied to the clean airfoil shape was calculated as shown in Fig. 33. The red solid line represents the $\gamma - Re_\theta$ model, which predicted a delayed position for the maximum convective heat transfer coefficient for both the lower and the upper sides of the airfoil compared with the results of the $k - \omega\, SST$, represented by the black dashed line. Although the transition onset appeared for both sides of the airfoil, unlike the lower surface where the size and position of the maximum h_{cv} changed, only the position was slightly tilted on the upper surface.

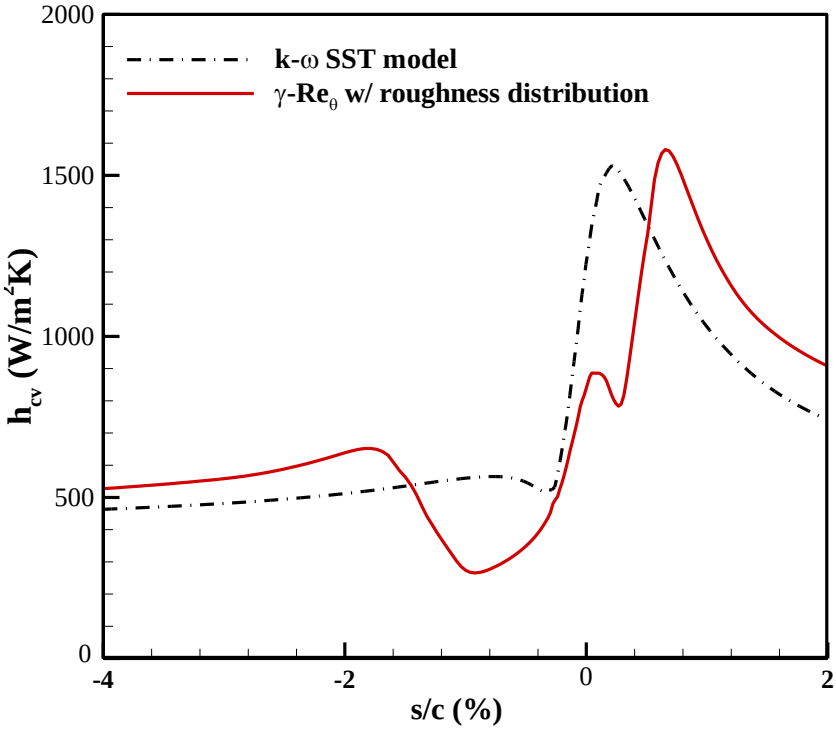

Fig. 33. h_{cv} for case 1 (V_∞ = 102.8 m/s, T_∞ = -11.11 ℃, LWC = 0.55 g/m^3, MVD = 20 μm)

In summary, the present research applied the roughness-induced transition model to the RANS-based inflight icing code, and numerically evaluate its influence on airfoil ice shape prediction. To simulate roughness effect on the transition, the A_r transport equation was linked with the $\gamma - Re_\theta$ model instead of the fully turbulent model. Since the local roughness affects the roughness-induced transition model, local roughness distribution was computed based on the physical insights.

Compared to the result of fully turbulent $k - w\ SST$ model, the present roughness-induced transition model has shown improved result in predicting

convective heat transfer coefficients and ice shapes for airfoil icing cases in glaze ice condition with low Reynolds number. In terms of convective heat transfer, the present method displayed the varying laminar region and transition onset due to the local roughness height variation, unlike the previously used fully turbulent model predicted little or very short laminar regions. This would relieve under-estimation or mis-distribution of the ice mass along the surface. For the lower side of the airfoil, the prediction of ice horn thickness was improved when the present method is applied. At this region, effect of modified h_{cv} due to the transition was well presented due to the low pressure gradient formed by the angle of attack. Therefore, for the second-generation inflight icing code, the current model could attribute to the improved results over the fully turbulent model when applied for the part with low aerodynamic pressure gradient effect in glaze or mixed ice condition. However, some considerations still remain. The model does not consider the influence of the roughness on transitional region length. Better results can be obtained if the proposed model is revised based on the icing experimental results.

Chapter 8

Application: Icing on oscillating airfoil

The present study analyzed the experiments conducted by the Boeing-NASA consortium in detail [21]. The experiment was designed to simulate the pitching motion of the rotor blade in a simplified 2D oscillating motion and present its effect on ice accretion. The SC2110 airfoil with a 15-inch (0.381 m) length was installed vertically on the tunnel floor up to the ceiling for the test to reduce the 3D effect by minimizing the gap between the model and wall. Different combinations of oscillating frequency, mean angle of attack, airspeed, and LWC were tested, as shown in Table 10.

Table 10. Parameters for the experiments of Boeing-NASA consortium [21]

	Run 36	**Run 61**	**Run 50**	**Run 55**	**Run 57**
AoA (°)	5±6	5±6	5±6	10±6	5
V_∞ (m/s)	77.167	77.167	132.727	132.727	132.727
Frequency (Hz)			2.8		
Reduced frequency	0.043	0.043	0.025	0.025	0
Temperature T_∞ (°C)			-14		
LWC (g/m^3)	0.5	1.0	0.5	0.5	0.5
MVD (μm)			22		
Time (s)			600		

To simulate the experiments, a hybrid mesh system was adopted for the computational domain. The mesh system consisted of a boundary layer and freestream regions. For the boundary layer region, a quadrilateral mesh starting with a near-wall grid spacing of y+=1 and growth ratio of 1.1 was used. In contrast, a triangular mesh was used for the freestream region. The inlet, upper, and lower boundaries were detached from the quarter-chord of the airfoil by approximately 10 chords, and the outlet boundary was 20 chords away from the quarter-chord of the airfoil. The surface of the baseline airfoil used 600 grids with 120,000 meshes for the entire domain, and after the shape deformation, approximately 20–30 grids were added to the surface for each step to maintain the grid spacing. For parametric study and ice shape comparison, quasi-steady and quasi-unsteady ice accretion solvers were used. Table 11 shows how each solver applies a different time step. For airflow, droplet trajectory, and thermodynamics analysis, the quasi-steady solver applies local time stepping, and for quasi-unsteady solvers, 2nd order Euler schemes are used that satisfy CFL=5. Eq. (9) in section 3.2.2 was used to determine the time it takes to update the ice shape.

Table 11. Time step selection for icing simulation for oscillating airfoil

	Airflow	**Droplet trajectory**	**Thermo-dynamics**	**Ice shape update**
Quasi-steady	local time stepping (pseudo time step)			Run 36,61 (50 sec)
Quasi-unsteady	2^{nd} order Euler scheme for PIMPLE algorithm (CFL = 5)			Run 50,55,57 (45 sec)

8.1 Effect of oscillating frequency on icing solvers

The key consideration in the icing solver module for oscillating airfoils is how to account for motion-dependent unsteadiness. The quasi-steady ice accretion solver was developed based on the observation that some cases showed no significant difference in shape between oscillating and quasi-static results. The oscillating motion is assumed to be a very slow-moving blade, representing a series of quasi-static events. Fouladi noted that the quasi-steady ice accretion solver depends on the angle of attack and the number of shots. In contrast, the quasi-unsteady ice accretion solver preserves the unsteady characteristics of the droplet and thermodynamic solver. The study focused on the unsteady effect on collection efficiency and glaze ice shape. However, as the icing codes consist of various modules, the governing equations of each module account for different fields that would be affected by the oscillating motion of the airfoil. Therefore, this section discusses the influence of the unsteady effect on each module of the icing solver using numerical results. This study conducted comparative analyses using the quasi-unsteady ice accretion solver and the quasi-steady ice accretion solver that applied the very slow motion assumption described in Chapter 3, section 3.2. In the parametric study, the quasi-unsteady ice accretion solver applied oscillating frequencies of 1.4, 2.8, and 5.6 Hz, while the quasi-steady ice accretion solver applied steady-state calculations for every angle of attack.

8.1.1 Convective heat transfer

To investigate the unsteady effect on the aerodynamic module in the ice simulation, Fig. 34 compares the convective heat transfer coefficients according to the oscillating frequency for Run 50 and Run 61. The red line indicates the result of the steady-state solver, and the square, circle, and diamond shapes refer to the 1.4, 2.8, and 5.6 Hz, respectively

When the quasi-unsteady approach was applied, the transition onsets where the convective heat transfer coefficient changes to a positive curve occurred later from the leading edge than in the corresponding static cases. As the oscillating frequency increases, the transition onset moves downstream in the direction in which the airfoil moves. The transition onset changes significantly during the upstroke and downstroke. At the mid-angle of attack, a delayed transition onset occurred during the upstroke, while a promoted transition onset occurred during the downstroke. Unlike the static case, the present method considered the inertial effect owing to the velocity of the moving wall, which delays separation. Therefore, the response of the thermal boundary layer was extended at the suction side of the upstroke and the pressure side of the downstroke. Fig. 35 represents the γ (intermittency) to visualize the transition onset where γ starts to increase.

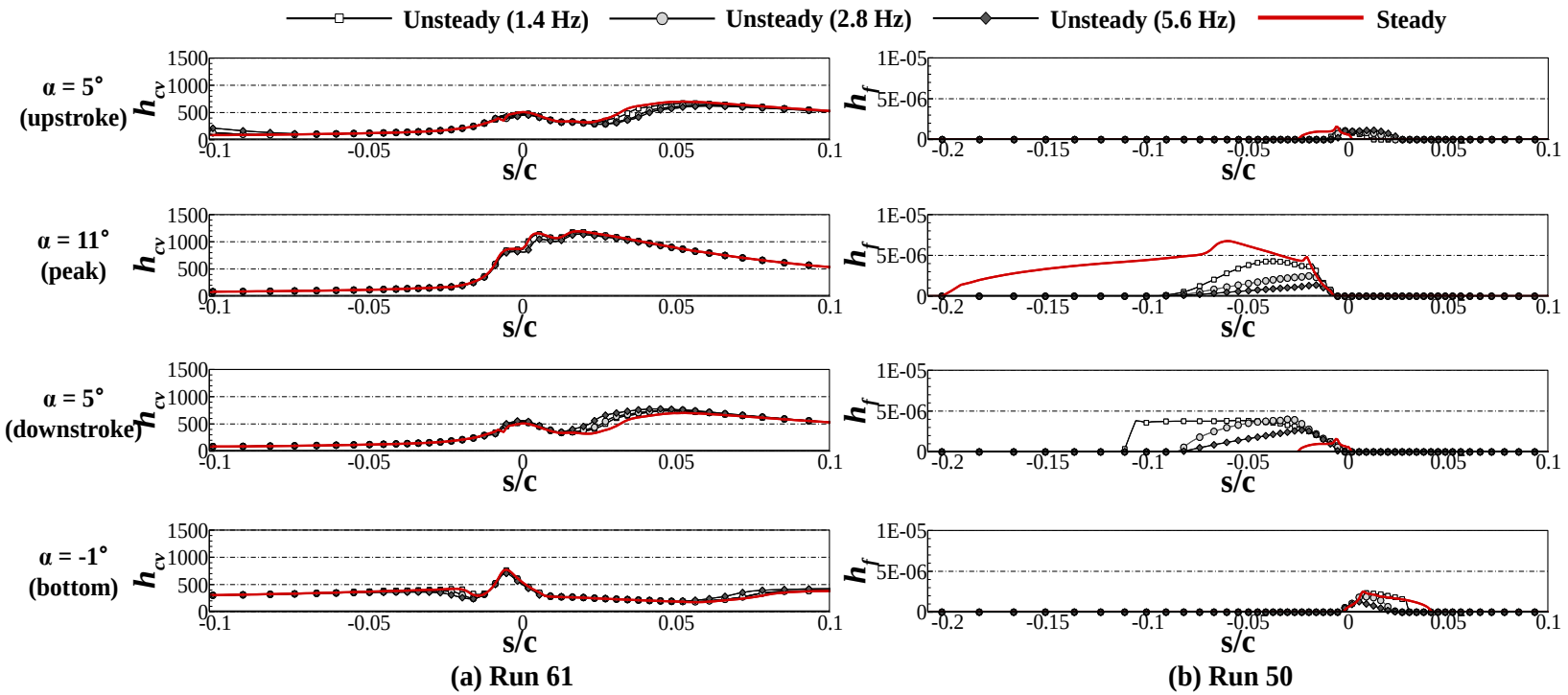

Fig. 34. Convective heat transfer coefficient for different oscillating frequencies and steady state assumption

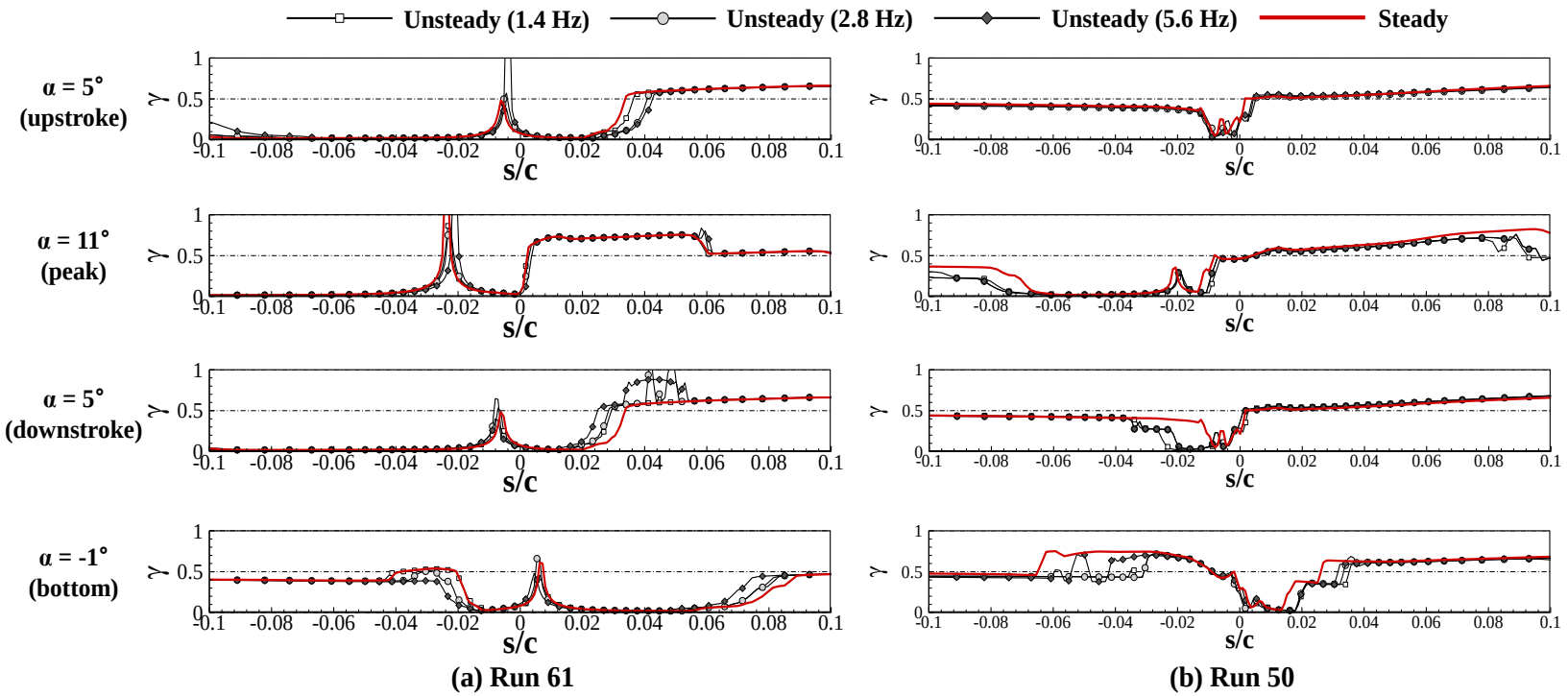

Fig. 35. γ (intermittency) distribution for different oscillating frequencies and steady state assumption

Table 11 compares the non-dimensionalized surface distance from the leading edge to the transition onset of the upper surface at the mid-angle of attack of upstroke and downstroke. The deviation of the transition onset from the steady state solver depends on oscillating frequency and airspeed. The case with reduced frequency over 0.025 showed a 30% deviation compared to the static cases. Thus, the reduced frequency affects the transition onset and the resulting thermal transfer distribution more sensitively compared to the flow field, where the unsteady effect is assumed to be dominant at the reduced frequency over 0.05.

Table 12. Distance of transition onset from leading edge at upper surface

Frequency (Reduced frequency)	**Steady**	**1.4 Hz (0.022)**	**2.8 Hz (0.044)**	**5.6 Hz (0.088)**
		Run 61		
α = 5° (Up)	0.019	0.02	0.025	0.027
α = 5° (Down)	0.019	0.017	0.013	0.012
		Run 50		
α = 5° (Up)	0.007	0.008	0.009	0.009
α = 5° (Down)	0.007	0.006	0.005	0.005

8.1.2 Collection efficiency

Fig. 36 presents an unsteady effect on the impingement module by comparing the collection efficiency according to the oscillating frequency for Run 50 and Run 61. For the sinusoidal angles of 0°, 90°, 180°, and 270° during one oscillation cycle, the results of the steady-state solver and unsteady solvers with different frequencies are depicted in the same manner shown in Fig. 34. At each angle of attack, the impinging area shifted in the direction of airfoil movement according to the oscillating frequency. Accordingly, in the upstroke process, the impinging limit obtained using the quasi-unsteady approach appeared farther from the leading edge than that obtained using the quasi-steady approach. This trend is reversed on the downstroke. Table 12 represents the distance from the leading edge to the impinging limit of the upper surface. The difference in the impinging limit is about 1-5% for the impinging area; therefore, it is not estimated to have a decisive influence on the ice shape.

Table 13. Distance of impinging limit from leading edge at upper surface

Frequency (Reduced frequency)	Steady	1.4 Hz (0.022)	2.8 Hz (0.044)	5.6 Hz (0.088)
Run 61				
α = 5° (Up)	0.019	0.02	0.025	0.027
α = 5° (Down)	0.019	0.017	0.013	0.012
Run 50				
α = 5° (Up)	0.007	0.008	0.009	0.009
α = 5° (Down)	0.007	0.006	0.005	0.005

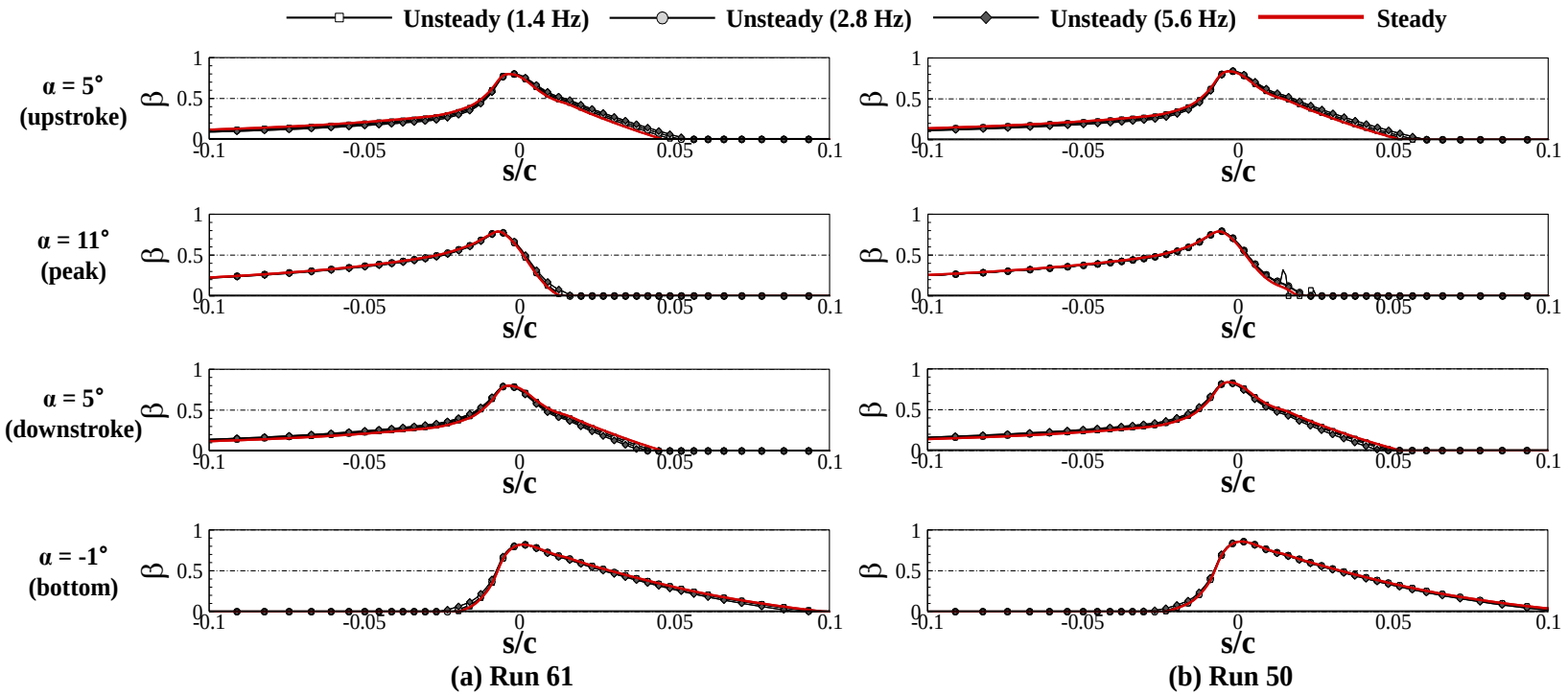

Fig. 36. Collection efficiency for different oscillating frequencies and steady state assumption

8.1.3 Water film thickness

Fig. 37 presents the film thickness at the sinusoidal angles of 0°, 90°, 180°, and 270° during one oscillation cycle. For the comparison, the periodic solution of the quasi-unsteady approach and the converged solution of the quasi-steady approach were used.

The profile of the water film differentiates according to the methodology. For the steady-state solution, the water film accumulated near the stagnation point of each angle of attack. On the other hand, in the periodic solution, the water film moves in the direction in which the airfoil oscillates. Oscillating frequency also affects the profile. The water thickness decreases according to the frequency increment, and the rime ice zone where only ice exists increases. The collection efficiency and flow rate determine the ice profile at the rime ice region, while the mixed zone follows the convective heat transfer curve. Therefore, the results inferred that the water film thickness is dominantly affected by unsteady effects for all oscillating frequencies.

In summary, the oscillating frequency affects the range of collection efficiency and transition onset of the convective heat transfer coefficient. The deviation increases along the frequency near the leading edge. As the ice accretion mainly occurs at the leading edge, a difference of around 5-10% would impact the ice shape. Oscillating motion highly affects the water film thickness, which decides the ice type. Due to the low order of film thickness and velocity, it is more sensitive to the degree of unsteadiness, so it is necessary to apply the unsteady solver even at low reduced frequencies.

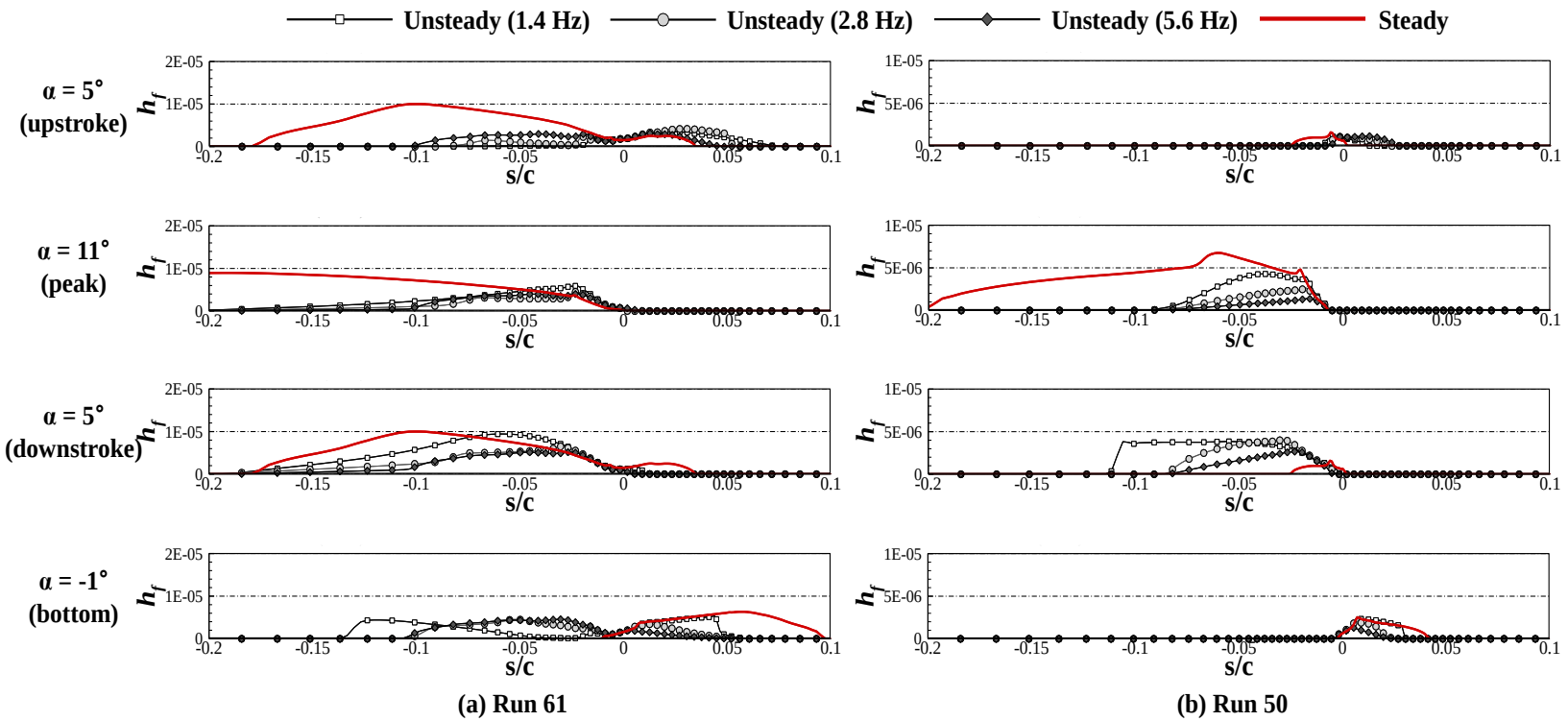

Fig. 37. Water film thickness for different oscillating frequencies and steady state assumption

8.2 Effect of roughness on oscillating airfoil icing

In the in-flight icing simulation, the convective heat transfer increased according to the roughness height and was altered when the laminar-turbulence transition was considered. Therefore, the accuracy of predicting the ice shape varied depending on the prediction of the roughness height and the use of the turbulence model. Conventionally, to simulate icing on an oscillating airfoil, a roughness model based on empirical correlation [8] or the beading model [29] was used. The corresponding roughness models were correlated to match the ice shape forming on a static airfoil, or the characteristics of the water bead generated on a static airfoil are ambiguous when calculating the convective heat transfer coefficient and applying it to the oscillating motion. In this section, the effect of the roughness height on the quasi-unsteady icing solver is examined, and an empirical roughness height considering the parameter related to the oscillating motion is proposed to increase the prediction accuracy of the ice shape.

The present study considered the physical characteristics of ice roughness to correct the empirical roughness of oscillating airfoils. Experimental observations showed that impinging droplets and residual water film roughness determine the surface roughness of static airfoils [25,26]. A bead or rivulet of roughness is formed in the glaze zone with residing water, while the feather of roughness is developed in the rime zone where only ice accretion occurs. Due to the characteristics of surface roughness, the static case grows roughness over several seconds as it has fixed collection efficiency and aerodynamic properties. Alternatively, in an oscillating

surface, the icing parameters constantly change according to body motion, thus continuously altering surface characteristics. We inferred that the ice roughness in the rime and glaze zones determined using the accumulated impinging droplets or water film did not grow fully.

Fig. 38 compared predicted ice shape with different roughness height. Fig. 38(a) is Run 61 with a reduced frequency of 0.044 at an LWC = 1 g/m^3, and Fig. 38(b) is Run 50 with a reduced frequency of 0.027 at an LWC =0.55 g/m^3. The dotted line indicates the experimental ice shape and the dashed line indicates the numerical results applied to the empirical roughness model. The solid line indicates ice shape with the roughness size when the direction and size of the ice horn closely match the experimental values. When an empirical roughness model is applied, the ice horns are usually concentrated near the leading edge. Roughness increases convective heat transfer and premature laminar turbulence in ice accretion. The convective heat transfer peaks near the leading edge with a high roughness value; therefore, the ice horn gathers near the leading edge. Low roughness delayed the formation of the ice horn due to the decreased heat transfer rate, which balances the latent heat of icing, thereby allowing the droplets to freeze before moving to the trailing edge. In Run 61, the ice shape was predicted accurately at 20 % of the empirical roughness and 40 % roughness height of Run 55. When the roughness height was reduced, such as in the case of Run 61 with 10 % empirical roughness, the primary horn reduced, whereas the secondary horns increased.case of Run 61 with 10 % empirical roughness, the primary horn reduced, whereas the secondary horns increased.

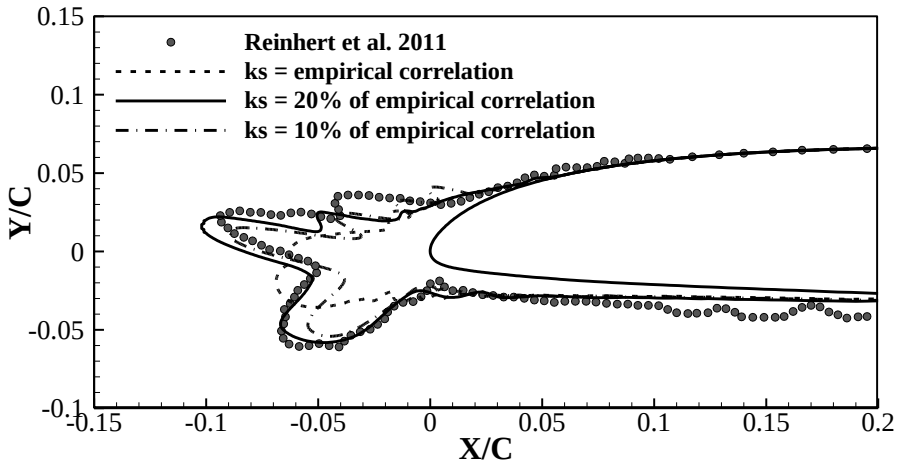

(a) Run 61

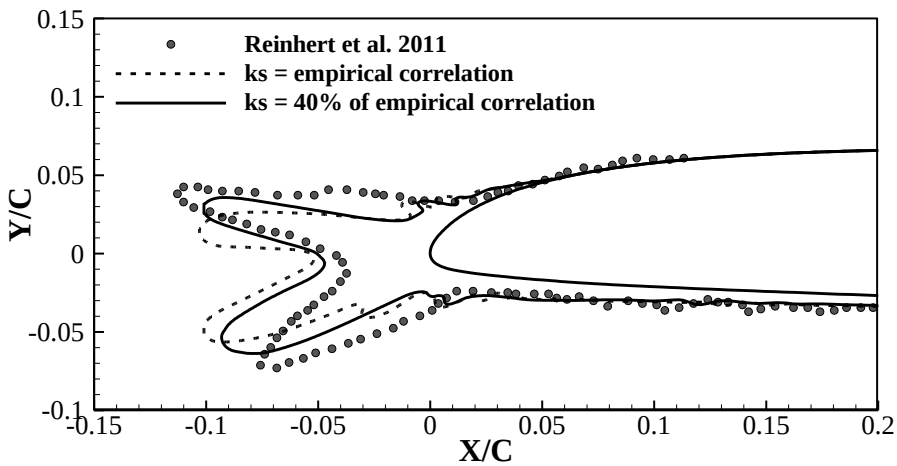

(b) Run 50

Fig. 38. Ice shapes for different roughness heights

The simulated ice shapes in Fig. 38 indicate that as the reduced frequency increases, the roughness height required for predicting the ice shape is reduced. As mentioned in Section IV A., the water film thickness and surface type are affected

by the unsteady effect, and the deviation with the static case grows according to the frequency. Roughness Height is affected by the amount of water on the surface; thus, the study inferred that the degree of unsteadiness affects the roughness height. Fig. 39 presented the ratio for the empirical roughness height according to the reduced frequency and designed the correlation about the reduced frequency. Then present work modified the empirical correlation for roughness, as shown in Eq. (32), by applying the newly designed correlation, in which x_k is the reduced frequency, and α_{corr} is the calibration term for the solver.

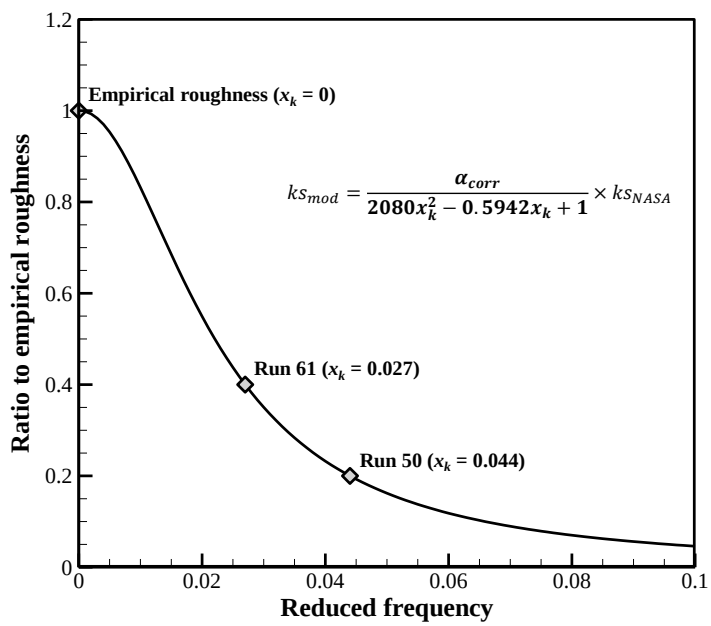

Fig. 39. Ratio for the empirical roughness height according to the reduced frequency

$$ks_{\text{mod}} = \frac{\alpha_{corr}}{2080x_k^2 - 0.5942x_k + 1} \times ks_{\text{NASA}} \tag{32}$$

To sum up, the roughness height involves changes in the thermal transfer rate and transition onset and affects the ice distribution. Since this roughness height is related to the water film strongly influenced by the unsteady effect, it also has an unsteady characteristic. Thus, the empirical term attributed to the reduced frequency was added for empirical roughness correlation from NASA to obtain the roughness value for the icing on the oscillating airfoil. The modified correlation is made based on limited experimental results and requires verification of additional experiments. The improved analysis would be made through a study on a roughness model based on unsteady physics that can account for real-time surface characteristics.

8.3 Ice shape comparison

This section assesses the quasi-unsteady approach applied to ICEPAC. The ice shapes of the oscillating cases presented in Table 10 were compared with the results of the icing wind tunnel test conducted by NASA and numerical analysis results obtained in previous studies. Each calculation was performed in 12 steps according to the equation used to determine the time step used in NASA LEWICE 2.0. The roughness-induced transition model was used as the turbulent model, and the modified empirical correlation presented in previous section was used for the roughness. Each case revealed the characteristics of different ice shapes according to the conditions. Run 36 presented the attributes of rime ice, in general, owing to low airspeed and LWC, and Run 61 showed the characteristics of glaze ice with an ice horn by increasing the LWC. With a high airspeed and low LWC, Run 50 yielded a glaze ice shape. Run 55 had the same ambient conditions as those of Run 50; however, the position of the horn was different because of the high angle of attack. In Fig. 40, the black dots represent the results of the oscillating airfoil experiment performed by Reinhart et al. [21], and the gray squares with solid lines indicate the quasi-steady simulation results obtained by Narducci and Reinhart [22]. For Runs 36 and 61, the numerical results reported by Fouladi [23] are indicated by a dashed line. The solid black lines show the results of the ICEPAC using the quasi-unsteady approach.

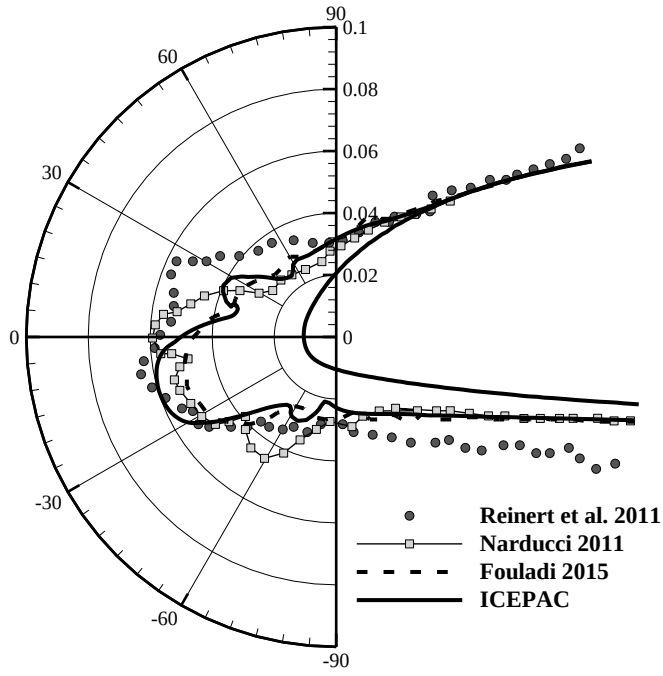

(a) Run 36

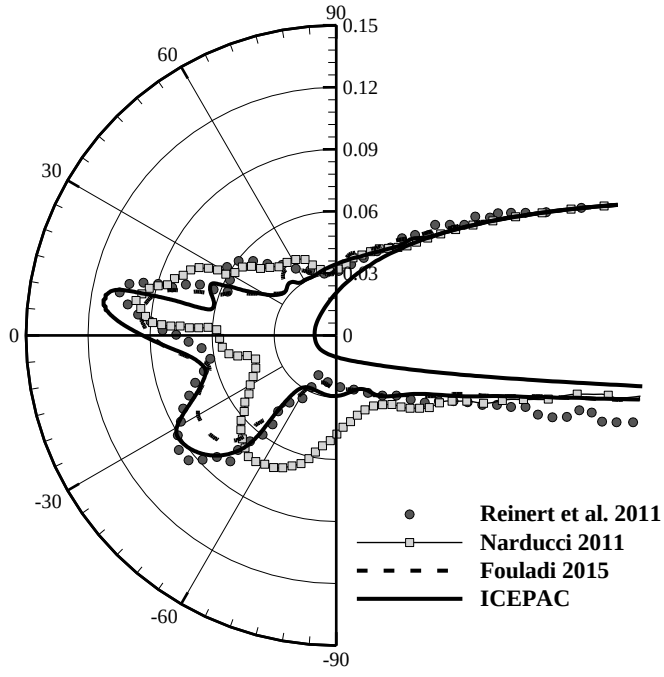

(b) Run 61

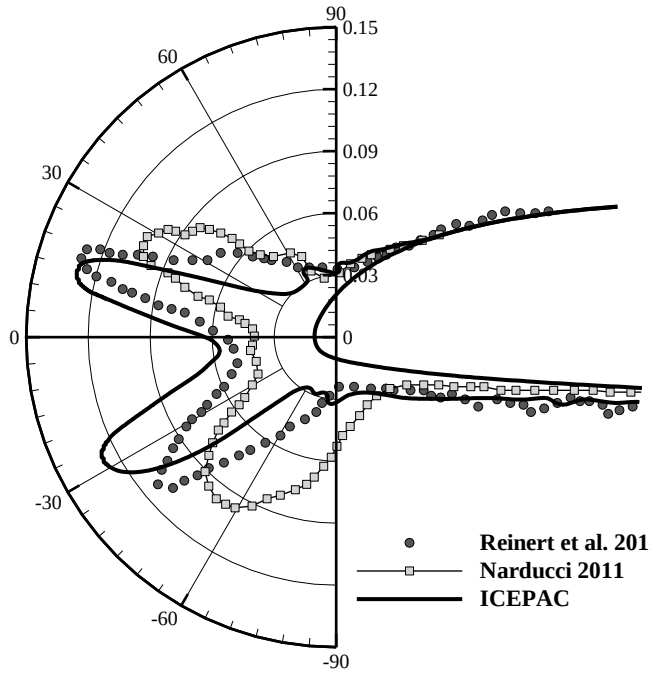

(c) Run 50

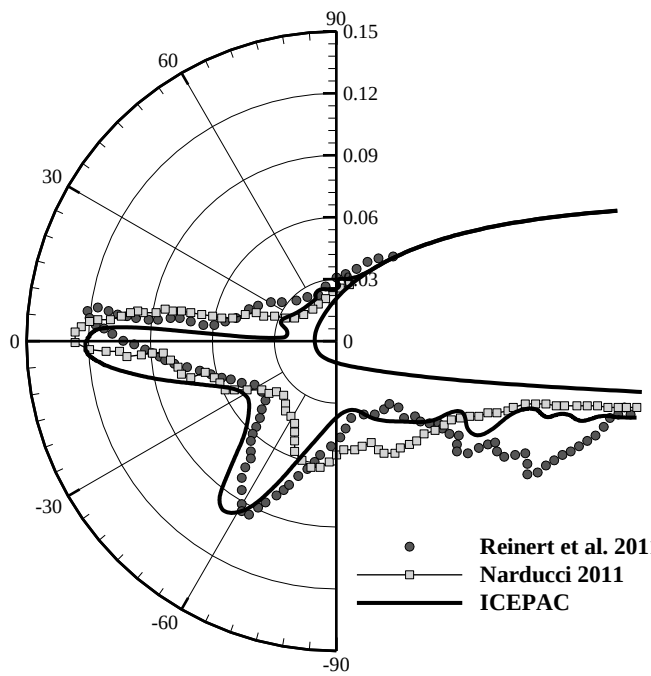

(d) Run 55

Fig. 40. Comparison between the ice shapes on oscillating airfoils

The proposed method accurately predicted the direction and thickness of the ice horn. The geometry of the ice shape was evaluated according to two aspects: the direction of the ice horn and the formation of the secondary horn. For comparison, Fig. 40 applied a radial line graph with a center corresponding to the cylinder of the leading edge curvature of the SC2110 airfoil. The radius of the cylinder was r_{nose}/c = 0.0105. For Run 36, the rime ice case, the numerical results predicted a similar but smaller overall shape than that obtained from the experimental results. The discrepancy in ice size was presumed to be owing to the uniform ice density. Regarding the development of secondary horns on the upper and lower surfaces, the quasi-unsteady approach was closer to the experimental value than the quasi-steady approach. Current methodology considering transitions more clearly displayed secondary horns. This tendency was also observed for Run 61, which formed the glaze ice. The quasi-unsteady approach accurately represented the direction of the ice horn and secondary horn compared to the quasi-steady approach. Runs 50 and 55 showed the results for high airspeed with a low reduced frequency. Owing to the high velocity and low LWC, the water film was concentrated in the formation of the primary horn. In summary, although there were some discrepancies in the ice shape, the corresponding results confirmed that the quasi-unsteady approach sufficiently captured the unsteady characteristics caused by body motion and improved the accuracy of predicting the ice shape on an oscillating airfoil.

Chapter 9

Conclusion and Future Works

Icing poses a severe threat to the operational safety of aircraft. It is essential to determine in advance whether icing will occur and the severity according to weather conditions to prevent accidents caused by inflight icing. Thus, numerical analysis techniques proved to be the most time and cost-effective way of predicting the icing phenomenon among experimental and numerical methods. As inflight icing involves airflow, water droplets, and surface water film, previously developed icing codes assumed quasi-steady conditions. Quasi-steady code integrated with a steady aerodynamic solver and the multi-shot method generates a converged airflow solution only after the shots with an updated ice shape. Although numerical simulation is considered an efficient way to predict the icing phenomenon, some issues arise considering the unsteady characteristics, such as the interaction between body motion and the icing process and surface contamination due to roughness distribution.

This dissertation uses the quasi-unsteady approach to study unsteady characteristics that may occur during inflight icing, which is limitedly considered in previous numerical simulations. First, the interaction between body motion and ice accretion in a moving object was examined through this method. Furthermore, roughness distributions during the icing process were considered in a quasi-unsteady manner, and a roughness-induced turbulent transition model was used to simulate

the effect. The present study demonstrated the validity of the quasi-unsteady assumption by comparing the convective heat transfer coefficient and collection efficiency, which are essential inflight icing parameters. Also, the proposed models better predicted the direction and distribution of the ice horn compared with experimental values of ice shape. Following are the conclusions drawn from the dissertation.

1) The quasi-unsteady approach was first adapted to ICEPAC, developed at Seoul National University so that the ice shape that predicts freezing rates in body motion can only be updated periodically. Body motion was implemented through dynamic meshes, and airflow, droplet trajectory, and thermodynamic modules were sequentially arranged through segregated formulas in time step for airflow. The governing equations incorporated the mesh deformation using the convection terms and boundary conditions. In this study, parameter analysis was carried out using the code to analyze an oscillating airfoil's icing phenomena. Besides previous studies focusing on unsteady collection efficiency, this study showed that unsteadiness affects thermal convection and water film thickness. Additionally, predicted ice shapes demonstrated that icing simulation should consider the effect of unsteadiness by body motion on roughness formation. Based on these results, the study numerically confirmed that the reduced frequency and reduction rate were correlated. The modified roughness is presented by including the reduced frequency function in the static case's empirical model. The quasi-unsteady approach affected the overall

ice shape prediction of the oscillating airfoil. Unlike the results of the quasi-steady approach, the current numerical method has pronounced features, such as the direction and thickness of the primary ice horn and secondary horn formation. The direction and thickness of the ice horn were affected by the redistribution of convective heat transfer and the delayed transition of oscillating motion. Additionally, the modified roughness was crucial for accurately predicting the ice shape. The increased impinging limit and water film coverage also captured the secondary horn considering the unsteadiness of the icing parameter. These ice shape characteristics indicated that accounting for the unsteadiness originating from body motion can improve the icing code applied to moving objects.

2) The roughness distribution model based on the physics of water bead formation was then applied to account for the local roughness distribution growth. Based on the maximum bead height derived through force equilibrium, water beads characteristics were classified according to the residual water in the cells. Then, the model categorized the surface into smooth and rough regions according to the water behavior on the surface. As the proposed methodology requires a thermodynamic module to account for residual water, the existing icing code's sequential connection limited the transfer of the roughness effect from the thermodynamic module to other modules. The current model partially applies the quasi-unsteady method to deliver the roughness effect to the turbulent model. During a single shot, airflow, droplet trajectory, and thermodynamic modules were solved together to converge roughness

and convective heat transfer coefficient. A quantitative comparison was made between the surface roughness height and the heat transfer coefficient derived from the simulation with the empirical correlation. The result was quite encouraging in predicting the width of the smooth-rough region. Since the prediction of the transition onset in the present approach is highly dependent on local roughness, the study on the numerical model capable of distinguishing the smooth-rough region improved the prediction of ice shape for the airfoil.

3) This study numerically investigated the influence of a roughness-induced transition on the simulation of inflight icing. An icing physics-based model of roughness distribution was associated with the $\gamma - Re_\theta$ model based on the $k - \omega$ SST turbulent model to consider the interrelation between the roughness of ice and the transition. The distributions of surface roughness were computed through a thermodynamic module and incorporated the turbulent modeling of the transition onset. The numerical results of roughness, convective heat transfer coefficient, and the shape of ice were compared with the experimental results and agreed well with them. Considering the effects of roughness on the transition in the form of the transport equation yielded several advantages over other methods to predict the transition onset. As the transport equation for roughness amplification shows the effects of roughness downstream, the transition onset was computed without an a priori guess, unlike in other turbulence models. Application of the transport equation to the amplification parameter in roughness is an essential component of the

proposed roughness-induced transition model. It can be applied to second-generation icing codes without additional modification by explicitly linking the transport equation with the model. Modeling the transition in inflight icing simulation affects the overall predicted shape of ice. The difference is particularly pronounced on the lower surface of an airfoil with an angle of attack. The noticeable difference effected by the proposed approach was in the formation of ice horns. These numerical results indicated that considering roughness-induced transition could be one option to improve the accuracy of the second-generation inflight icing code.

The numerical simulation of inflight icing using the quasi-unsteady approach improves the accuracy of aircraft icing shape prediction based on unsteady factors such as body motion, roughness distribution, and boundary layer transition, demonstrating the versatility of the quasi-unsteady assumption. The quasi-unsteady assumption focused on numerically resolving discrepancies between the physical time scales in unsteady characteristics and ice accretion efficiently. However, further research is required to address some physical loopholes in numerical models which were empirically modified and extend the present method to more practical cases.

The quasi-unsteady approach for the rotorcraft icing problem needs to be continued for practicality and is therefore applicable in industrial fields. Such issues are significant in the design and certification process for rotorcraft that require many calculations under different aero-icing conditions. With the quasi-unsteady assumption, the complex physics of a rotor blade with high frequency, such as the

pitching and plunging motion of a rotor blade, would be considered. In addition, generating an appropriate grid and updating the icing shape is challenging for a complex rotorcraft configuration that includes rotating and non-rotating components. The validation process also requires extensive work and continues to offer opportunities for new research along with experiments.

Other areas, such as roughness and turbulence model development, would also be challenging issues where numerical methodologies are less mature than their counterparts in fixed-wing aircraft. While the present study proposed novel methods for simulating roughness distribution and its effect, experiments or numerical simulations have yet to verify the impact of unsteady motion. It can be inferred that the unsteady effect would have a critical impact; however, due to the change in small units, defining the exact process is difficult through experiments and simulation. Consequently, the numerical simulations include the development of appropriate physical models for rotorcraft icing challenges and resolving unsteady issues, which are inherently limited in the present numerical methodology. Several exciting opportunities will be in the future for developing more innovative computational models with advanced capabilities and providing the ability to access more diverse issues in the design or compliance process of rotorcraft.

References

[1] Parachivoiu, I., and Saeed, F., "Aircraft Icing," *Wiley*, New York, 2004.

[2] "Proceeding of the FAA International Conference on Aircraft In-flight Icing," Springfield, Virginia, May 6-8, 1996, Vol I & II, U.S. *Department of Transportation, Federal Aviation Administration*, DOT/FAA/AR-96/81, Final Report, August, 1996.

[3] Thomas, S.K., Cassoni, R.P., and MacArthur, C.D., "Aircraft Anti-Icing and Deicing Techniques and Modeling," *Journal of Aircraft*, Vol. 33, No. 5, 1996, pp. 841–854.

[4] FAA, "Title 14 - Aeronautics and Space, Chapter 1 - FAA, Department of Transportation, Subchapter C - Aircraft, Part 25 - Airworthiness Standards: Transport Category Airplanes, Special Federal Aviation Regulation No. 109, Subpart 1, Appendices C and O," GPO - Electronic CFR, 2016.

[5] EASA, "Certification Specifications and Acceptable Means of Compliance for Large Aeroplanes CS-25, Appendices C and O," Amendment 18, 12 Jun 2016.

[6] Langmuir, I. and Blodgett, K.B., "A Mathematical Investigation of Water Droplet Trajectories," *Army Air Forces Technical Report*, No 5418, Feb., 1946.

[7] Messinger, B.L., "Equilibrium Temperature of an Unheated Icing Surface as a Function of Air Speed," *Journal of the Aeronautical Sciences*, Vol. 20, No. 1, 1953, pp. 29–42.

[8] Ruff, G. A., & Berkowitz, B. M., “User’s Manual for the NASA Lewis ice accretion prediction code (LEWICE),” 1990.

[9] Wright, W. B., Gent, R. W., and Guffond, D. “DRA/NASA/ONERA Collaboration on Icing Research. Part 2; Prediction of Airfoil Ice Accretion,” NASA-CR-202349, 1997.

[10] Brahimi, N. T., P. Tran, and I. Paraschivoiu, “Numerical Simulation and Thermodynamic Analysis of Ice Accretion on Aircraft Wings," *Center de Development Technologique de Ecole Polytechnique de Montreal, Final report CDT Project C* 159 (1994): 1994.

[11] Beaugendre, H., Morency, F., and Habashi, W. G., “Development of a Second Generation In-flight Icing Simulation Code,” Journal of Fluid Engineering, Vol. 128, No. 2, 2006, pp. 378-387.
DOI: https://doi.org/10.1115/1.2169807

[12] Son, C., Oh, S., and Yee, K., “Development of 2nd Generation Ice Accretion Analysis Program for Handling General 3-D Geometries,” *Journal of computational fluids engineering*, Vol. 20, No.2, 2015, pp. 23-36.
DOI: https://doi.org/10.6112/kscfe.2015.20.2.023

[13] Habashi, W. G., “Recent Advances in CFD for In-flight Icing Simulations,” *Japan Society of Fluid Mechanics*, Vol. 28, No. 2, 2009, pp. 99-118.

[14] Dow, Sr., J., Aliaga, C., Shah, S., Chen, J., Habashi, W. G., Siemens, J. L., "FENSAP-ICE in Aid of Certification: From CFD to Flight Testing," SAE

Technical Paper 2011-38-0033, 2011

DOI: https://doi.org/10.4271/2011-38-0033

[15] Cebeci, T., Kafyeke, K., “Aircraft Icing,” Annual Review of Fluid Mechanics, Vol. 35, pp. 11-21., 2003.

DOI: https://doi.org/10.1146/annurev.fluid.35.101101.161217

[16] Frink, T. N., Murphy , P. C., Atkins, H. L., Viken, S. A., Petrilli, J. L., Gopalarathnam, A., and Paul, R. C., "Computational Aerodynamic Modeling Tools for Aircraft Loss of Control", Journal of Guidance, Control, and Dynamics, Vol. 40, No. 4, pp. 789-803. 2017

DOI: https://doi.org/10.2514/1.G001736

[17] Aliaga, C. N., Aubé, M. S., Baruzzi, G. S., and Habashi, W. G., “FENSAP-ICE-Unsteady: unified in-flight icing simulation methodology for aircraft, rotorcraft, and jet engines,” *Journal of Aircraft*, Vol. 48, No. 1, 2011, pp. 119-126.

DOI: https://doi.org/10.2514/1.C000327

[18] Morelli, M., Zhou, B. Y., and Guardone, A., “Simulation and analysis of oscillating airfoil ice shapes via a fully unsteady collection efficiency approach,” *75th International Annual Forum American Helicopter Society*, Philadelphia, Pennsylvania, USA, May 2019.

[19] Rajmohan, N., Bain, J., Nucci, M., and Kreeger, R., “Icing Studies for the UH-60A Rotor in Forward Flight,” *2010 AHS Aeromechanics Specialists' Conference*, San Francisco, CA, Jan. 2010, pp. 261–276.

[20] Bain, J., Deresz, R., Sankar, L., Egolf, T. A., Flemming, R., and Kreeger, E., "Effects of Icing on Rotary Wing Loads and Surface Heat Transfer," *49th AIAA Aerospace Sciences Meeting including the New Horizons Forum and Aerospace Exposition*, Orlando, Florida, USA, January 2011.
DOI: https://doi.org/10.2514/6.2011-1100

[21] Reinhart, T., Flemming, R. J., Narducci, R., and Aubert, R. J., "Oscillating Airfoil Icing Tests in the NASA Glenn Research Center Icing Research Tunnel," (No. 2011-38-0016). *SAE Technical Paper*, 2011.
DOI: https://doi.org/10.4271/PT-163

[22] Narducci, R., and Reinhart, T., "Calculations of Ice Shapes on Oscillating Airfoils," *SAE Technical Paper*, No. 2011-38-0015, 2011.
DOI: https://doi.org/10.4271/2011-38-0016

[23] Fouladi, H., Aliaga, C. N., and Habashi, W. G., "Quasi-unsteady icing simulation of an oscillating airfoil," *7th AIAA Atmospheric and Space Environments Conference*, Dallas, Texas, USA, June 2015, p. 3020.
DOI: https://doi.org/10.2514/6.2015-3020

[24] Morelli, M., Zhou, B. Y., & Guardone, A., "Acoustic Characterization of Glaze and Rime Ice Structures on an Oscillating Airfoil via Fully Unsteady Simulations," *Journal of the American Helicopter Society*, Vol. 65, No. 4, 2020, pp. 1-12.
DOI: https://doi.org/10.4050/JAHS.65.042004

[25] Olsen, W., and Walker, E., “Experimental Evidence for Modifying the Current Physical Model for Ice Accretion on Aircraft Surfaces,” NASA TM-87184, 1986.

[26] Hansman, R. J., and Turnock, S., “Investigation of Surface Water Behavior during Glaze Ice Accretion,” *AIAA Journal*, Vol. 26, No. 2, 1989, pp. 140-147. DOI: https://doi.org/10.2514/3.45735

[27] Shin, J., “Characteristics of Surface Roughness Associated with Leading Edge Ice Accretion,” NASA TM-106459, 1994.

[28] Gent, R., Markiewicz, R., and Cansdale, J., “Further studies of helicopter rotor ice accretion and protection,” Vertica, Vol. 11, pp. 473-492, 1987.

[29] Fortin, G., Ilinca, A., Laforte, J.-L., and Brandi, V., “New Roughness Computation Method and Geometric Accretion Model for Airfoil Icing,” *Journal of Aircraft*, Vol. 41, No. 1, 2004, pp. 119-127. DOI: https://doi.org/10.2514/1.173

[30] Kreith, F., and Black, W. Z., *Basic Heat Transfer*, Harper & Row, New York, 1980, pp. 218-219 and 486-489.

[31] Ozcer, I. A., Baruzzi, G. S., Reid, T., Habashi, W. G., Fossati, M., and Croce, G., “Fensap-ice: Numerical Prediction of Ice Roughness Evolution, and its Effects on Ice Shapes,” SAE Technical Paper, No. 2011-38-0024, 2011. DOI: https://doi.org/10.4271/2011-38-0024

[32] Beaugendre, H., Morency, F., and Habashi, W. G., “FENSAP-ICE's Three-Dimensional In-flight Ice Accretion Module: ICE3D,” *Journal of Aircraft*, Vol.

40, No. 2, 2003, pp. 239-247.

DOI: https://doi.org/10.2514/2.3113

[33] Cebeci, T. and Bradshaw, P., *Physical and Computational Aspects of Convective Heat Transfer*, Springer-Verlag, New York, 1984.

[34] Wright, W., "Advancements in the LEWICE Ice Accretion Model," NASA CR-191019, 1993.

[35] Hasanzadeh, K., Laurendeau, E., and Paraschivoiu, I., "Quasi-steady Convergence of Multistep Navier–Stokes Icing Simulations," *Journal of Aircraft*, Vol. 50, No. 4, 2013, pp. 1261-1274.

DOI: https://doi.org/10.2514/1.C032197

[36] Habashi, W. G., "Recent Advances in CFD for In-flight Icing Simulations," *Japan Society of Fluid Mechanics*, Vol. 28, No. 2, 2009, pp. 99-118.

[37] Spalart, P. R., and Aupoix, B., "Extensions of the Spalart–Allmaras Turbulence Model to Account for Wall Roughness," *International Journal of Heat and Fluid Flow*, Vol. 24, No. 4, 2001, pp. 454-462.

DOI: https://doi.org/10.1016/S0142-727X(03)00043-2

[38] Aupoix, B., "Wall Roughness Modelling with k–w SST Model," *10th International ERCOFTAC Symposium on Engineering Turbulence Modelling and Measurements*, ERCOFTAC, Brussels, Belgium, 2014.

DOI: https://doi.org/10.1016/j.ijheatfluidflow.2008.09.009

[39] Henry, R. C., Hansman, R. J., and Breuer, K. S., "Heat Transfer Variation on Protuberances and Surface Roughness Elements," *Journal of Thermophysics*

and Heat Transfer, Vol. 9, No. 1, 1995, pp. 175-180.

DOI: https://doi.org/10.2514/3.644

[40] Han, Y., and Palacios, J., "Transient Heat Transfer Measurements of Surface Roughness Due to Ice Accretion," *6th AIAA Atmospheric and Space Environments Conference*, AIAA, Reston, VA, USA, 2014, p. 2464.

DOI: https://doi.org/10.2514/6.2014-2464

[41] McClain, S., Vargas, M., Tsao, J., Broeren, A., and Lee, S., "Ice Accretion Roughness Measurements and Modeling," *7th European Conference for Aeronautics and Space Sciences*, EUCASS, Milan, Italy, 2017.

DOI: https://doi.org/10.13009/EUCASS2017-555

[42] Dassler, P., Kozulovic, D., and Fiala, A., "An Approach to Modelling the Roughness-induced Boundary Layer Transition Using Transport Equations," *European Congress on Computational Methods in Applied Sciences and Engineering*, ECCOMAS, Barcelona, Spain, 2012, Paper no. 1821.

[43] Feindt, E., "Untersuchungen uber die Abhangigkeit des Umschlages Laminar-turbulent von der Oberflachenrauhigkeit und der Druckverteilung," DFL Bericht, vol. 43, 1956, pp. 180-203.

[44] Langel, C. M., Chow, R., Van Dam, C. C. P., Rumsey, M. A., Maniaci, D. C., Ehrmann, R. S., and White, E. B., "A Computational Approach to Simulating the Effects of Realistic Surface Roughness on Boundary Layer Transition," *52nd Aerospace Sciences Meeting*, 2014, p. 0234.

DOI: https://doi.org/10.2514/6.2014-0234

[45] Pedgley, D. E., “Luke Howard and his clouds. *Weather*,” Vol. 58, No. 2, 2003, pp. 51-55.

[46] What’s that cloud?, (2019, Aug 29), https://media.bom.gov.au/social/blog/895/whats-that-cloud/

[47] J.G. Mason, P. Chow, and D.M. Fuleki, “Understanding Ice Crystal Accretion and Shedding Phenomenon in Jet Engines Using a Rig Test”, *Journal of Engineering for Gas Turbines and Power*, Vol. 133, No. 4, 2011.

[48] Jeck, R. K., “Icing Design Envelopes (14 CFR Parts 25 and 29, Appendix C) Converted to a Distance-Based Format,” Federal Aviation Administration Rept. DOT/FAA/AR-00/30, 2002.

[49] Han, Y., Palacios, J., and Smith, E., “An Experimental Correlation between Rotor Test and Wind Tunnel Ice Shape on NACA 0012 Airfoils,” *SAE Technical Paper*, 2011-38-0092, 2011
DOI: htttps://doi.org/10.4271/2011-38-0092

[50] Hedde, T., and Guffond, D., "ONERA Three-Dimensional Icing Model," AIAA Journal, Vol. 33, No. 6, 1995, pp. 1038-1045.

[51] Hess, J. L., and A.M.O., “Smith, Calculation of non-lifting potential flow about arbitrary three-dimensional bodies,” Douglas Aircraft Company Report No. ES 40622, 1962.

[52] Frost, W., Chang, H., Shieh, C., & Kimble, K. (1982). Two-dimensional particle trajectory computer program. Interim Report for Contract NAS3-22448.

[53] Bourgault, Y., Boutanios, Z., & Habashi, W. G., "Three-dimensional Eulerian approach to droplet impingement simulation using FENSAP-ICE, Part 1: model, algorithm, and validation," *AIAA Journal*, Vol. 37, No. 1, 200, pp. 95-103. DOI: https://doi.org/10.2514/2.2566

[54] Myers, T. G., "Extenstion to the Messinger model for aircraft icing," AIAA Journal, Vol. 39, No. 2, 2001, pp. 211-128. DOI: https://doi.org/10.2514/2.1312

[55] T.G. Myers, Extension to the Messinger model for aircraft icing, AIAA J. 39, 211-218 (2001)

[56] OpenFOAM, "Open-source Field Operation and Manipulation," Software Package, Ver. 2012, 2020, http://www.openfoam.com.

[57] Cabler, S. J., "Aircraft Ice Protection," Federal Aviation Administration AC 20-73A, Aug. 2006.

[58] Knopp, T., Eisfeld, B., amd Calvo, J. B., "A new extension for k–ω turbulence models to account for wall roughness," *International Journal of Heat and Fluid Flow*, Vol. *30*, No. 1, 2009, pp. 54-65. DOI: https://doi.org/10.1016/j.ijheatfluidflow.2008.09.009

[59] Flemming, R. J., Britton, R. K., & Bond, T. H. Role of wind tunnels and computer codes in the certification and qualification of rotorcraft for flight in forecast icing, 1994. NASA TM, 106747.

[60] Korkan, K. D., Cross Jr, E. J., & Miller, T. L. "Performance degradation of a model helicopter rotor with a generic ice shape," *Journal of Aircraft*, Vol.21,

No. 10, 1984, pp. 823-830.

DOI: https://doi.org/10.2514/3.45049

[61] Bragg, M., and Gregorek, G., “Aerodynamic characteristics of airfoils with ice accretions,” *20th Aerospace Sciences Meeting, AIAA*, Columbus, OH, USA 1982, p. 282.

DOI: https://doi.org/10.2514/6.1982-282

[62] Korkan, K. D., Dadone, L., and Shaw, R. J., “Performance degradation of helicopter rotor in forward flight due to ice,” *Journal of Aircraft*, Vol. 22, No. 8, 1985, pp. 713-718.

[63] Britton, R., and Bond, T., “A review of ice accretion data from a model rotor icing test and comparison with theory,” *In AIAA 29th Aerospace Sciences Meeting*, Reno, NV, USA, 1991, p. 661.

DOI: https://doi.org/10.2514/6.1991-661

[64] Britton, R., “Development of an analytical method to predict helicopter main rotor performance in icing conditions,” *In AIAA 30th Aerospace Sciences Meeting and Exhibit*, Reno, NV, USA, 1992, p. 418.

DOI: https://doi.org/10.2514/6.1992-418

[65] Cebeci, T., Chen, H., and Alemdaroglu, N., "Fortified LEWICE with viscous effects," *In AIAA 28th Aerospace Sciences Meeting*, Reno, NV, USA, 1990, p. 754.

DOI: https://doi.org/10.2514/6.1990-754

[66] Rajmohan, N., Bain, J., Nucci, M., Sankar, L., Flemming, R., Egolf, T. A., and Kreeger, R., "Icing Studies for the UH-60A Rotor in Forward Flight," In *AHS Specialist's Conference on Aeromechanics*, USA, 2010.

[67] Bain, J., Deresz, R., Sankar, L., Egolf, T. A., Flemming, R., and Kreeger, E., "Effects of Icing on Rotary Wing Loads and Surface Heat Transfer," In *49th AIAA Aerospace Sciences Meeting including the New Horizons Forum and Aerospace Exposition*, Orlando, FL, USA, 2011, p. 1100.
DOI: https://doi.org/10.2514/6.2011-1100

[68] Rajmohan, N., "Application of hybrid methodology to rotors in steady and maneuvering flight," Georgia Institute of Technology, 2010.

[69] Bauchau, O. A., and Kang, N. K., "A Multi-body Formulation for Helicopter Structural Dynamic Analysis," *Journal of the American Helicopter Society*, Vol. 38, No 2, April 1993, pp. 3-14.
DOI: https://doi.org/10.4050/JAHS.38.3

[70] Bidwell, C. S., and Potapczuk, M. G. "Users manual for the NASA Lewis three-dimensional ice accretion code (LEWICE 3D)," NAS 1.15: 105974, 1993.

[71] Narducci, R., and Kreeger, R. E. "Analysis of a hovering rotor in icing conditions," *In AHS 66th Annual Forum and Technology Display,* E-17815, 2012.

[72] Narducci, R., Orr, S., and Kreeger, R. E., "Application of a high-fidelity icing analysis method to a model-scale rotor in forward flight," *In AHS 67th Annual Forum and Technology Display*, NASA/TM-2012-217122, 2012.

[73] Jasak, H., “Dynamic mesh handling in OpenFOAM,” In *47th AIAA aerospace sciences meeting including the new horizons forum and aerospace exposition*, Orlando, Florida, USA, January 2009, p. 341.
DOI: https://doi.org/10.2514/6.2009-341

[74] Demirdzic, I., and Peric, M., “Space conservation law in finite volume calculations of fluid flow,” *International Journal for Numerical Methods in Fluids*, Vol. 8, 1988, pp. 1037–1050.
DOI: https://doi.org/10.1002/fld.1650080906

[75] McClain, S. T., & Kreeger, R. E. (2013). Assessment of Ice Shape Roughness Using a Self-Organizing Map Approach. In *5th AIAA Atmospheric and Space Environments Conference* (p. 2546).

[76] S.T. McClain, M.M. Vargas, J.C. Tsao, Characterization of ice roughness variations in scaled glaze icing conditions, 8th AIAA Atmos. Space Environ. Conf., 13–17 June, 2016.

[77] S.T. McClain, M.M. Vargas, J.C. Tsao, Ice roughness and thickness evolution on a swept NACA 0012 airfoil, 9th AIAA Atmos. Space Environ. Conf, 5–9 June, 2017.

[78] Neubauer, T., Hassler, W., & Puffing, R. (2020). Ice Shape Roughness Assessment Based on a Three-Dimensional Self-Organizing Map Approach. In *AIAA AVIATION 2020 FORUM* (p. 2805).
DOI: https://doi.org/10.2514/6.2020-2805

[79] Henry, R. C., Hansman, R. J., and Breuer, K. S., "Heat Transfer Variation on Protuberances and Surface Roughness Elements," *Journal of Thermophysics and Heat Transfer*, Vol. 9, No. 1, 1995, pp. 175-180.
DOI: https://doi.org/10.2514/3.644

[80] Yamaguchi, K., and Hansman, R. J., "Heat Transfer on Accreting Ice Surfaces," *Journal of Aircraft*, Vol. 29, No. 1, 1992, pp. 108-113.
DOI: https://doi.org/10.2514/3.46132

[81] D. N. Anderson, and J. Shin, "Characterization of Ice Roughness from Simulated Icing Encounters," NASA TM 107400, 1997

[82] Mingione, G., and Brandi, V., "Ice Accretion Prediction on Multielements Airfoils," *Journal of Aircraft*, Vol. 35, No. 2, 1998, pp. 240-246.
DOI:

[83] Croce, G., Candido, E. D., Habashi, W. G., Munzar, J., Aubé, M. S., Baruzzi, G. S., and Aliaga, C. N., "FENSAP-ICE: Analytical model for spatial and temporal evolution of in-flight icing roughness," *Journal of Aircraft*, Vol. 47, No. 4, 2010, pp. 1283-1289.
DOI:

[84] El Sherbini, A. I., and Jacobi, A. M., "Retention Forces and Contact Angles for Critical Liquid Drops on Non-horizontal Surfaces," *Journal of Colloid and Interface Science*, Vol. 299, 2006, pp. 841-849.
DOI: https://doi.org/10.1016/j.jcis.2006.02.018

[85] Min, S., and Yee, K., "New roughness-induced transition model for simulating ice accretion on airfoils," *AIAA Journal,* Vol. 59, No. 1, 2021, pp. 250-262. DOI: https://doi.org/10.2514/1.J059222

[86] Gerhart, P. M., and Gross, R. J., *Fundamentals of fluid mechanics,* Addison-Wesley, Wokingham, 1985.

[87] Poinsatte, P. E., Fossen, G. V., Newton, J. E., and DeWitt, K. J., "Heat Transfer Measurements from a Smooth NACA 0012 Airfoil," *Journal of Aircraft,* Vol. 28, No. 12, 1991, pp. 892–898. DOI: https://doi.org/10.2514/3.46114

[88] Poinsatte, P. E., Fossen, G. V., and DeWitt, K. J., "Roughness Effects on Heat Transfer from a NACA 0012 Airfoil," *Journal of Aircraft,* Vol. 28, No. 12, 1991, pp. 908-911. DOI: https://doi.org/10.2514/3.46116

[89] Kerho, M. F., and Bragg, M. B., "Airfoil Boundary-layer Development and Transition with Large Leading-edge Roughness," *AIAA Journal,* Vol. 35, No. 1, 1997, pp. 75-84. doi: https://doi.org/10.2514/2.65

[90] Cebeci T., and Besnard E., "Progress Towards the Prediction of the Aerodynamic Performance Degradation of an Aircraft in Natural Icing Conditions," *The First Bombardier International Workshop Aircraft Icing/Boundary Layer Stability and Transition,* 1993, pp. 57-85.

[91] Menter, F. R., Langtry, R., and Volker, S., "Transition Modelling for General Purpose CFD Codes." *Flow, Turbulence and Combustion*, Vol. 77, No. 1-4, 2006, pp. 277-303.
DOI: https://doi.org/10.1016/B978-008044544-1/50003-0

[92] Colebrook, C. F., and White, C. M., "Experiments with Fluid Friction in Roughened Pipes," *Proceedings of the Royal Society of London A*, Vol. 161, 1937, pp. 367-381.
DOI: https://doi.org/10.1098/rspa.1937.0150

[93] Piziali, R. A., "2-D and 3-D oscillating wing aerodynamics for a range of angles of attack including stall," NASA-TM-4632, 1994.

[94] Dumlupinar, E., and Murthy, V., "Investigation of dynamic stall of airfoils and wings by CFD," *29th AIAA applied aerodynamics conference*, Honolulu, Hawaii, USA, June 2011.
doi: https://doi.org/10.2514/6.2011-3511

[95] Sheng, W., Galbraith, R. A. M., Coton, F. N., and Gilmour, R., "The collected data for tests on an S809 aerofoil," technical report, Department of Aerospace Engineering, University of Glasgow, 2006.

[96] Nandi, T. N., Brasseur, J. G., and Vijayakumar, G., "Prediction and Analysis of the Nonsteady Transition and Separation Processes on an Oscillating Wind Turbine Airfoil using the γ-Re_θ Transition Model," *34th AIAA wind energy symposium*, San Diego, California, USA, January 2016.

[97] Son, C., Oh, S., and Yee, K., "Ice Accretion on Helicopter Fuselage Considering Rotor-wake Effects," *Journal of Aircraft*, Vol. *54*, No. 2, 2017, pp. 500-518. doi: https://doi.org/10.2514/1.C033830

[98] Wright, W. B., and Rutkowski, A., "Validation Results for LEWICE 2.0," NASA/CR-1999-208690, 1999.

국문 초록

항공기 결빙 형상을 정확히 예측하는 것은 비행 운영 안정성을 확보하는데 중요하다. 항공기 결빙 현상에는 다양한 단위를 갖는 변수들이 관여하므로, 초기 수치해석 도구를 개발할 때에는 수치적 효율성을 고려하고자 하였다. 이러한 변수들간의 단위 차이를 해결하기 위해서 일반적인 항공기 결빙 해석 코드들은 준정상 가정을 도입하였다. 해당 방법은 각 변수들에 대해 정상상태 해와 멀티샷 방법을 사용하였다. 해당 방법은 수치적인 효율성을 달성하였으나, 결빙 해석의 정확성에 영향을 줄 수 있는 비정상 특성을 일부 고려하지 못하였다. 이러한 비정상 특성은 항공기와 같이 움직이는 물체의 공기역학적 비정상성을 모델링하는 것과 표면에서의 미세한 표면 거칠기 변화를 포함한다. 이전의 연구에서는 결빙 해석 코드의 정확도와 적용 범위를 올리기 위하여 해당 문제들을 해결하기 위해 노력하였다.

본 연구는 준비정상 가정을 통해 항공기 결빙에서 나타날 수 있는 비정상과 관련된 문제들을 완화하고자 하였다. 준비정상 해석은 유동과 공기 중의 액적 및 표면에서의 수막 방정식을 동시에 해석하므로 결빙 과정 중 나타날 수 있는 비정상 특성을 고려할 수 있다. 준비정상 해석 방법을 기반으로 진동하는 익형에 대하여 항공기 결빙 해석을 진행하였다. 진동하는 익형의 움직임을 고려하기 위해서 동적 격자 방법을 사용하였다. 해당 연구는 또한 결빙 형상 예측의 정확도를 위해, 거칠기 분포 모델과 난류 천이를 고려할 수 있는 새로운 모델을 제시하였다. 해당 모델은 거칠기 증폭 변수와 난류 천이 모델을 통해

거칠기와 경계층 사이의 상호 작용을 보였다.

준 비정상 해석은 기존의 수치 해석 연구와 비교했을때 결빙 형상을 더 정확하게 예측하였다. 본 연구에서는 준 비정상 해석방법이 물체의 움직임에 따른 비정상 특성이 액적의 수집 효율과 표면의 대류 열전달에 미치는 영향을 보였으며, 기존의 준 정상 해석방법과 같이 진동하는 익형에 대해서 거칠기 모델과 난류 천이 모델이 결빙 형상 예측의 정확도를 향상시킬수 있음을 보였다. 거칠기 분포와 거칠기 분포에 따른 대류 열전달 계수를 기존 해석 도구에서 사용된 난류모델과 비교를 통해 적용된 모델들을 검증하였다. 본 연구에서 제시된 개선된 모델들은 기존의 실험 결과들과 일치하는 것을 확인하였으며, 결빙 과정의 비정상 특성을 고려하는 것이 해석 정확도를 높일 수 있음을 보였다.

주요어: 항공기 안전, 항공기 결빙, 진동 익형, 표면 거칠기, 준 비정상 해석, 난류 천이, 난류 모델, 대류 열전달 계수

학번: 2018-34705

성명: 민승인